Modelling failure of laminated composites using physically-based failure models

by

Silvestre Taveira Pinho

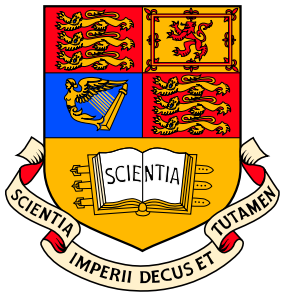

Department of Aeronautics
South Kensington Campus
Imperial College London
London SW7 2AZ
U.K.

This thesis is submitted for the degree of Doctor of Philosophy of the University of London

2005

Abstract

Numerically modelling the crushing of composite structures is important in crashworthiness. In this work, advanced material models are formulated and implemented into an explicit finite element code to model delamination and ply failure.

A new interface element with mixed mode capabilities is formulated and implemented to model delamination. A 3D ply material model is formulated and is also implemented into the same code. The material model distinguishes matrix and fibre tensile and compressive failure, and includes nonlinear behaviour in shear. Matrix compressive failure is addressed with a phenomenological approach based on the Mohr-Coulomb failure criterion. For the fibre failure in compression, a 3D criterion that considers an initial fibre misalignment angle prompting compressive failure is used. Failure in tensile of the matrix is modelled with a simpler stress interaction criterion, and no stress interaction is considered for fibre tensile failure. On the post failure onset behaviour, the failure process is smeared over the finite element dimension. This allows for constant energy absorption, regardless of mesh refinement.

Experimental tests were carried to measure the energy release rate associated with intralaminar fracture, fibre tensile failure and fibre kinking, as these are material properties required by the numerical model.

Finally, the validation and applications of the interface element and ply failure model are presented. Analytical and experimental data are shown to be in good agreement with the numerical predictions.

Contents

List of Figures

List of Tables

Acknowledgments

The author would like to acknowledge the support from the Portuguese Foundation for Science and Technology (Fundação para a Ciência e a Tecnologia, FCT) and the University of Porto for their funding which made this research possible.

For their constant supervision, guidance and advice throughout the last three years, the author would like to thank both his supervisors, Dr. Lorenzo Iannucci and Dr. Paul Robinson.

The interest, involvement and participation of Dr. Pedro Camanho and Dr. Carlos Dávila in the work presented in Chapter 3 is acknowledged. A more detailed description of their contribution is included at the beginning of the same chapter.

Equally to Dr. Pedro Camanho, Prof. Paulo Tavares de Castro and Prof. António Torres Marques, the author is indebted for their support and for contributing to create the conditions that made this PhD project at Imperial College London possible.

The author would also like to thank Dr. Emile Greenhalgh and Ms. Victoria Bloodworth for help with obtaining fractographic images and their interpretation; Dr. Letty Foulkes for help with Linux; Dr. John Hodgkinson for providing some of the prepreg material used; Mr. Gary Senior and Mr. Russell Stracey for help with the manufacture of laminates and machining of specimens; and Mr. Joseph Meggyesi and Mr. William Godwin for help with experimental testing.

Finally, the author would like to acknowledge his family, Antigoni, Octávio and all his friends and colleagues who humored him during this research.

Notation

Lower case Roman letters

a ..... fibre direction

a ..... crack length

a ..... dimension of an elliptic region along x

a .... length of the initial pre-crack (four point bend, compact tension and compact compression tests)

a_o ..... initial crack length

a_o ..... half length of a slit crack

a_o . initial length of the pre-crack (compact tension and compact compression tests)

a_L ..... dimension of the crack in the longitudinal direction

a^m ..... fibre direction in the fibre misalignment frame

b ..... in-plane transverse direction

b ..... dimension of an elliptic region along y

b ..... length of the tabs in a specimen (compression, tension and shear tests)

b ..... specimen width (DCB test)

b_{cal} ..... width of a calibration specimen (MMB test)

b^m ..... transverse direction in the fibre misalignment frame

$\mathbf{b}^t$ ..... fictitious body force

b^ψ axis defining the orientation of the fibre-kinking plane, as shown in Fig. 3.15(b)

c ..... through-the-thickness direction

c ..... dimension of an elliptic region along z

c .... distance between a loading point and a support point in an intralaminar test (Fig. 5.2)

c_i . . . . coefficients, $i = 0, 1, 2, 3h$ thickness of a four point bend specimen (four point bend, compact tension and compact compression tests)

c^{ψ} axis defining the orientation of the fibre-kinking plane, as shown in Fig. 3.15(b)

d . . . . . damage variable

d . . . . . distance between the two load points in a 4ENF specimen

$d\,(t)$ . . . . . damage variable at time t

$d(\tau)$ . . . . . damage variable at time τ

d^{inst} . . . . . instantaneous value of a damage variable

$d^{inst}\,(t')$ . . . . . instantaneous value of a damage variable at time t'

$d^{inst}(\tau')$ . . . . . damage variable at time τ'

d_i . . . . . damage variable for the i failure mode, $i = mat, kink, ft$

f . . . . . failure index (failure when $f = 1$)

f_f . . . . . failure index for the fibre failure mode (failure when $f_f = 1$)

f_{ft} . . . . . failure index for the fibre tensile failure mode (failure when $f_{ft} = 1$)

f_{kink} . . . . . failure index for the fibre-kinking failure mode (failure when $f_{kink} = 1$)

f_{mat} . . . . . failure index for the matrix failure mode (failure when $f_{mat} = 1$)

f_{mc} . . . failure index for the matrix compression failure mode (failure when $f_{mc} = 1$)

f_{mt} . . . . . failure index for the matrix tensile failure mode (failure when $f_{mt} = 1$)

f_{CL} . . . . . constitutive law for the shear behaviour $\tau = f_{CL}\,(\gamma)$

g . . . . . mode ratio for intralaminar fracture, $g = G_{Ic}/G_{IIc}$

h . . . . . half thickness (MMB test)

h . . . . . thickness of the tabs in a specimen (compression, tension and shear tests)

h . . . . . total specimen thickness (DCB test)

k . . . . . penalty stiffness

k_{pos} . . . . . penalty stiffness for a positive opening mode component of the relative displacement (i.e. $\delta_1 > 0$)

k_{neg} . . . . . penalty stiffness for a negative opening mode component of the relative displacement (i.e. $\delta_1 \leq 0$)

k_1 . . . . . parameter for the logarithmic law $\tau = k_1 \ln(k_2\gamma + 1)$

k_2 . . . . . parameter for the logarithmic law $\tau = k_1 \ln(k_2\gamma + 1)$

l . . . . . mesh size

m ..... parameter in Williams and Vaziri's model [146]
m ..... slope of the load-displacement curve (MMB test)
m ..... parameter for the least squares fit of the experimental data in a 4ENF test
m_{cal} ..... slope of the load-displacement curve (MMB test)
n ..... number of layers
$\mathbf{n}$ ..... normal to an ellipsoid
t ..... thickness of a ply
t ..... thickness
t ..... thickness of a specimen (compression, tension and shear tests)
t_{cal} ..... thickness of a calibration specimen (MMB test)
t_i ..... component i of the traction vector, $i = 1, 2, 3$
t^o ..... magnitude of the traction vector at the onset of damage
t_{shear} ..... shear component of the traction vector
w ..... width
w ..... width of a damage band
x ..... geometric coordinate
y ..... geometric coordinate
z ..... geometric coordinate

Upper case Roman letters

A ..... area of a crack
A ..... cross-sectional area
A_o ..... initial cross-sectional area
C ..... compliance
$\mathbf{C}$ ..... constitutive law tensor
$\mathbf{C}^*$ ..... constitutive tensor of an elliptical inclusion
C_0 ..... parameter for the least squares fit of the experimental data in a 4ENF test
C_{sys} ..... compliance of the loading system (MMB test)
E ..... Young's modulus
E_{cal} ..... modulus of a calibration specimen (MMB test)
E_i ..... Young's modulus in the i direction, $i = a, b, c$

E_{int} ..... interaction energy

E_f ..... bending modulus

F ..... total energy transferred to a body through external work

F_i ..... parameter for interactive criteria, $i = 1, 2, 6$

F_{ii} ..... parameter for interactive criteria, $i = 1, 2, 6$

F_{12} ..... parameter for interactive criteria

F_{12}^* ..... parameter for interactive criteria

G ..... energy release rate

G_c ..... critical energy release rate

G_i ..... mode i component of the energy release rate, $i = I, II, III$

G_{ic} ..... mode i component of the critical energy release rate, $i = I, II, III$

G_{ij} ..... Shear modulus in the (i, j) plane, $ij = ab, bc, ca$

G^i ..... energy release rate for crack growth in direction i, with $i = T, L$

G_I^i mode I component of the energy release rate for crack propagation in direction i, with $i = T, L$

G_{Ic}^i . mode I component of the critical energy release rate for crack propagation in direction i, with $i = T, L$

G_{II}^i ..... mode II component of the energy release rate for crack propagation in direction i, with $i = T, L$

G_{IIc}^i mode II component of the critical energy release rate for crack propagation in direction i, with $i = T, L$

G_{matrix} ..... shear modulus of the matrix

G_{shear} ..... shear component of the energy release rate

G_{Sc} ..... shear mode critical energy release rate

G_{Sc} ..... shear component of the critical energy release rate

G_{tot} ..... total energy release rate

I ..... moment of inertia of one arm of a DCB specimen

K_{Ic} ..... mode I critical stress intensity factor

K_{II} ..... mode II stress intensity factor

L ..... characteristic length

L ..... longitudinal direction

L ..... half distance between the support points in an intralaminar test (Fig. 5.2)

L ..... length of a specimen (compression, tension and shear tests)

L ..... half length of a 4ENF or MMB specimen

L_i ..... length of a brick element along axis i with $i = 1, 2, 3$

L_i ..... characteristic length for the i failure mode, $i = mat, kink, ft$

L_i ..... characteristic length given in Figs. D.1(a), (b) and (c), $i = a, c^{\phi}, a^{m}$

N ..... maximum allowable traction for loading in pure mode I

P ..... total applied load at failure (four point bend, compact tension and compact compression tests)

P ..... applied load

$\mathbf{P}$ tensor used to obtain the stress field in a transformed region; it can by found in Refs. [188, 189]

P_c ..... load at onset of crack propagation

$\mathbf{Q}$ ..... tensor used to obtain the stress field in a transformed region

S ..... maximum allowable traction for loading in pure shear mode

S ..... compliance

S ..... surface

S_{ij} ..... shear strength in plane (i, j), with $ij = ab, bc, ca$

S_{is}^{L} ..... longitudinal shear strength considering in-situ effects

S_L ..... shear strength for the longitudinal direction

S_T fracture plane fracture resistance against its fracture by transverse shear, often referred to in the text as transverse shear strength

T ..... transverse direction

U ..... strain energy of a body

U ..... energy absorbed by an element after complete failure

U_o ..... strain energy of an uncracked body

V ..... volume of an element

V ..... volume

V_f ..... fibre volume fraction

W ..... width of a specimen (compression, tension and shear tests)

W_o ..... uniform strain energy density of the uncracked body

W_o ..... initial width of a specimen (shear test)
W_s ..... energy absorbed by a solid to create the surface of area A
X ..... strength in the longitudinal direction
X_c ..... compressive strength in the longitudinal direction
X_t ..... tensile strength in the longitudinal direction
Y ..... strength in the in-plane transverse direction
Y_c ..... compressive strength in the in-plane transverse direction
Y_t ..... tensile strength in the in-plane transverse direction
Y_{is}^t ..... in-situ transverse tensile strength

Lower case Greek letters

α ..... coefficient of the power law (propagation criterion)
β ..... mode ratio
β.... parameter in the polynomial relation between the shear strain and the shear stress proposed by Hahn and Tsai [110]
β ..... lamination angle
β ..... angle
γ ..... shear strain
γ_{ij} ..... shear strain in the (i, j) plane, $ij = ab, bc, ca$
γ_{ab}^u ..... in-plane shear strain at failure
$\gamma_{ab_{|is}}^u$ ..... in-situ in-plane shear ultimate strain
$\gamma_{ab}^{\max}$ ..... maximum (over time) shear strain
$\gamma_{ab}^{\max}(t)$ ..... maximum (over time) shear strain until time t
$\gamma_{ab}(t')$ ..... maximum (over time) shear strain until time t'
γ_{ab}^{in}.... inelastic component of the in-plane shear strainγ_{ab}^{el} elastic component of the in-plane shear strain
$\gamma_{a^m b^m}^{el}$ ..... elastic component of the shear strain in the (a^m, b^m) plane
γ^o ..... shear strain at failure
γ_m ..... shear strain in the fibre misalignment frame at failure
γ_{mc} ..... shear strain in the fibre misalignment frame at failure for a pure axial compression case

γ_{mat} ..... elastic component of the shear strain acting on the fracture plane, in the direction of τ_{mat}

γ_L^{el} .....elastic component of the longitudinal shear strain component acting on a fracture plane

$\gamma_L^{el,o}$ ..... elastic component of the longitudinal shear strain component acting on a fracture plane at onset of failure

γ_T ..... transverse shear strain component acting on a fracture plane

γ_T^o . transverse shear strain component acting on a fracture plane at onset of failure

δ ..... relative displacement

δ .....opening displacement (DCB test)

$\delta(\tau')$ .....relative displacement at time τ'

δ_i .....component i of the relative displacement vector, $i = 1, 2, 3$

$\delta^{\max}(\tau)$ .....maximum historical value of the relative displacement, until time τ

δ^o .....relative-displacement corresponding to damage onset

δ^f .....relative-displacement corresponding to damage propagation

$\delta^{\max}$ ..... maximum historical value of the relative displacement

δ_{shear} .....shear component of the relative displacement

δ_{shear}^f ..... shear component of the relative-displacement corresponding to damage propagation

δ_{shear}^o shear component of the relative-displacement corresponding to damage onset

δ_N^o relative-displacement corresponding to damage onset for loading in pure mode I

δ_N^f relative-displacement corresponding to damage propagation for loading in pure mode I

δ_S^o . relative-displacement corresponding to damage onset for loading in pure shear mode

δ_S^f .relative-displacement corresponding to damage propagation for loading in pure shear mode

ϵ .....small number (b/a)

ε ..... strain

ε ..... total strain tensor

ε^∞ .....uniform strain at infinity

$\tilde{\varepsilon}$ ..... perturbation in the strain field due to the presence of an inclusion

ε_i ..... normal strain component, $i = a, b, c$

ε_i ..... driving strain for the i failure mode, $i = mat, kink$

ε_{ij} ..... shear strain component, $ij = ab, bc, ca$

ε_i^o ..... normal strain at onset of failure, $i = a, b, c$

ε_{ij}^o ..... shear strain at onset of failure, $ij = ab, bc, ca$

ε_i^{ot} ..... normal strain at onset of failure in tension, $i = a, b, c$

ε_i^{oc} ..... normal strain at onset of failure in compression, $i = a, b, c$

ε_i^o ..... value of the driving strain for the i failure mode at damage onset, $i = mat, kink, a$

ε_i^f ..... value of the driving strain for the i failure mode at damage propagation, $i = mat, kink, a$

ε^{el} ..... elastic strain tensor

ε^f ..... strain at failure propagation

ε^o ..... strain at failure onset

ε_l ..... longitudinal strain

ε_n ..... normal strain component acting on a fracture plane

ε_n^o ..... normal strain component acting on a fracture plane at onset of failure

ε^t ..... transformation strain tensor

ε_{tr} ..... transverse train

η_i stress intensity reduction coefficients for propagation in the transverse direction, $i = I, II, III$

θ . angle defined by the shear and normal components of the relative displacement vector, $\theta = \text{acos}\ \langle \delta_1 \rangle / \delta$

θ ..... angle formed by the shear component of the traction vector, τ**,** and the transverse direction in the fracture plane, i.e., $\theta = \arctan(\tau_L / \tau_T)$

θ ..... misalignment frame

θ ..... lamination angle

θ_c ..... misalignment angle θ at failure for a pure compression case

θ_i ..... initial fibre misalignment angle

κ ..... variable used in the constitutive law from Refs. [11, 12, 21]

λ angle of the resultant shear component of the traction, τ_{mat}, with the component τ_T (see Fig. 4.4(a), $\lambda = \arctan \tau_L/\tau_T$)

μ_T ..... friction coefficient for the transverse direction

μ_L ..... friction coefficient for the longitudinal direction

ν .....Poisson's ratio

ν_{ij} ..... Poisson's ratio in the (i, j) plane, $ij = ab, bc, ca$

ξ_i .....stress intensity reduction coefficients for propagation in the longitudinal direction, $i = I, II, III$

ρ ..... density

σ ..... stress

σ .....stress tensor

$\tilde{\sigma}$ ..... perturbation in the stress field due to the presence of an inclusion

σ^{∞} .....uniform stress at infinity

σ^{ap} ..... applied stress

σ^{ef} .....effective stress

σ_i ..... normal stress component, $i = a, b, c, a^m, b^m, b^{\psi}, c^{\psi}$

$\sigma_i$traction associated with the driving strain for the i failure mode, $i = mat, kink, a$

σ_n .. normal component of the traction vector in a potential matrix fracture plane

σ^o .....stress at onset of failure

σ_i^o.....traction associated with the driving strain for the i failure mode at damage onset, $i = mat, kink, a$

σ_n^o . normal component of the traction vector acting on a fracture plane at onset of failure

τ ..... shear stress

τ ..... shear component of the traction vector

τ .....time

τ' .....time

τ_{ij} .....shear stress component, $ij = ab$, bc, ca, $a^m b^m$, $b^{\psi} c^{\psi}$, ab^{ψ}, $c^{\psi} a, b^m c^{\psi}, c^{\psi} a^m$

τ_m ..... shear strain in the fibre misalignment frame at failure

τ_{mat}.....shear component of the traction associated with the driving strain for the matrix failure mode (σ_{mat})

τ_{mc} ....shear strain in the fibre misalignment frame at failure by pure longitudinal compression

τ_L ..... longitudinal shear component of the traction vector in a potential matrix fracture plane

$\tau_L^{fric.}$ .....friction stress associated with the longitudinal direction

τ_T transverse shear component of the traction vector in a potential matrix fracture plane

τ_L^olongitudinal shear component of the traction vector acting on a fracture plane at onset of failure

τ_T^o . transverse shear component of the traction vector acting on a fracture plane at onset of failure

$\tau_T^{fric.}$ .....friction stress associated with the transverse direction

ϕ ... angle of the fracture surface with the through-the-thickness direction, for the matrix failure mode under a generic state of stress

ϕ_o .. angle of the fracture surface with the through-the-thickness direction, for the matrix failure mode under pure in-plane transverse compression

χ.....correction factor for the data reduction in an MMB test

$\chi(\gamma_{ab})$ ..... twice the strain energy associated with in-plane shear

$\chi\left(\gamma_{ab\mid is}^u\right)$ .....twice the strain energy associated with in-plane shear at failure

ψ .....angle of the fibre-kinking plane with the b axis, as shown in Fig. 3.15(b)

ψ_1 ..... first root of the angle of the fibre-kinking plane with the b axis

ψ_2 .....second root of the angle of the fibre-kinking plane with the b axis

ω . angle defined by the two shear components of the relative displacement vector, $\omega = \text{atan}\,\delta_3/\delta_2$

ω..angle of the magnitude of the traction σ_{mat} with the shear component τ_{mat} (see Fig. 4.4(b), $\omega = \arctan\langle\sigma_n\rangle/\tau_{mat}$)

Upper case Greek letters

Γ.....energy per unit area dissipated by a localized damage mode

Γ.....correction factor for the data reduction in an MMB test

Γ_a ..... energy release rate for the fibre tensile failure mode

Γ_b ..... mode I intralaminar fracture energy release rate (i.e. pure tensile failure, positive σ_n acting alone)

Γ_{kink} ..... energy release rate for the fibre kinking failure mode

Γ_v ..... energy per unit volume dissipated by a localized damage mode

Γ_L ..... energy release rate corresponding to τ_L acting alone

Γ_T ..... energy release rate corresponding to τ_T acting alone

Δ ..... displacement

Δ ... correction term applied to the crack length, from the ASTM standard for the DCB test [30]

$\mathbf{\Lambda}$ ..... tensor used to obtain the interaction energy

Λ_b^o . parameter used to obtain the energy release rate for an intralaminar slit crack

Λ_{bc}^o parameter used to obtain the energy release rate for an intralaminar slit crack

Π ..... potential energy, defined as $\Pi = U - F$

Operators

$\langle \cdot \rangle$ ..... Mc-Cauley bracket defined by $\langle x \rangle = \max\{0, x\}$, $x \in \mathbb{R}$

$\delta(\cdot)$ ..... Dirac delta function

Chapter 1

Introduction

Advanced composite materials, typically consisting of reinforcing fibres (e.g. carbon fibres) in a resin matrix (e.g. epoxy), are progressively replacing metals in the transport and defence industries. For this reason, it is important to understand and be able to predict the failure of composite structures, under static and dynamic loads.

The present knowledge on the failure behaviour of composite structures comes from two main sources: experimental and numerical. The experimental tests suffer from two main drawbacks. Firstly, they are considerably expensive and time consuming, particularly when different loading situations, impact orientations, velocities and morphologies of the structure are tested. Secondly, they can rarely be used in the earlier design stages, as the manufacturing capabilities may not be installed yet, and component testing might require a dedicated test set-up.

The capability to numerically model the failure and energy absorption of composite structures allows savings by postponing testing to final stages of design, and brings a deeper insight into the knowledge of material and structural failure. Once a numerical model of a particular component or complete structure is developed, several load cases, impact orientations and velocities can in principle be investigated at low cost. This can result in the definition of response maps, characterizing a component's structural and crashworthiness capabilities. The information obtained can then be used to further enhance the final design.

At the current state of development, numerical models cannot be totally trusted to model complex static or dynamic failure situations involving composite materials accurately. To a great extent, this is because the physics of composite materials failure is complex and not fully understood yet. Furthermore, failure models need to be implemented into numerical codes, if they are to be used to analyse complex structures. However, for the most commonly used numerical method, the Finite Element (FE) method, modelling failure is a complex issue, and raises difficult problems, which include, for example, mesh dependency, energy absorption and large element distortions.

The work in this thesis is restricted to laminated composites with unidirectionally reinforced plies, and its aims are:

- to investigate the physics of failure in laminated composites, and formulate failure models and criteria for each failure mode, which more accurately incorporate the physics of failure;
- to implement these models in an FE code which is used by the industry, and which should be able to model situations ranging from simple specimens to complex structures, in static and dynamic loading situations;
- to use, in the FE implementation, formulations which correctly model the energy absorbed by each failure mode. For delamination, this is achieved by using decohesion (or interface) elements, and for the other failure modes by using a smeared formulation;
- if necessary, to develop the experimental tests required to measure the material properties needed by the model.

In this context, in Chapter 2, a three-dimensional (3D) decohesion element with mixed mode capabilities is formulated and incorporated into the finite element code LS-Dyna [1] to model delamination. In Chapter 3, a 3D ply material model is formulated. The material model distinguishes matrix and fibre tensile and compressive failure, and includes nonlinear behaviour in shear. The matrix compressive failure mode is addressed with a modified 3D version of the Puck [2] matrix compression

failure criterion. For the fibre failure in compression, a 3D criterion based on Argon's [3] approach considering matrix failure prompted by material imperfections is used in a framework similar to the one proposed by Dávila et al. [4]. In Chapter 4, the 3D ply material model is implemented in LS-Dyna. On the post-failure behaviour, a smeared formulation is used, which allows for constant energy absorption, regardless of mesh refinement. Applications of the interface element and the ply failure model are presented. Analytical and experimental data are shown to be in good agreement with the numerical predictions. Experimental tests to measure the energy release rate associated with intralaminar fracture are presented in Chapter 5. For the tensile and compressive fibre-dominated failure modes, experimental tests to measure the associated energy release rates are presented in Chapter 6.

Chapter 2

Formulation and implementation of a decohesion element

2.1 Introduction

Initiation and propagation of delamination is often a precursor to ultimate failure in laminated composite structures. Knowledge of delamination and ability to model this aspect of failure therefore deserve particular attention.

In implicit Finite Element (FE) codes, decohesion elements have been successfully used to simulate standard delamination toughness tests (Double Cantilever Beam (DCB), Mixed-Mode Bending (MMB) and End Notch Flexure (ENF)) [5–10]; debonding of skin/stiffener specimens [6], overlap tests [11], compression after impact (CAI) of composite plates [5, 12] and crush of composite tubes [13].

In explicit analyses, nonlinear springs have been used to model the interfaces in layered composites [14]. Some work using a cohesive zone approach is presented in Refs. [15, 16], in which the applications include MMB specimens and the impact with penetration of a steel ball in a composite plate. However, very few details are given on the formulation and implementation. In another work, Borg et al. [17] used a discrete cohesive zone approach to model delamination. Coincident nodes were tied together with a penalty formulation before delamination onset. During damage propagation, the nodal forces were reduced to zero as the amount of dissipated

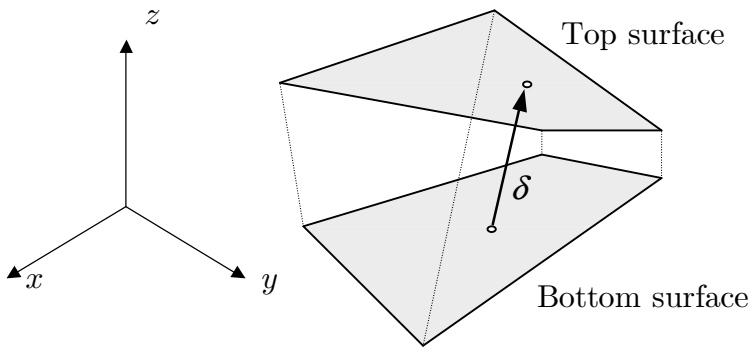

Figure 2.1: Decohesion model

work approached a value corresponding to the fracture energy, which was obtained from the energy release rate using the respective nodal area. The model was then modified to use a damage formulation [18], and was finally implemented within a contact algorithm [19, 20]. In the present work, a different approach is pursued, using decohesion elements, because they have proved to be an useful tool for implicit analyses.

Decohesion elements are typically formulated in terms of a traction vs. relative-displacement relationship instead of the traditional stress vs. strain relation. Generally, two surfaces (top and bottom) are considered, as shown in Fig. 2.1. Each point in each of these surfaces has a corresponding point on the other surface, designated as homologous. A pair of homologous points is a pair of points that are in contact before the interface is loaded. The relative displacement between each pair of homologous points is projected in a local reference system, which expresses the relative displacement in terms of an opening mode and a sliding mode. Sliding can be due to mode II or mode III loading (or a combination of both).

Prior to delamination onset, an elastic constitutive law usually relates the relative displacement of two homologous points with the traction (force per unit area) acting on both the top and bottom surfaces. For pure mode I or pure shear mode problems, the interface is usually considered to have an elastic behaviour (linear or not), until the respective maximum allowable stress is reached. Then, the stiffness is reduced in such a way that the energy absorbed per unit area is equal to the corresponding critical energy release rate (G_{Ic} or G_{Sc} respectively). For mixed-mode problems,

the elastic relationship is valid until a stress-based initiation criterion is verified. From this stage onwards, the stiffness is reduced for each mode ratio in such a way that the energy absorbed in the mixed-mode situation is defined by a propagation criterion.

LS-Dyna [1] is one of the explicit FE codes most widely used by the industry to model impact or crash situations in laminated composite materials. However, decohesion elements are not available within this code. In this work, a decohesion element with a bilinear constitutive law is formulated and implemented in LS-Dyna. The formulation is based on published work [5, 10, 13]. Due to stability limitations which are identified with the discontinuities in the bilinear law, two other constitutive laws are also developed. One of these constitutive laws is a third-order polynomial, and the other is a combination of linear and third-order polynomial segments. These two constitutive laws are implemented together with the bilinear law within a new decohesion element, using an enhanced formalism. The three different constitutive laws are compared, and applications are presented in mode I, mode II and mixed mode I and II.

2.2 Bilinear constitutive law

2.2.1 Introduction

The bilinear formulation presented in this section is based on the formulation from Refs. [5, 10, 13], and a comparison with the work from Refs. [11, 12, 21] is performed.

Consider a point in an interface like the one in Fig. 2.2. The tractions t_i between the top and bottom surfaces of the interface at that point are related to the relative displacement δ_i at the same point for $i = 1, 2, 3$ (Fig. 2.2). The index value $i = 1$ corresponds to an opening mode (mode I), while the index values $i = 2$ and 3 correspond to a shear mode (mode II, III, or a combination of both). In decohesion-element formulations, the sliding mode is usually considered to represent both modes II and III because the distinction between mode II and III depends on the direction of the relative displacement between homologous points with respect to the orientation

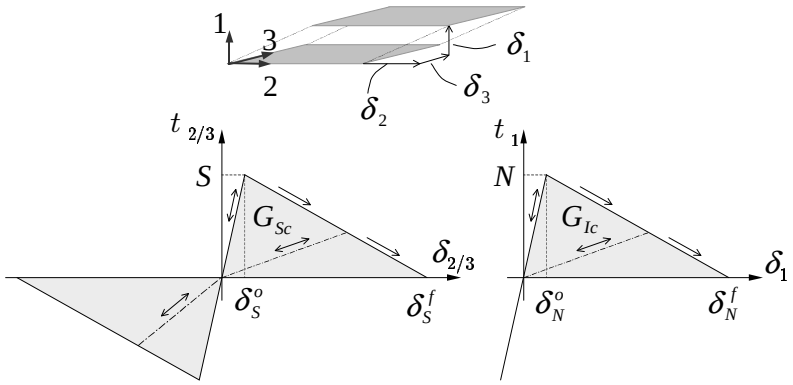

Figure 2.2: Bilinear constitutive law in single-mode loading

of the crack front. Without knowing how the crack front is oriented—and in a generic situation, with multiple crack growth, it might be difficult even to define it—it is impossible to distinguish between mode II and mode III.

The relative-displacements and tractions corresponding to the onset of damage are denoted as onset displacements and onset tractions respectively, and identified with the superscript 'o'. The relative displacements corresponding to complete decohesion are denoted final displacements and identified with the superscript 'f'.

Suppose a point loaded such that a relative displacement δ_i is applied parallel to one of the local axes ($i = 1, 2$ or 3). While the relative displacement has never exceeded its damage onset value, the point behaves elastically. Once the onset displacement is exceeded, some energy is dissipated. The total energy that can be dissipated at each point (per unit area of the interface) equals the critical energy release rate for the corresponding mode.

When the maximum traction N or S (according to the mode) is reached, the damage is assumed to start propagating. The corresponding onset displacements are, for the opening and shear modes respectively:

$$\delta_N^o = \frac{N}{k},\ \delta_S^o = \frac{S}{k} \tag{2.1}$$

where N and S are the mode I and shear mode maximum allowable tractions respectively. (The subscripts N and S on the onset displacements δ_N^o and δ_S^o indicate that these onset displacements correspond to the normal or shear traction acting alone, respectively.) When the traction reaches zero, the energy absorbed must

equal the critical energy release rate. This leads directly to the definition of the final displacements in a pure-mode loading situation as

$$\delta_N^f = \frac{2G_{Ic}}{k\delta_N^o} \qquad \text{and} \qquad \delta_S^f = \frac{2G_{Sc}}{k\delta_S^o}. \tag{2.2}$$

where G_{Ic} and G_{Sc} are the mode I and shear mode fracture toughnesses.

The maximum tractions N and S should be an estimate of the tensile and shear interfacial strengths, respectively. However, when modelling delamination propagation, it has often been found that the precise value of these strengths has little effect on the computed response [11].

2.2.2 Mixed mode

In a situation where more than one mode acts simultaneously, the damage starts propagating even before one of the limit tractions for pure mode loading (N or S) is attained individually—Fig. 2.3. In order to analyze this situation, the shear relative-displacement, δ_{shear}, and the magnitude of the relative displacement, δ, are defined as

$$\delta_{shear} = \sqrt{(\delta_2)^2 + (\delta_3)^2}, \qquad \delta = \sqrt{\langle\delta_1\rangle^2 + (\delta_{shear})^2} \tag{2.3}$$

where the operator $\langle\cdot\rangle$ is the Mc-Cauley bracket defined as $\langle x\rangle = \max\{0, x\}$, $x \in \mathbb{R}$. The shear traction is defined as

$$t_{shear} = \sqrt{(t_2)^2 + (t_3)^2} \tag{2.4}$$

and the participation of the different modes β, is defined as

$$\beta = \max\left\{0, \frac{\delta_{shear}}{\delta_1}\right\}. \tag{2.5}$$

The equivalent driving displacement δ leads to a unique definition of the state of deterioration in mixed mode, as proposed by Allix and Corigliano [22] in the framework of damage modelling. The onset relative-displacement, δ^o, is defined by a mixed-mode *initiation* criterion and the final relative-displacement, δ^f, is defined by a mixed-mode *propagation* criterion.

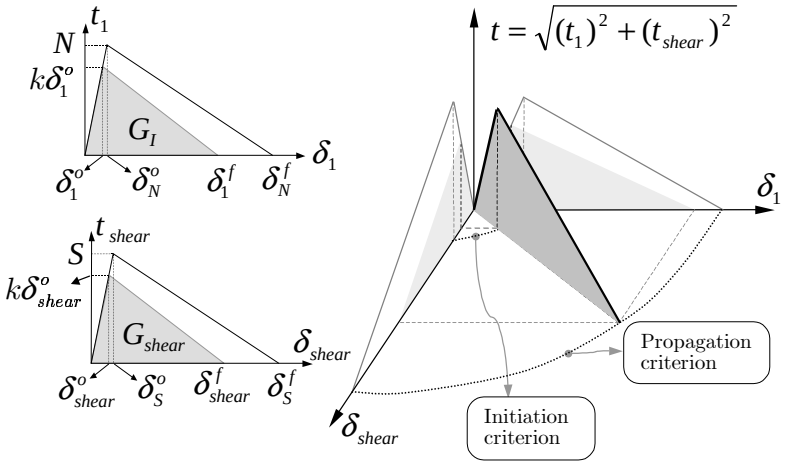

Figure 2.3: Mixed-mode behaviour for the bilinear law

2.2.2.1 Mixed-mode initiation criterion

The following quadratic delamination criterion is used, for it has proven to be suitable for delamination onset prediction in composite materials by other authors [23–25]:

$$\left(\frac{\langle t_1 \rangle}{N}\right)^2 + \left(\frac{t_{shear}}{S}\right)^2 = 1. \tag{2.6}$$

As tractions are a function of the relative displacements, the previous criterion may be expressed in terms of relative displacements resulting in

$$\delta^o = \begin{cases} \delta_S^o \delta_N^o \sqrt{\dfrac{1+\beta^2}{(\delta_S^o)^2 + (\beta\delta_N^o)^2}} \Leftarrow \delta_1 > 0 \\ \delta_S^o \Leftarrow \delta_1 \leq 0. \end{cases} \tag{2.7}$$

2.2.2.2 Mixed-mode propagation criterion

The mixed-mode propagation criterion establishes the state of complete decohesion for different ratios of applied mode I and shear mode energy release rates. There are several criteria that establish mixed-mode propagation. One of these, the power law criterion [11], can be expressed as

$$\left(\frac{G_I}{G_{Ic}}\right)^\alpha + \left(\frac{G_{shear}}{G_{Sc}}\right)^\alpha = 1. \tag{2.8}$$

Consider the energy absorbed up to the complete decohesion in a mixed-mode loading situation, for each mode. As the tractions are a function of the relative displace-

ments, the mode I and shear mode energy release rates may be expressed in terms of relative displacements. The energy absorbed by each mode in a mixed-mode loading is (Fig. 2.3)

$$G_I = \frac{k\delta_1^o \delta_1^f}{2} \quad \text{and } G_{shear} = \frac{k\delta_{shear}^o \delta_{shear}^f}{2}. \tag{2.9}$$

Introducing Eq. 2.9 in the expression of the power law criterion, Eq. 2.8, the expression for δ^f can be obtained as

$$\delta^f = \begin{cases} \dfrac{2\left(1+\beta^2\right)}{k\delta^o}\left[\left(\dfrac{1}{G_{Ic}}\right)^\alpha + \left(\dfrac{\beta^2}{G_{Sc}}\right)^\alpha\right]^{-1/\alpha} \Leftarrow \delta_1 > 0 \\ {\delta_S}^f \Leftarrow \delta_1 \leq 0. \end{cases} \tag{2.10}$$

For most carbon/epoxy composites, the mixed-mode data can be accurately represented using $1 \leq \alpha \leq 2$.

Similar expressions can be derived for other criteria. For instance, Benzeggagh and Kenane's criterion [26] uses the parameter η to describe the mixed-mode interface behaviour:

$$G_{Ic} + \left(G_{Sc} - G_{Ic}\right)\left(\frac{G_{shear}}{G_I + G_{shear}}\right)^\eta = G_I + G_{shear}. \tag{2.11}$$

Proceeding as before, but now using this criterion, the expression for the final relative displacement is obtained as

$$\delta^f = \begin{cases} \dfrac{2}{k\delta^o}\left[G_{Ic} + \left(G_{Sc} - G_{Ic}\right)\left(\frac{\beta^2}{1+\beta^2}\right)^\eta\right] \Leftarrow \delta_1 > 0 \\ {\delta_S}^f \Leftarrow \delta_1 \leq 0. \end{cases} \tag{2.12}$$

2.2.3 Constitutive law

In order to account for irreversibility, the maximum over time value of the mixed-mode displacement is defined as, at time τ,

$$\delta^{\max}(\tau) = \max_{\tau' \leq \tau}\left\{\delta\left(\tau'\right)\right\}. \tag{2.13}$$

Neglecting the interpenetration that occurs in the eventuality of compression, the constitutive law could be expressed very simply as

$$t_i = (1-d)\, k\delta_i \qquad \text{(no sum in } i\text{)} \tag{2.14}$$

where only one damage variable is used, and is defined as

$$d = \begin{cases} 0 \Leftarrow \delta^{\max} \leq \delta^o \\ \frac{\delta^f(\delta^{\max}-\delta^o)}{\delta^{\max}\left(\delta^f-\delta^o\right)} \Leftarrow \delta^o < \delta^{\max} \leq \delta^f \\ 1 \Leftarrow \delta^{\max} \geq \delta^f. \end{cases} \tag{2.15}$$

The expression for the damage variable above results directly from the definition of the onset and final relative-displacements, and the bilinear shape for the constitutive law. From Eq. 2.15, it follows that $d \in [0, 1]$.

In order to avoid interpenetration for compression situations, a simple contact logic already available in most FE codes could be used. Instead, the following condition is added to Eq. 2.14:

$$t_1 = k\delta_1 \Leftarrow \delta_1 \leq 0. \tag{2.16}$$

This constitutive law expressed by Eqs. 2.14 to 2.16 has only one damage variable d, and, in a mixed-mode situation, implies that the state of complete decohesion is attained *at the same time* for opening and shear loading.

2.2.4 Comparison to other formulations

The decohesion formulation presented is compared to the one proposed by Crisfield and co-workers in Refs. [11, 12, 21]. In those references, the following relation between relative displacements and tractions is proposed:

$$t_1 = \left(1 - \frac{\kappa}{1+\kappa}\frac{\delta_N^f}{\delta_N^f - \delta_N^o}\right) k\delta_1 \tag{2.17}$$

$$t_{shear} = \left(1 - \frac{\kappa}{1+\kappa}\frac{\delta_S^f}{\delta_S^f - \delta_S^o}\right) k\delta_{shear} \tag{2.18}$$

with

$$\kappa = \left\langle \left[\left(\frac{\langle\delta_1\rangle}{\delta_N^o}\right)^{2\alpha} + \left(\frac{\delta_{shear}}{\delta_S^o}\right)^{2\alpha} \right]^{1/(2\alpha)} - 1 \right\rangle. \tag{2.19}$$

This formulation verifies the power law for damage propagation, as expressed in Eq. 2.8. Fig. 2.4 compares the applications of both implementations in a mixed-mode loading situation with $\beta = 1/2$, for an interface with the following properties:

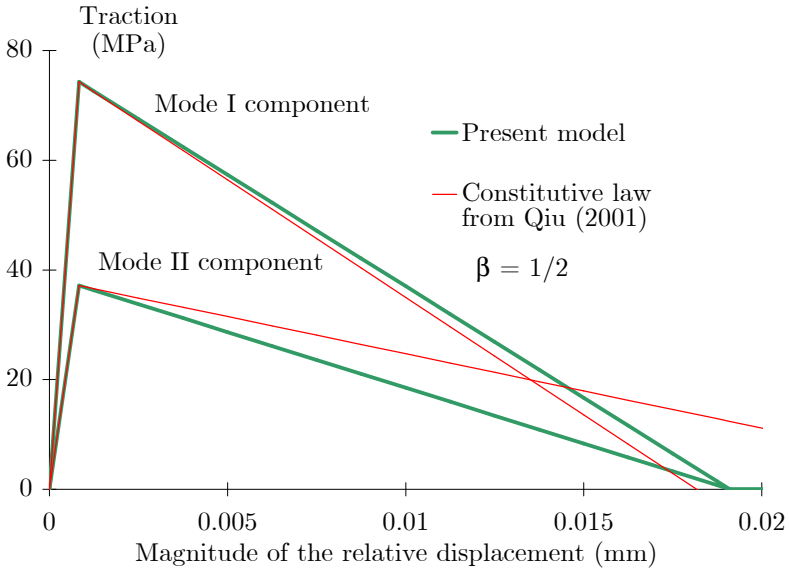

Figure 2.4: Comparison of two different decohesion models in mixed mode

$G_{Ic} = 0.7\,\mathrm{kJ/m^2}$, $G_{IIc} = 1.7\,\mathrm{kJ/m^2}$, $N = 80\,\mathrm{MPa}$, $S = 100\,\mathrm{MPa}$ and $k = 1 \times 10^5\,\mathrm{N/mm^3}$. For this comparison, the value $\alpha = 1$ is used for both formulations, as, for this case, the damage onset criterion expressed in Eq. 2.6 is also satisfied. Note that when damage starts propagating, the complete definition of the model requires the determination of the two different variables δ_1^f and δ_{shear}^f. However, only one equation is available: the one that results from the application of a propagation criterion. The other condition, implicitly considered in the model presented, is that the interface should attain the state of complete decohesion at the same time for normal and shear components of the traction, as can be observed in Fig. 2.4. On the other hand, for the model proposed in Refs. [11, 12, 21], complete decohesion is attained at different times for the opening and shear modes. In Ref. [21], it is recognized that this goes against experimental evidence; it is however argued that this problem can be simply overcome by considering different penalty stiffness values for mode I and mode II, so as to achieve $\delta_N^o/\delta_N^f = \delta_S^o/\delta_S^f$. All formulations presented in the present work avoid this requirement.

2.2.5 Varying mode ratio

In this formulation, the irreversibility of damage is considered through the definition of the maximum magnitude of the relative displacement (Eq. 2.13).

Consider a situation where the mode ratio at a given material point is constant in time. In this case, if unloading occurs after damage onset, then the point will linearly unload towards the origin and the maximum relative displacement that once existed at that point is recorded in the variable $\delta^{\max}$. When re-loading, no energy is absorbed until $\delta^{\max}$ is reached again. When complete decohesion occurs, the energy absorbed is the one defined by the propagation criterion, and does not depend on the loading/unloading sequence.

Consider now a more generic situation, where the mode ratio (at a given point) does change throughout the loading, in the damage propagation phase, Fig. 2.5. In this figure, a point has been loaded in mode I (vertical axis) and damage started propagating until it reached the point denoted by '1'. Suppose that in a numeric incremental implementation, the next equilibrium point is '2'. There is no trivial answer to what the memory of damage would be for this new mode ratio, and how much energy should still be available to be absorbed.

One possibility to address this issue in a decohesion formulation is that, at any load step, the maximum mixed-mode displacement is considered to provide a memory of the damage evolution, regardless of the mode ratio. In Fig. 2.5, this methodology is represented by the circle drawn from the initial point '1'. Another possibility, from Refs. [12, 21], consists in storing the maximum value in time of the variable κ in Eq. 2.19. This approach is represented in Fig. 2.5 for the particular case of $\alpha = 1$, by the ellipse starting from point '1'. Provided the mode ratio does not change substantially, then the two approaches are very similar.

2.2.6 Implementation

The decohesion model presented has been implemented in LS-Dyna [1] as a user material within a brick element. This approach for the implementation has the implication of requiring to model the resin rich layer (for the case of delaminations)

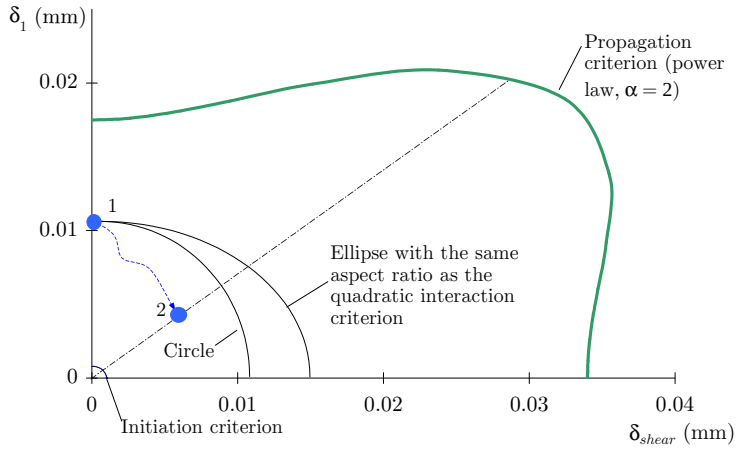

Figure 2.5: Varying mode ratio at a point

as a nonzero thickness medium. However, the resin rich layer has, in fact, a finite thickness, and mass scaling can be used to obtain faster solutions when applying the decohesion element to quasi-static situations. Note that the volume associated with the decohesion element can in fact be set to be very small by using a small thickness (0.01 to 0.001mm) and the element's kinetic energy arising from this be still several orders of magnitude below its internal energy, which is an important consideration for quasi-static analyses. Within the user material, the nodal displacements and the strains are known, and the stress tensor must be provided. The only nonzero components of the stress tensor correspond to the components of the traction vector, whose determination is straight-forward using the presented formulation, which requires storing $\delta^{\max}$ as a history variable.

2.3 Two other constitutive laws

2.3.1 Introduction

The bilinear constitutive law presented in the previous section allows the modelling of delamination in composite materials and has been successfully used by several authors in implicit analyses [5, 10, 13]. Several authors have proposed different shapes for the traction vs. relative displacement laws, e.g. Refs. [9, 27, 28]. Williams and

Hadavinia [29] derived analytical solutions using different cohesive zone traction laws for a cantilever beam specimen, using a beam on elastic foundation model. They concluded that the results showed insensitivity to the form of the traction law, for any of the five laws studied. It can thus be asserted that the shape of the interface law is not of extreme importance, provided the fracture toughness is correctly accounted for, and that the initial stiffness and maximum traction are reasonably consistent with the stiffness and strength of the material being modelled. However, there is little information on the stability of different shapes of the constitutive law in explicit FE codes.

It will become evident in the remainder of this work that the two discontinuities existing in the bilinear law (at peak value and complete decohesion) generate numerical instabilities in an explicit implementation. In certain situations, a stress wave is generated at those points, and this excites high-frequency vibrations that completely break the decohesion elements in the vicinity. It is possible to overcome this problem by using damping algorithms, higher mesh refinement, lower interface strength, higher fracture toughness or lower load-rate. However, the particular finite element model that is not affected by these shock waves is not always straight forward to define.

For those reasons, two alternative constitutive laws are proposed and implemented in LS-Dyna [1]. The shape of the first law is a curve, and is defined by a third order polynomial function as proposed in Ref. [27]:

$$t = \frac{27}{4} t^o \left(1 - \frac{\delta}{\delta^f}\right)^2 \frac{\delta}{\delta^f}. \tag{2.20}$$

It can be easily shown that the maximum value of the traction in Eq. 2.20 is t^o, which corresponds to damage onset. It can also be shown that the maximum traction corresponds to a relative displacement $\delta = \delta^f/3$. The final displacement in a single-mode loading can be related to t^o and the energy dissipated per unit area G_c by

$$\delta^f = \frac{48}{27} \frac{G_c}{t^o}. \tag{2.21}$$

The function in Eq. 2.20 has no discontinuities, and the slope at complete decohesion is zero, which renders the complete failure of the element much smoother—Fig.

2.6(a) and (b). In order to introduce a damage variable (which is useful to define the mixed-mode behaviour, irreversibility, for post-processing, and for uniformity of the implementation), Eq. 2.20 can be expressed as

$$t = k\,(1-d)\,\delta \tag{2.22}$$

where $k = 27t_o/4\delta^f$, $d = 1$ for $\delta > \delta^f$, and

$$d = 2\frac{\delta}{\delta^f} - \left(\frac{\delta}{\delta^f}\right)^2 \quad \text{for} \quad \delta \leq \delta^f. \tag{2.23}$$

The second alternative constitutive law proposed and implemented in LS-Dyna [1] is similar to the bilinear, in the sense that it is characterized by a linear-elastic behaviour before failure onset. However, it is also similar to the third order polynomial constitutive law, in the sense that discontinuities are smoothed by using a third-order polynomial. The constitutive law, shown in Fig. 2.6(c) and (d), can be expressed by Eq. 2.22, but with the damage variable defined as $d = 0$ for $\delta \leq \delta^o$, $d = 1$ for $\delta > \delta^f$, and

$$d = 1 - \frac{\delta^o}{\delta}\left[1 + \left(\frac{\delta-\delta^o}{\delta^f-\delta^o}\right)^2\left(2\frac{\delta-\delta^o}{\delta^f-\delta^o} - 3\right)\right] \quad \text{for} \quad \delta^o < \delta \leq \delta^f. \tag{2.24}$$

The constitutive law defined by Eqs. 2.22 and 2.24 has zero slope at failure onset, resulting in a discontinuity which is less severe than the one existing for the bilinear formulation, and the slope at complete decohesion is zero, which renders complete failure smoother.

2.3.2 Constitutive law

The bilinear formulation presented in the previous section is based on previous work [5, 10, 13], and for consistency with that work, the mixed-mode ratio was defined as $\beta = \delta_{shear}/\delta_1$. However, this definition implies that a division by zero occurs for pure shear mode loading, which has to be considered as a particular case in the numerical implementation. An alternative definition is therefore used in this section, which avoids this division by zero: $\theta = \text{acos}\left(\langle\delta_1\rangle/\delta\right)$, $\theta \in [0, \pi/2]$. The contribution of the different shear components is defined as $\omega = \text{atan}\left(\delta_3/\delta_2\right)$, $\omega \in [0, 2\pi[$.

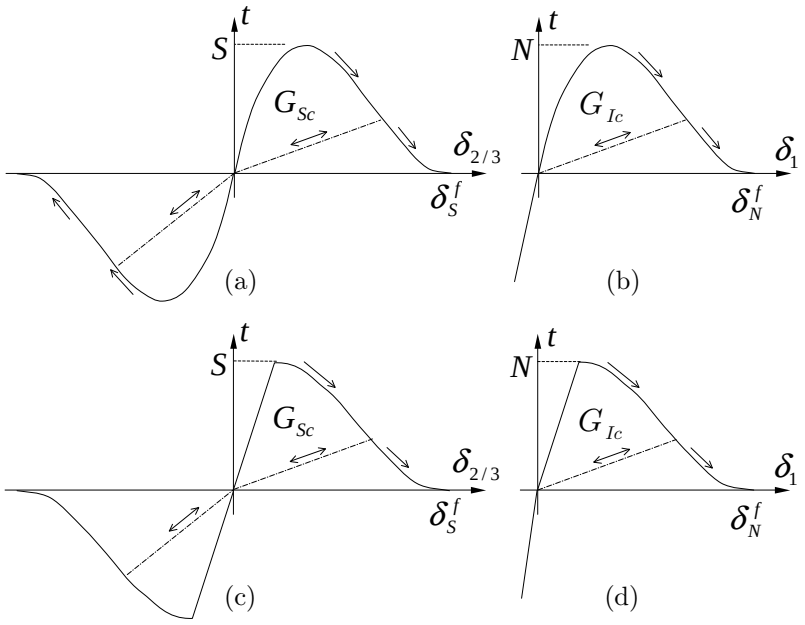

Figure 2.6: Third-order polynomial constitutive law (a) shear mode and (b) opening mode; linear/ polynomial constitutive law (c) shear mode and (d) opening mode

The constitutive law of the interface element, expressed on the direction of the relative displacement, is defined as

$$t = k_{pos}\,(1-d)\,\delta \tag{2.25}$$

where k_{pos} is an input parameter for the bilinear and the linear/polynomial constitutive laws, but is computed as $k_{pos} = 27t_o/4\delta^f$ for the third order polynomial law. The traction components are recovered as

$$t_1 = t\cos\theta, \qquad t_{shear} = t\sin\theta \tag{2.26}$$

$$t_2 = t_{shear}\cos\omega, \qquad t_3 = t_{shear}\sin\omega \tag{2.27}$$

with the following condition added to prevent interpenetration:

$$t_1 = k_{neg}\delta_1 \Leftarrow \delta_1 \leq 0 \tag{2.28}$$

where k_{neg} is the penalty stiffness, also given to the model as an input parameter.

2.3.3 Mixed-mode behaviour

2.3.3.1 Initiation criterion

The initiation criterion used in the bilinear constitutive law of the previous section, Eq. 2.6, is also used here. When applied to this formulation, the expression for the magnitude of the onset traction is

$$t^o = \left[\left(\frac{\cos\theta}{N} \right)^2 + \left(\frac{\sin\theta}{S} \right)^2 \right]^{-1/2} . \tag{2.29}$$

For the bilinear and the linear/polynomial constitutive laws, the onset relative displacement needs to be defined and is obtained as

$$\delta^o = t^o / k_{pos} \tag{2.30}$$

where k_{pos} is the elastic stiffness.

2.3.3.2 Propagation criterion

Using the power law (Eq. 2.8) for the propagation criterion, and using the definition of the participation of each mode ratio θ, Eq. 2.8 can be manipulated to obtain the fracture toughness G_c as

$$G_c = \left[\left(\frac{\cos^2\theta}{G_{Ic}} \right)^\alpha + \left(\frac{\sin^2\theta}{G_{Sc}} \right)^\alpha \right]^{-1/\alpha} . \tag{2.31}$$

Benzeggagh and Kenane's criterion [26] (Eq. 2.11) can also be used instead of the power law, resulting in

$$G_c = G_{Ic} + (G_{Sc} - G_{Ic}) \left(\sin^2\theta \right)^\eta . \tag{2.32}$$

The final relative-displacement can then be obtained as

$$\delta^f = \begin{cases} \dfrac{2G_c}{t^o} \text{ (bilinear and linear/ polyn. laws)} \\ \dfrac{48}{27}\dfrac{G_c}{t^o} \text{ (3^{rd} order polynomial law).} \end{cases} \tag{2.33}$$

2.3.4 Irreversibility

Irreversibility can be addressed by storing the maximum value in time of the magnitude of the relative displacement δ. This approach was followed in the previous section, for consistency with the work on which it was based [5, 10, 13]. Other similar approaches are possible, such as storing the maximum value in time of the variable δ/δ^o or of the variable δ/δ^f. With any of these approaches however, it cannot be always and simultaneously guaranteed that a point at the stage of damage propagation will not become completely undamaged or fully damaged, just as a result of a change in the mode ratio. Also, with some of the previous approaches, and in particular with the one implemented in the previous section, a fully damaged point could become only partially damaged as a result of just a change in the mode ratio. These assertions can be better visualized using Fig. 2.5.

An approach that avoids the mentioned limitation, and which is eventually more intuitive, consists of storing the maximum value in time of the damage variable itself. With the latter approach, the instantaneous value of the damage variables are defined as

$$d^{inst} = \begin{cases} 0 \Leftarrow \delta \leq \delta^o \\ \frac{\delta^f(\delta-\delta^o)}{\delta\left(\delta^f-\delta^o\right)} \Leftarrow \delta^o < \delta \leq \delta^f \\ 1 \Leftarrow \delta \geq \delta^f \end{cases} \quad \text{(bilinear law)} \tag{2.34}$$

$$d^{inst} = \begin{cases} 2\frac{\delta}{\delta^f} - \left(\frac{\delta}{\delta^f}\right)^2 \Leftarrow \delta \leq \delta^f \\ 1 \Leftarrow \delta \geq \delta^f \end{cases} \quad (3^{rd} \text{ order polynomial law}) \tag{2.35}$$

$$d^{inst} = \begin{cases} 0 \Leftarrow \delta \leq \delta^o \\ 1 - \frac{\delta^o}{\delta}\left[1 + \left(\frac{\delta-\delta^o}{\delta^f-\delta^o}\right)^2\left(2\frac{\delta-\delta^o}{\delta^f-\delta^o} - 3\right)^2\right] \Leftarrow \delta^o < \delta \leq \delta^f \\ 1 \Leftarrow \delta \geq \delta^f \end{cases} \quad \text{(Linear/polyn. law)} \tag{2.36}$$

and the damage variable itself is obtained from the instantaneous value as

$$d(\tau) = \max_{\tau' < \tau} \left\{ d^{inst}(\tau') \right\}. \tag{2.37}$$

For the 3^{rd} order polynomial law, Eq. 2.37 can be modified so that a reversible

nonlinear elastic behaviour exists before damage onset, resulting in

$$d(\tau) = \begin{cases} d^{inst}(\tau) \Leftarrow d \leq 5/9 \\ \max\limits_{\tau' < \tau} \{d^{inst}(\tau')\} \Leftarrow d > 5/9 \end{cases} \quad (3^{rd} \text{ order polynomial}). \tag{2.38}$$

2.3.5 Implementation

The third-order polynomial, linear/polynomial and bilinear decohesion models presented have also been implemented in LS-Dyna [1] as a user material within a brick element. The implementation is similar to the previous bilinear one, except that the damage variable d is now stored as a history variable, instead of the maximum displacement $\delta^{\max}$. Also, the implementation is made within a single user element, and the user can specify which constitutive law to use via the input file.

2.4 Benchmark applications (quasi-static)

Even though the decohesion element has been implemented in LS-Dyna for dynamic analyses essentially, the benchmark tests presented in this section are quasi-static. Modelling quasi-static problems with an explicit FE code is bounded by some constraints. System damping has to be used to damp the dynamic vibrations, and the analysis requires a large number of time steps (during which numerical errors can potentially accumulate, and external work can be converted into energy forms other than internal, such as kinetic, hourglass control, and damping). The displacement rate in the following examples was chosen in such way that, while guaranteeing that the kinetic and damping energy are negligible and the vibrations acceptable (thus guaranteeing the simulation of a quasi-static case), the CPU run time was kept under a few hours. For considerably more complex problems, the analysis time can still be reasonably low, by using several CPUs in parallel. However, there are advantages of using explicit codes for quasi-static problems, since decohesion elements implemented in implicit codes usually have difficulties converging for large displacements, which does not happen for explicit codes. Finally, it is worth mentioning that most tests in this section could have been modelled more efficiently having used 2D elements, but, as stated, they are intended as benchmarks. In the following examples,

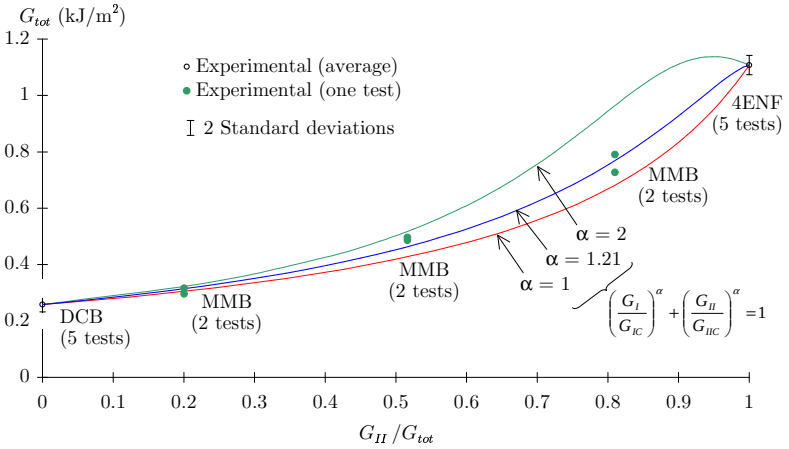

Figure 2.7: Total fracture toughness, as a function of mode ratio

the bilinear formulation from Section 3 has been used, as opposed to the one from Section 2 (note that the two bilinear formulations are coincident for all examples, since the mode ratio does not change).

2.4.1 Fracture toughness tests

The mechanical properties of a carbon-epoxy prepreg (T300/913, supplied by Hexcel) were measured experimentally (see Appendices A and B). Mode I (DCB, [30]), mode II (4ENF, [31, 32]) and mixed mode (MMB, [33]) tests were carried. The main results from these tests are presented graphically in Fig. 2.7. To characterize the mixed-mode behaviour, the power law (with coefficient $\alpha = 1.21$) was found to give the best fit to the mixed-mode data. This value of α has therefore been used in the simulations. The average mode I and mode II fracture toughness were determined as $G_{Ic} = 0.258\,\mathrm{kJ/m^2}$ and $G_{IIc} = 1.08\,\mathrm{kJ/m^2}$.

2.4.1.1 Mode I

One of the DCB specimens from the mentioned test program (Appendix B), was chosen to be simulated. The specimen was 20 mm wide, 3.1 mm thick and the pre-crack length was 53 mm—Fig. 2.8. The average mode I fracture toughness registered during the test is $G_{Ic} = 0.268\,\mathrm{kJ/m^2}$ and the flexural Young's modulus is $E = 119\,\mathrm{GPa}$. The maximum mode I traction was taken as $N = 60\,\mathrm{MPa}$, which

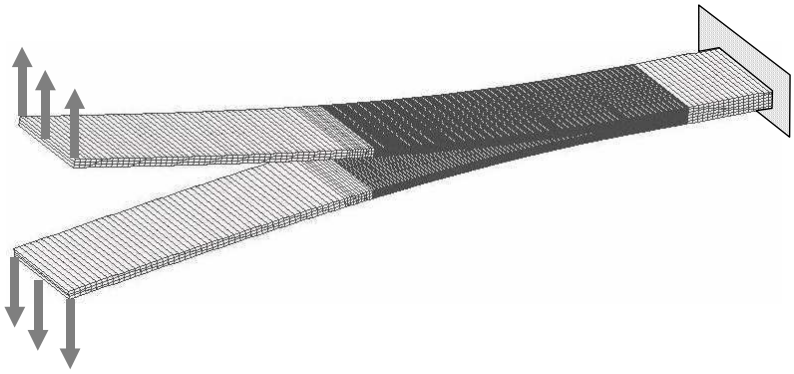

Figure 2.8: Numerical model of a DCB specimen

is representative of the interface strength, and the penalty stiffness as $k = k_{pos} = k_{neg} = 1 \times 10^5\,\mathrm{N/mm^3}$ (the use of much smaller values of maximum traction or penalty stiffness would result in failing to correctly represent the behaviour of the specimen before crack propagation). The minimum decohesion-element length in the numerical model was 0.2 mm , which ensured that at least 4 decohesion elements were contained in the cohesive zone at any time, thus ensuring a smooth solution [11]. A displacement-rate of 560 mm/s was applied to the appropriate points of the model. Each arm of the specimen was modelled using 1-integration point 8-noded brick elements, with 3 elements across the thickness, and considered isotropic with $E = 119\,\mathrm{GPa}$ and $\nu = 0.3$. The model ran in ≈ 5 hours (using a 2.4GHz Pentium IV computer).

The load vs. displacement curves obtained from the simulation are presented in Fig. 2.9, together with experimental data and the analytical solution for propagation.

It can be observed that the numerical curves slightly over-estimate the load for large displacements. The error in the fracture energy absorbed by each failed element is monitored and found to be under 0.0025% for all formulations. The difference between analytical and numerical is thus essentially due to other factors which include kinetic, hourglass-control and damping energy in the model, as well as accumulation of round-off errors during the analysis.

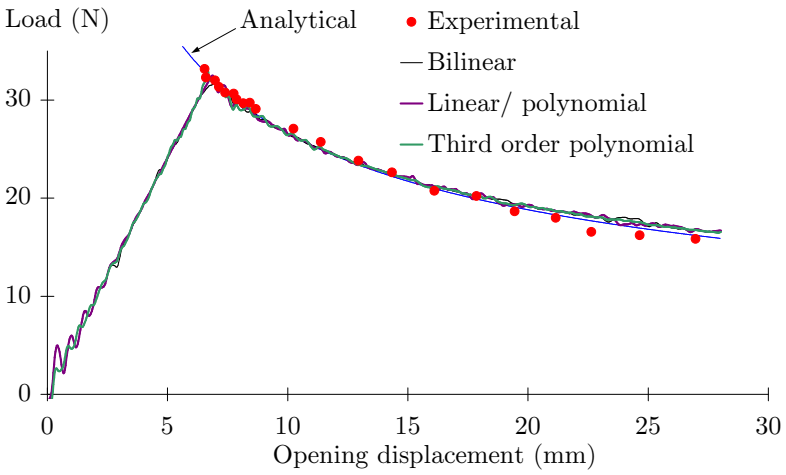

Figure 2.9: Experimental, analytical and numerical load vs. displacement curves for a DCB specimen

2.4.1.2 Mode II

A particular 4ENF specimen from the mentioned test program (Appendix B) was chosen to be simulated. The specimen was 20 mm wide, 3.1 mm thick and the pre-crack length was 25 mm. Part of the loading rig was modelled as well, in order to account correctly for the boundary conditions, as shown in Fig. 2.10. The measured fracture toughness, $G_{IIc} = 1.11\,\mathrm{kJ/m^2}$, was used in the simulation, and the flexural modulus was taken as $E = 137\,\mathrm{GPa}$. The maximum mode II traction was taken as $S = 60\,\mathrm{MPa}$. The minimum decohesion element length was 0.5 mm. A displacement-rate of 240 mm/s was applied to the appropriate points of the model. Each arm of the specimen was modelled using 1-integration point 8-noded brick elements, with 3 elements across the thickness, and considered isotropic with $E = 137\,\mathrm{GPa}$ and $\nu = 0.3$. The model ran in ≈ 2 hours (using a 2.4GHz Pentium IV computer).

The maximum error in the energy absorbed by each element is under 1% for all formulations. With the exception of the harmonic vibrations related to the dynamic loading, the numerical results fit very well the analytical and experimental ones, Fig. 2.11.

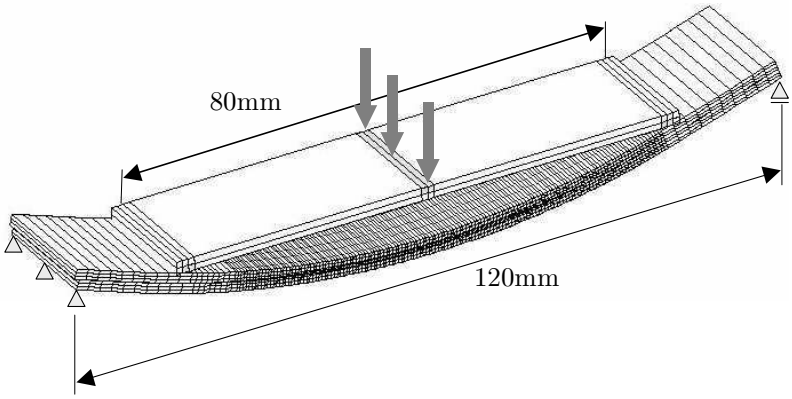

Figure 2.10: Mesh and loading body for the 4ENF specimen

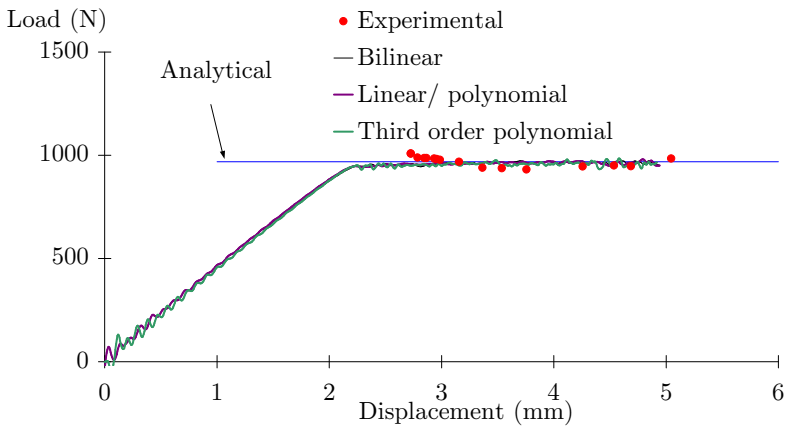

Figure 2.11: Experimental, analytical and numerical load vs. displacement curves, for an ENF specimen

2.4.1.3 Mixed mode

The simulation of an MMB test also requires modelling of the test fixture, as shown in Fig. 2.12. The specimen modelled was 20 mm wide, 3.1 mm thick and the pre-crack length was 33 mm. The distances between loading points are shown in Fig. 2.12. The fracture toughness values used in this simulation were an average of the tests performed (Appendix B): $G_{Ic} = 0.258\,\mathrm{kJ/m^2}$, $G_{IIc} = 1.108\,\mathrm{kJ/m^2}$, and, as reported earlier, the power law parameter α was determined to be 1.21. The flexural modulus obtained from the test was $E = 112\,\mathrm{GPa}$. The maximum mode I and mode II tractions were taken as $N = S = 60\,\mathrm{MPa}$. The minimum decohesion element length was 0.25 mm. A displacement-rate of 60 mm/s was applied to the appropriate points of the model. Each arm of the specimen was modelled using 1-integration point 8-noded thick-shell[1] elements, with 1 element across the thickness, and considered isotropic with $E = 112\,\mathrm{GPa}$ and $\nu = 0.3$. The model ran in ≈ 3 hours (using a 2.4GHz Pentium IV computer).

There is a good agreement between the numerical, analytical and experimental data, as shown in Fig. 2.13. Note that in this case, a significant part of the difference between numerical and analytical curves results from two factors not present in pure-mode loading situations: the decohesion element (i) interpolates the mixed-mode fracture toughness using the power law, and (ii) obtains the mode ratio from the ratio of relative displacements, and the latter ratio might be influenced by the vibrations in the model.

2.4.2 Isotropic circular plate under transverse point load

An isotropic circular plate is loaded by a single point load at the centre, and a circular delamination is assumed to start in the mid-surface of the plate. The failure load is independent of the delamination size and the axissimetric plate boundary conditions. The failure load at which a delamination starts propagating is given

[1] Thick-shell elements [1] are 8-noded solid elements with a shell formulation which allows each arm of the specimen to be modelled with 1 element only, thus saving computational time. These elements could have also been used for the other examples.

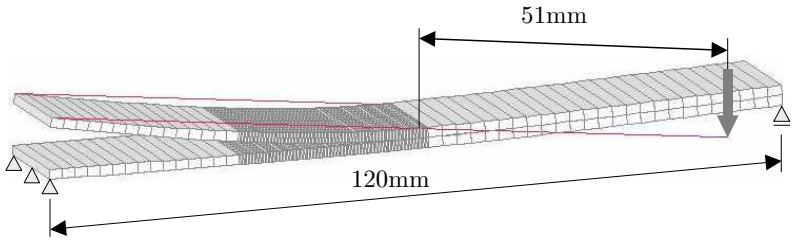

Figure 2.12: Finite element model of the MMB test and boundary conditions

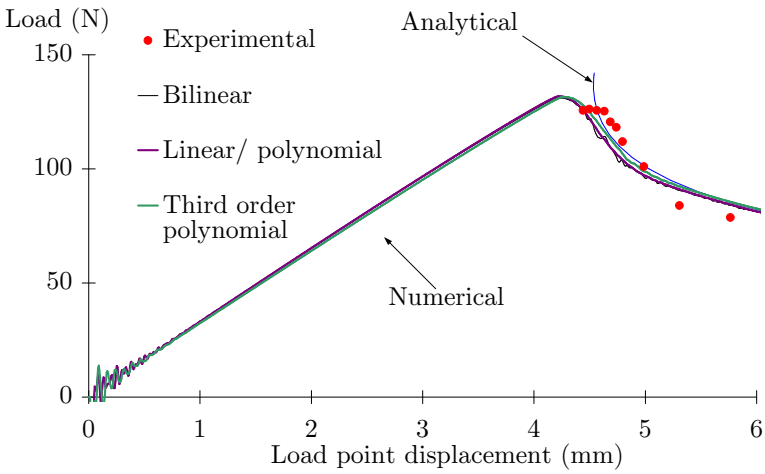

Figure 2.13: Experimental, analytical and numerical load vs. displacement curves for an MMB specimen

analytically by the expression [34]

$$P = \sqrt{\frac{8\pi^2 E t^3}{9\,(1-\nu^2)} G_{IIc}} \tag{2.39}$$

which neglects both membrane and geometrically nonlinear effects. In Eq. 2.39, P is the failure load, E is the Young's modulus, ν is the Poisson's ratio, t is the thickness of the plate and G_{IIc} is the mode II fracture toughness. This benchmark has been simulated for a simply supported plate with diameter $100\,\text{mm}$, for the values $E = 600\,\text{GPa}$, $\nu = 0.3$, $t = 3\,\text{mm}$ and $G_{IIc} = 0.1\,\text{kJ/m}^2$. These values were chosen so that the delamination propagates for a small deflection of the plate, well in the domain of application of Eq. 2.39. The minimum decohesion element length was $0.3\,\text{mm}$. A displacement-rate of $100\,\text{mm/s}$ was applied to the appropriate points of the model. The plate was modelled using 1-integration point 8-noded thick-shell elements, with 2 element across the thickness. The model ran in ≈ 4 hours (using a 2.4GHz Pentium IV computer).

Figs. 2.14(a)-(e) show the propagation of the delamination, with the colour scale representing the damage variable, thus identifying the cohesive zone. The fully-failed elements are deleted from the analysis. The three different material laws give almost coincident results. It can be observed that the circular shape of the delamination is also well simulated, even when the mesh is not radial. The load vs. displacement curve is shown in Fig. 2.14(f), where it can be observed that the crack propagation load from Eq. 2.39 is well predicted.

2.5 Effect of the constitutive law on numerical stability

The three different decohesion-element constitutive laws implemented in LS-Dyna are compared in test cases which are designed to test the limits of their stability. For decohesion elements implemented in explicit codes, stability is affected negatively by coarse meshes, high maximum tractions in the interface and low fracture toughness (because these factors result in fewer elements in the cohesive zone). Discontinuity

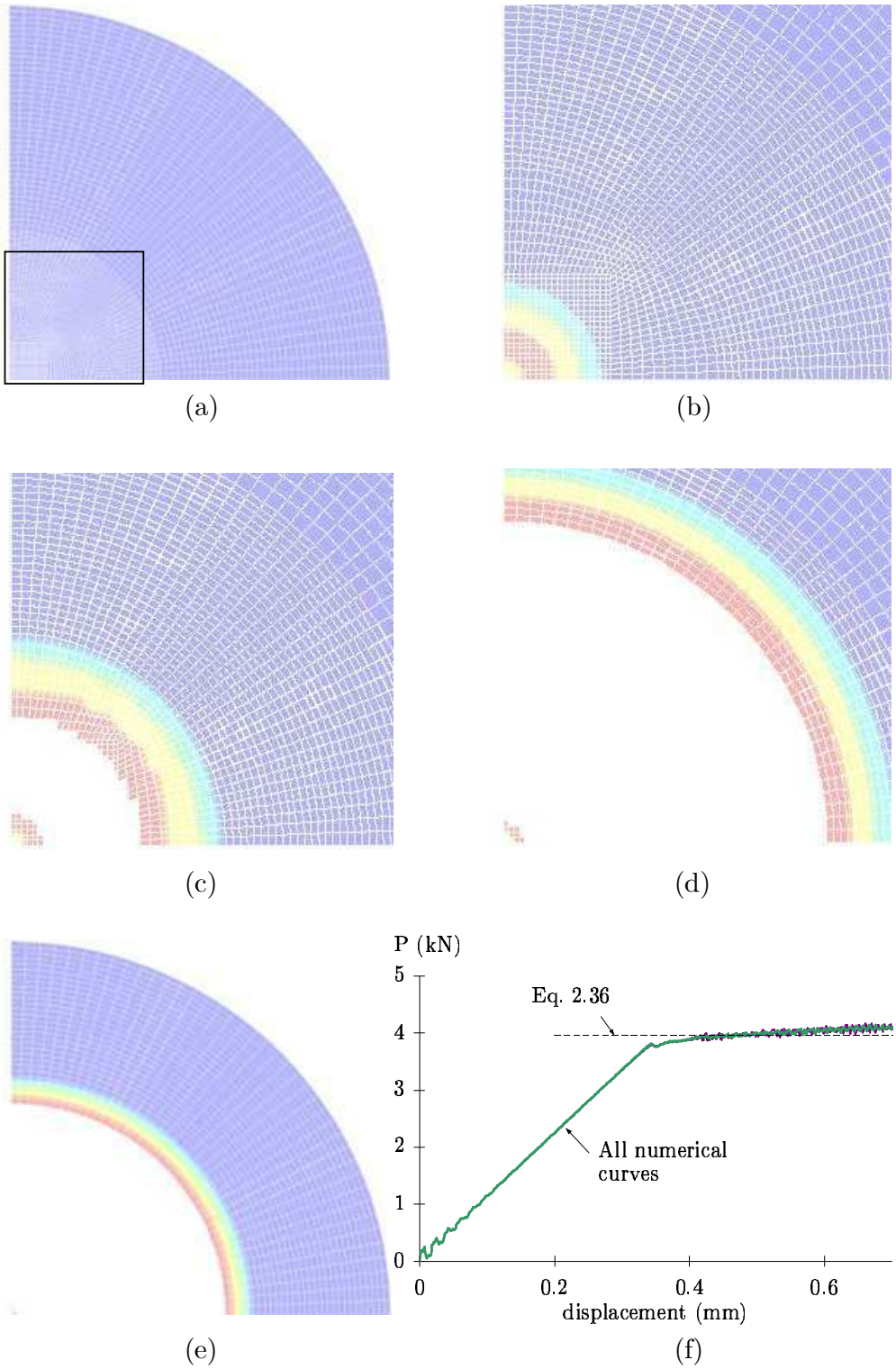

Figure 2.14: Decohesion elements layer, (a) before loading and (b)-(e) during crack propagation ((b)-(d) are zoomed in, as represented in (a)); (f) load vs. displacement curve

points in the constitutive law, like those in the bilinear formulation, also affect stability negatively, as shock waves are generated when the elements fail; this effect is found to be more pronounced at higher load-rates, probably due to the higher kinetic energy of the model [35]. Increasing the value of the stiffness accentuates the discontinuity at delamination onset, and thus also affects stability negatively. However, if extremely low values of stiffness are used, the elastic behaviour before delamination onset might not be properly captured and interpenetration might result in compression.

One example examining the limits of stability of the three decohesion laws, consists of a pure mode I DCB test of a carbon-PEEK composite, with material properties $E = 150\,\text{GPa}$, $G_{Ic} = 0.7\,\text{kJ/m}^2$ and density $\rho = 10^3\text{Kg/m}^3$. For the maximum traction, two values $N = 50\,\text{MPa}$ and $N = 80\,\text{MPa}$ are compared. The penalty stiffness used is $k = k_{pos} = k_{neg} = 1 \times 10^5\,\text{N/mm}^3$. The specimen is $25\,\text{mm}$ wide and $3\,\text{mm}$ thick, with a pre-crack length of $33\,\text{mm}$. The length of each decohesion element is $0.37\,\text{mm}$, which ensured that about $3 - 4$ decohesion elements were in the cohesive zone at any time (Mi et al. [11] found that at least 2 decohesion elements had to be included in the cohesive zone in order to achieve a reasonably smooth solution). A high displacement-rate of $4000\,\text{mm/s}$ is applied to the specimen, up to an opening displacement of $8\,\text{mm}$. The test lasted 2ms, with increments of $\approx 2 \times 10^{-5}\text{ms}$. The displacement rate is considered high, in the sense that it leads to a high relative-displacement rate in the decohesion elements. This high relative-displacement rate results in fewer interpolation points in the interface law which, combined with dynamic effects, results in reduced stability.

Fig. 2.15(a) presents the load vs. displacement curve obtained with the three constitutive laws implemented[2], for a maximum traction $N = 50\,\text{MPa}$; and Fig. 2.15(b) presents the same results for a maximum traction $N = 80\,\text{MPa}$. Both figures show the analytical curve corresponding to damage propagation, using simple beam theory and treating the specimen arm as built-in at the crack tip.

While all formulations were found to be stable at lower imposed displacement-

[2]The two formulations with the bilinear law (Sections 2 and 3) are coincidental, provided that the mode ratio does not change during the analysis, as is the case with this example.

rates, the bilinear formulation leads to a severe instability once the crack starts propagating, for this fast loading. However, the other constitutive laws are able to model the smooth and progressive crack propagation. The vibrations observed during crack propagation for the linear and for the linear/ polynomial laws are more pronounced for higher maximum tractions in the interface. For the bilinear law, higher tractions resulted in a more severe instability (bigger crack jump). The crack jumps can be observed[3] in Fig. 2.15(c) for $N = 50\,\mathrm{MPa}$, and Fig. 2.15(d) for $N = 80\,\mathrm{MPa}$.

2.6 Conclusions

Three different constitutive laws were implemented within an interface element formulation, into the standard LS-Dyna [1] explicit dynamic code. The formalism used is relatively simple and modular, allowing other constitutive laws to be added easily. Initiation criteria (which define the maximum traction in mixed-mode situations), and propagation criteria (which define the energy absorbed in mixed-mode situations) can also be added taking advantage of the modularity of the implementation.

When under less favorable numerical conditions (e.g. DCB loaded at 4000mm/s), it was observed that the discontinuities existing in the bilinear constitutive law resulted in instabilities. These were not observed for the 3^{rd} order polynomial or linear-polynomial laws. However, all formulations were shown to model appropriately mode I, mode II and mixed mode I and II quasi-static crack propagation problems, at lower loading rates.

The decohesion element was shown to accurately model a range of static delamination problems. This element can then be applied to a range of impact and crash problems, eventually involving in addition in-plane damage. Other applications include modelling compression after impact (CAI) and the propagation of any delaminations from the initial impact. However, while parameters such as maximum tractions, penalty stiffnesses and mesh refinement used for quasi-static analyses can

[3]The crack length in Figs. 2.15(c) and (d) corresponds to the mid-point of the cohesive zone, which has a length $\approx 1.1\mathrm{mm}$ for any of the curves presented.

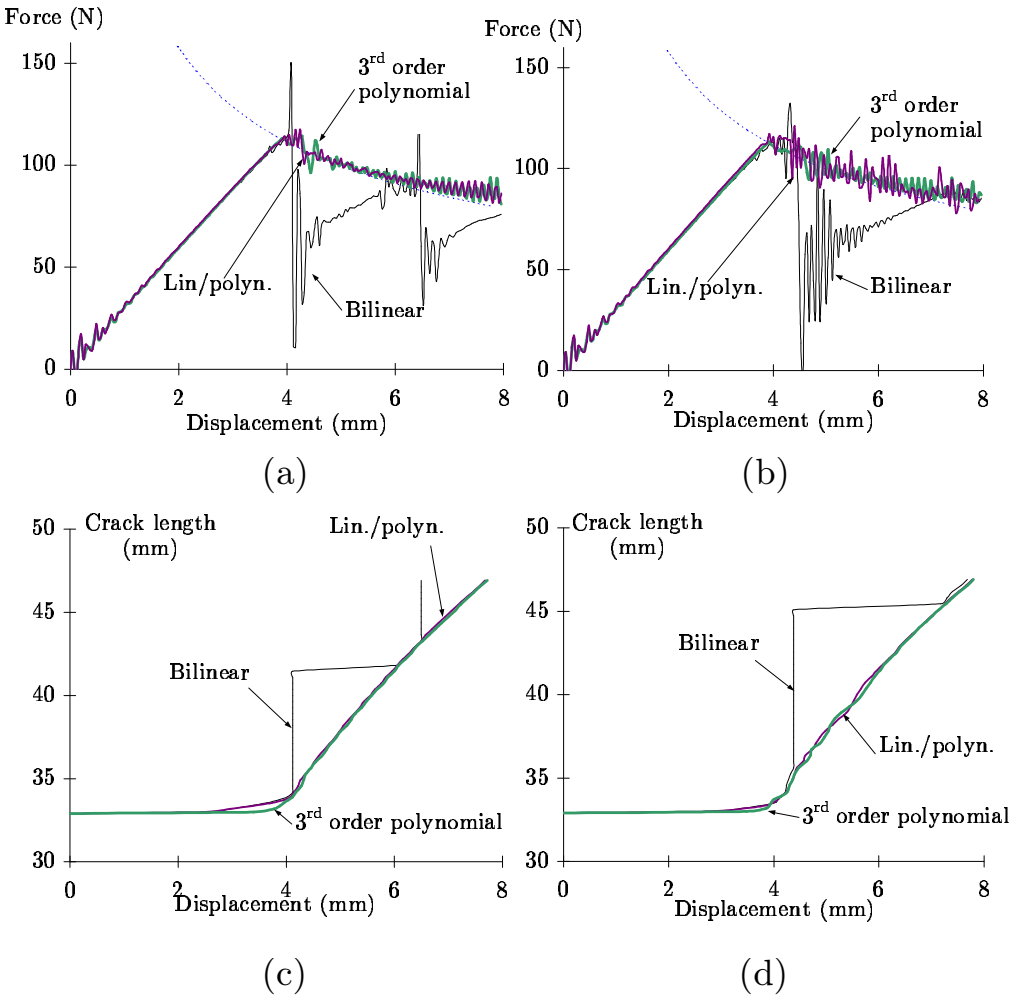

Figure 2.15: Comparison of the load vs. displacement curves obtained with different interface models, for (a) $N = 50\,\mathrm{MPa}$ and (b) $N = 80\,\mathrm{MPa}$; and corresponding crack-length vs. displacement for (c) $N = 50\,\mathrm{MPa}$ and (d) $N = 80\,\mathrm{MPa}$

be used for dynamic ones (more refined meshes might be required if the stress gradients are more accentuated), the dynamic fracture toughness may need to be determined for a more accurate simulation.

2.7 Publications

The work presented in this chapter resulted in the following publications[4]:

1. S. T. Pinho, L. Iannucci, P. Robinson. Crashworthiness of Composite Structures. Poster presented at GSEPS Research Student Research Symposium, Poster Competition, Imperial College London, 16^{th} July 2003 (won the 2^{nd} prize); *and* at Industrial Affiliates Annual Review Meeting, The Composites Centre, Imperial College London, 25^{th} September 2003

2. S. T. Pinho. MPhil to PhD Transfer Report: Formulation and implementation of a 3D decohesion element for delamination modelling in explicit FE codes. Department of Aeronautics, Imperial College London, 14^{th} (interview) and 17^{th} (power point presentation) October 2003

3. S. T. Pinho, L. Iannucci, P. Robinson. Modelling delamination in an explicit FE code using 3D decohesion elements. CompTest2004, Bristol, 21^{st} - 23^{rd} September 2004

4. S. T. Pinho, L. Iannucci, P. Robinson. Formulation and implementation of decohesion elements in an explicit finite element code. In press, Composites Part A, 2005

[4]Some of these publications include work from other chapters of this thesis and therefore feature again in the list of publications at the end of the corresponding chapters.

Chapter 3

Formulation of failure models and criteria

3.1 Acknowledgment

The work presented in this chapter was started at Imperial College London by the author and his supervisors. From the survey carried on failure criteria, it became apparent that the LaRC02 [4] failure criteria were among the best in the open literature. Some modifications and generalizations were proposed, and application examples carried [36–38]. This work was communicated to the proposers of the LaRC02 failure criteria (which in the meanwhile had become LaRC03 [39]) and a cooperation was started to develop, write and publish LaRC04 [40]. This cooperation resulted in many discussions, and considerable modifications to the models and criteria as a whole. In particular, the sub-section that deals with in-situ effects for tensile matrix failure was totally developed and written in close cooperation with Dr. Pedro Camanho and Dr. Carlos Dávila, and based on their previous published work [4, 39, 41]. In general, all of the work reported in this chapter has been influenced either by their published work, or by their direct involvement. As a result, Dr. Pedro Camanho and Dr. Carlos Dávila's contribution to the work presented in this chapter is acknowledged.

3.2 Introduction

The mechanisms that lead to failure in composite materials are not fully understood yet. This is especially true for compressive failure, both for the matrix and fibre-dominated failure modes. This has become particularly evident after the World Wide Failure Exercise (WWFE) [42].

In this chapter, physically-based failure models are discussed and proposed for each failure mode in laminated fibre-reinforced composites with unidirectional plies, at the ply level.

If composite materials are to be used in structural applications, then the understanding of how each failure mode takes place—i.e. having a physical model for each failure mode—becomes an important point of concern. These physical models should establish *when* failure takes place, and also describe the post-failure behaviour. For instance, a physical model for matrix compressive failure should predict that failure occurs when some stress state is achieved, as well as *what* orientation the fracture plane should have and how much energy the crack formation should dissipate.

The main failure modes of laminated fibre-reinforced composites are:

Delamination. Composite materials made of different plies stacked together tend to delaminate. The bending stiffness of delaminated panels can be significantly reduced, even when no defect is visible on the surface or the free edges. The physics of delamination is to a certain degree understood, and one of the best numerical tools to predict the propagation of delamination consists on the use of decohesion elements.

Matrix compressive failure. What is commonly referred to as matrix compressive failure is actually matrix shear failure. Indeed, failure occurs at an angle with the loading direction, which is evidence of the shear nature of the failure process.

Fibre compressive failure. This failure mode is largely affected by the resin shear behaviour and imperfections such as the initial fibre misalignment angle and voids. Typically, kink bands can be observed at a smaller scale, and are the result of fibre micro-buckling, matrix shear failure or fibre failure.

Matrix tensile failure. The fracture surface resulting from this failure mode is typically normal to the loading direction. Some fibre splitting at the fracture surface can usually be observed.

Fibre tensile failure. This failure mode is typically explosive. It releases large amounts of energy, and, in structures that cannot redistribute the load, it typically causes catastrophic failure.

Experimental results from the WWFE [42, 43] indicate that the (admittedly scarce) data on fibre tensile failure under bi- or multi-axial stress states does not seem to invalidate the maximum stress criterion. Thus, this chapter focuses on models for compressive failure, which is of great interest in crashworthiness and other areas, as well as matrix tensile failure.

Accurate physically-based criteria are developed and preferred to curve-fitting-based criteria. The main limitation associated with curve-fitting-based criteria is that their applicability is restricted to the load combinations used in the curve fitting from which they originate. However, it is impractical to test every material in enough load combinations to define these criteria for every combination of the six stress tensor components.

Matrix compressive failure is addressed with a model based on the Mohr-Coulomb criterion. Puck et al. [2, 44–46] were the first researchers to propose a matrix failure model based on the Mohr-Coulomb criterion. Further developments were later carried by Dávila et al. [4, 39] for the LaRC02/03 failure criteria. In this present work, an analysis of both Puck [2, 46] and LaRC02/03 [4, 39] matrix compressive failure criteria is performed. For the LaRC02/03 criteria, a correction is proposed for the consideration of friction stresses. This leads to more conservative predictions, and makes the resulting failure envelope coincide with a simpler criterion that can be related to the work from Puck and Schürmann [2, 46]. The analysis concludes with the proposal of the latter as a matrix failure criterion for a three dimensional (3D) stress state. Matrix tensile failure is addressed combining the action or fracture plane concept from Puck and Schürmann [2, 46] with experimental evidence from the WWFE. Also, a failure model for matrix in tension and shear is derived from Dvorak and Laws [47] fracture mechanics analyses of cracked plies, as a generaliza-

tion of LaRC03 [39].

For fibre failure in compression, it is assumed that kink-band formation results from matrix failure, due to small misalignments of the fibres in the composite. Also, it is suggested that shear nonlinearity should have a considerable effect on failure and 2D analyses of fibre kinking over-simplify the treatment of the problem. A formal treatment of fibre kinking is presented, that leads to a model for fibre kinking similar to the one proposed by Dávila et al. [4, 39]. The main differences are that the model presented here accounts for 3D effects, considers a generic nonlinear shear behaviour, and uses the matrix failure criteria from this work.

In this chapter, the index a refers to the fibre direction, the index b refers to the in-plane transverse direction and the index c refers to the through-the-thickness direction.

3.3 Literature review

The need for predicting failure in composites has led to the proposal of several failure criteria. These are usually stress-based and expressed as equations or sets of equations. There is no unique system of classification for failure criteria. The one presented here classifies the failure criteria based on the approach followed in their derivations: non physically-based (or not associated with the failure modes, or non-phenomenological) and physically-based (or associated with the failure modes, or phenomenological). This classification system has been used before by Echabi et al. [48] and París [49].

Non physically-based failure criteria. These are criteria in which a failure envelope is defined by using a mathematical expression, usually a polynomial, which predicts failure by interpolating between a few experimental points. No attempt is made to predict which failure mode is taking place, and the criterion itself is not the result of a physically-based failure model.

Physically-based failure criteria. These are criteria which result from models that, to a smaller or greater detail, aim at describing the physics of the failure process. Not only these criteria predict failure, as they give information on the

failure mode and sometimes provide further details characterizing the failure process.

3.3.1 Non physically-based failure criteria

Most non-phenomenological failure criteria are expressed in the form of polynomials, usually of the second order; for plane stress, they can be expressed as

$$f = F_{11}\sigma_a^2 + F_{22}\sigma_b^2 + F_{66}\tau_{ab}^2 + 2F_{12}\sigma_a\sigma_b + F_1\sigma_a + F_2\sigma_b + F_6\tau_{ab} \tag{3.1}$$

where the coefficients F_{ii} and F_j depend on the specific criterion and failure takes place for $f = 1$.

For the Tsai-Hill [50] criterion, where the coefficients depend on whether the state of stress is tensile or compressive, these are given by

$$\begin{aligned} F_{11} &= \frac{1}{X^2}, \qquad F_1 = 0, \qquad F_{12} = -\frac{1}{2X^2}, \\ F_{22} &= \frac{1}{Y^2}, \qquad F_2 = 0, \\ F_{66} &= \frac{1}{S_{ab}^2} \quad \text{and} \qquad F_6 = 0 \end{aligned} \tag{3.2}$$

with

$$\begin{aligned} \sigma_a &\geq 0 \Rightarrow X = X_t; \quad \sigma_a < 0 \Rightarrow X = X_c \\ \sigma_b &\geq 0 \Rightarrow Y = Y_t; \quad \sigma_b < 0 \Rightarrow Y = Y_c. \end{aligned} \tag{3.3}$$

In the previous equation, X_t, X_c, Y_t and Y_c are the tensile and compressive strengths, in the fibre and transverse directions respectively. In the Tsai-Wu [51] criterion, the coefficients are

$$\begin{aligned} F_{11} &= \frac{1}{X_t X_c}, \qquad F_1 = \frac{1}{X_t} - \frac{1}{X_c}, \\ F_{22} &= \frac{1}{Y_t Y_c}, \qquad F_2 = \frac{1}{Y_t} - \frac{1}{Y_c}, \\ F_{66} &= \frac{1}{S_{ab}^2}, \qquad F_6 = 0, \end{aligned} \tag{3.4}$$

and the coefficient F_{12} is given by

$$F_{12} = \frac{F_{12}^*}{\sqrt{X_t X_c Y_t Y_c}} \tag{3.5}$$

with $-1 < F_{12}^{*} < 1$ obtained by fitting experimental data. For the Hoffman [52] criterion, the coefficients are the same, apart from F_{12} which is given by

$$F_{12} = -\frac{1}{2X_t X_c}.$$

The non physically-based failure criteria presented are given as an overview only. More non physically-based failure criteria can be found in the reviews by Nahas [53] or by París [49].

3.3.2 Physically-based failure criteria

Physically-based failure criteria distinguish between failure modes. The failure envelopes corresponding to these criteria are therefore not always smooth, and the vertices correspond usually to a change in the failure mode. Hashin and Rotem [54] are usually credited to have established that the heterogenous nature of fibre reinforced composite materials means that failure is due to the failure of the different constituents (or their interfaces), and failure criteria should therefore predict failure of each constituent separately. Hence failure criteria should be composed of several expressions for the different failure modes. In fact, Puck's model, which also distinguishes between failure modes, is originally from 1969 [44, 45] (although published in German, in a journal that is "not known to the search engines" [2]), and therefore older than the Hashin-Rotem criterion from 1973 [54]. In any case, Hashin and Rotem's work in 1973 [54] and later Hashin's work in 1980 [55] have inspired considerable research in failure-mode oriented criteria.

The maximum strain and the maximum stress failure criteria are among the simplest physically-based failure criteria. In the maximum strain failure criterion, failure is predicted whenever the failure strain for uniaxial tests is attained, either in the axial or transverse directions, or in shear:

$$f = \max\left(\left|\frac{\varepsilon_a}{\varepsilon_a^o}\right|, \left|\frac{\varepsilon_b}{\varepsilon_b^o}\right|, \left|\frac{\varepsilon_{ab}}{\varepsilon_{ab}^o}\right|\right) \tag{3.6}$$

with

$$\begin{aligned} \varepsilon_a &\geq 0 \Rightarrow \varepsilon_a^o = \varepsilon_a^{ot}; \quad \varepsilon_a < 0 \Rightarrow \varepsilon_a^o = \varepsilon_a^{oc} \\ \varepsilon_b &\geq 0 \Rightarrow \varepsilon_b^o = \varepsilon_b^{ot}; \quad \varepsilon_b < 0 \Rightarrow \varepsilon_b^o = \varepsilon_b^{oc} \end{aligned} \tag{3.7}$$

where ε_a^{ot}, ε_a^{oc}, ε_b^{ot} and ε_b^{oc} are the tensile and compressive strains at failure, in the a and b directions respectively.

The maximum stress failure criterion is similar to the maximum strain, but replacing strains with stresses:

$$f = \max\left(\left|\frac{\sigma_a}{X}\right|, \left|\frac{\sigma_b}{Y}\right|, \left|\frac{\sigma_{ab}}{S_{ab}}\right|\right) \tag{3.8}$$

with

$$\begin{aligned} \sigma_a &\geq 0 \Rightarrow X = X_t; \quad \sigma_a < 0 \Rightarrow X = X_c \\ \sigma_b &\geq 0 \Rightarrow Y = Y_t; \quad \sigma_b < 0 \Rightarrow Y = Y_c. \end{aligned} \tag{3.9}$$

In the already mentioned Hashin and Rotem's work [54], fibre failure is predicted by

$$f_f = \begin{cases} \dfrac{\sigma_a}{X_t} \Leftarrow \sigma_a \geq 0 \\ \dfrac{-\sigma_a}{X_c} \Leftarrow \sigma_a < 0 \end{cases} \tag{3.10}$$

and matrix failure by

$$f_{mat} = \begin{cases} \left(\dfrac{\sigma_b}{Y_t}\right)^2 + \left(\dfrac{\sigma_{ab}}{S_{ab}}\right)^2 \Leftarrow \sigma_b \geq 0 \\ \left(\dfrac{\sigma_b}{Y_c}\right)^2 + \left(\dfrac{\sigma_{ab}}{S_{ab}}\right)^2 \Leftarrow \sigma_b < 0. \end{cases} \tag{3.11}$$

Hashin [55] later modified the expressions for fibre and matrix failure, the result being the Hashin criteria. Fibre failure is predicted by

$$f_f = \begin{cases} \left(\dfrac{\sigma_a}{X_t}\right)^2 + \left(\dfrac{\sigma_{ab}}{S_{ab}}\right)^2 \Leftarrow \sigma_a \geq 0 \\ \dfrac{-\sigma_a}{X_c} \Leftarrow \sigma_a < 0 \end{cases} \tag{3.12}$$

and matrix failure by

$$f_{mat} = \begin{cases} \left(\dfrac{\sigma_b}{Y_t}\right)^2 + \left(\dfrac{\sigma_{ab}}{S_{ab}}\right)^2 \Leftarrow \sigma_b \geq 0 \\ \left(\dfrac{\sigma_b}{2S_T}\right)^2 + \left[\left(\dfrac{Y_c}{2S_T}\right) - 1\right]\dfrac{\sigma_b}{Y_c} + \left(\dfrac{\sigma_{ab}}{S_{ab}}\right)^2 \Leftarrow \sigma_b < 0 \end{cases} \tag{3.13}$$

where S_T is the transverse shear strength.

Since the Hashin-Rotem criteria have been published, several other failure-mode oriented criteria have been proposed. In particular, Yamada and Sun [56] proposed

a criterion for the fibre breaking mode which included in-situ effects on the in-plane shear strength. This criterion was then used to predict the same failure mode in the Chang and Chang criteria [57–59], which has since been implemented in Ls-Dyna [1]. Christensen [60] proposed criteria for fibre and matrix dominated failure modes, which included the effect of hydrostatic pressure. Puck's model and criteria [44, 45, 61], were made available in English only recently, as a result of a project in Germany for the development of failure criteria for composites [62, 63]. Hart-Smith [64, 65] presented and developed criteria for fibrous composites based on a maximum shear stress criterion with a number of associated cutoff rules.

More recently, the WWFE [66] was conducted to assess the real predicting capability of the currently available failure criteria. Leading researchers in failure of composites were invited to participate in a round-robin in which they presented their approaches and predictions.

In the exercise, Hart-Smith [67–69] presented the original version of the maximum strain criterion, as well as a truncated form and a generalized form of the criterion. Gotsis et al. [70, 71] used the maximum stress criterion, superposed with a modified distortion energy (quadratic polynomial) criterion. McCartney [72, 73] applied the principles of mechanics at the microstructural level to predict damage formation. Rotem [74, 75] used the Hashin-Rotem criterion originally published in 1973 [54], but with the matrix failure criterion modified in order to account for axial stresses. Surprisingly, Sun and Tao [76, 77] used the Hashin-Rotem criterion [54], even though Sun had proposed previously [78] a criterion for matrix cracking that is acknowledged to represent better the matrix failure mode [4]. However, their predictions were overall particularly good. Liu and Tsai [79] used the Tsai-Wu [51] failure criterion. Wolfe and Butalia [80, 81] used a strain-energy based failure criterion, containing a sum on exponents of the longitudinal, transverse and shear strain energies. Edge [82, 83] used a phenomenological approach based on the stress interaction within each failure mode, with some similarities to the maximum stress, the Hashin-Rotem [54] and Hashin [55] criteria. Zinoviev [84, 85] used the simple maximum stress criterion, together with an also simple post failure-onset model, obtaining particularly good results. Puck and Schürmann [2, 46] were perhaps the

authors who achieved better agreement between their predictions and the experiments. Their criterion is phenomenological, as different failure modes are considered and is characterized by a sound physical basis. Arguably, their model for matrix compressive failure possesses the most sound physical basis of the theories proposed in the exercise. In Part C of the exercise, Huang [86, 87] and Mayes and Hansen [88, 89] used two different micromechanics-based approaches. Bogetti et al. employed the maximum strain criteria in a progressive failure analysis, obtaining particularly good results, as well as Cuntze and Freund [90, 91] (with a model similar to Puck's [2, 46]).

Several lessons can be learned from the WWFE. Firstly, most criteria were unable to capture some of the trends in the failure envelopes of the experimental results. Secondly, on what concerns phenomenological failure criteria, most expressions proposed to predict each failure mode are still to some extent empirical. It is somewhat difficult to choose between the criteria due to the lack of experimental data needed to validate them against each other. Despite several efforts to develop sound phenomenological criteria, non-phenomenological criteria like Tsai-Wu [51] are often better prediction tools than some phenomenological criteria [79]. Although test results are not provided in the WWFE for several stress combinations that remain open for discussion, significant progress was made. From the limited predictive capabilities of the most accurate analyses available, it is clear that further developments in failure model theories and criteria are required before any analysis approach can be used with confidence to predict the strength of a typical aerospace composite component.

3.4 Fibre tensile failure

For fibre tensile failure, it is somewhat difficult to argue whether stresses other than σ_a contribute to promote failure and have any influence on the strength. For instance, Soden et al. [43] obtained experimental data to define the (σ_a, τ_{ab}) failure envelope of carbon fibre reinforced composite, and the (σ_a, σ_b) failure envelope of glass fibre reinforced composite. From their results, it does not seem possible to

draw sound conclusions on how the different stress components interact to promote failure. Therefore the maximum stress failure criterion is used:

$$f_{ft} = \frac{\sigma_a}{X_t} = 1. \tag{3.14}$$

3.5 Matrix compressive failure

3.5.1 Mohr-Coulomb based criteria

The orientation of the fracture surface of specimens failing by matrix compression suggests that the Mohr-Coulomb criterion is applicable to matrix compressive failure [2, 44–46]. Matrix compression specimens fail by shear. For a pure compression loading, this fact suggests that the angle of the fracture surface with the through-the-thickness direction should be $\phi_o = 45°$, i.e. fracture should occur in the plane of the maximum shear stresses. However, it is experimentally seen that the angle is generally $\phi_o = 53 \pm 2°$ for most technical composite materials [2, 46], Fig. 3.1(a). This can be explained through the existence of a compressive stress acting on the potential fracture surfaces, and an associated friction stress.

The designation 'friction stress' is here used, as it was by previous authors [2, 46], even though there is no interface before fracture. At the micro-mechanical level, the effective macro-mechanical friction stress can be explained, at least partially, as resulting from the 'true' friction stress acting in the micro-cracks in the matrix before failure.

For a general loading situation, Fig. 3.1(b), the angle of the fracture plane with the through-the-thickness direction, denoted as ϕ, might assume a different value than the one for pure compression (ϕ_o). The particular orientation of the fracture plane depends on the particular combination of shear (τ_T and τ_L) and normal (σ_n) traction components for each particular value of ϕ, Fig. 3.1(c).

In a 3D formulation, the traction components are obtained from the components

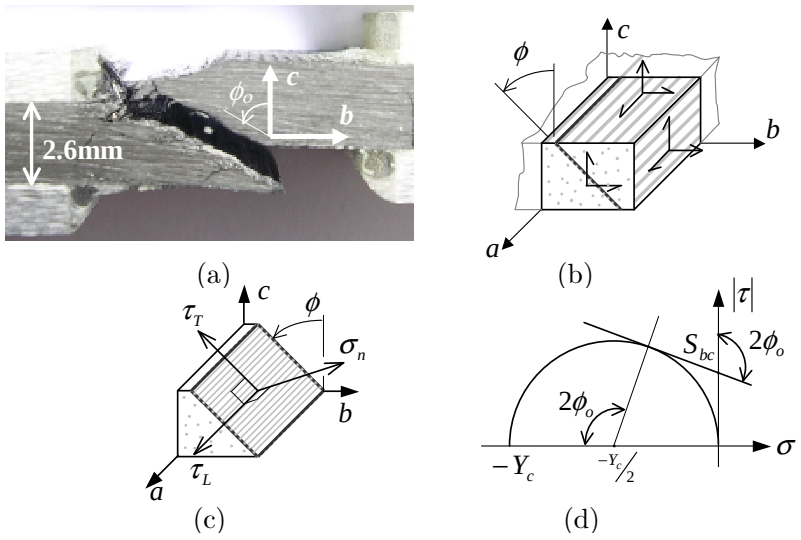

Figure 3.1: (a) Pure transverse compressive failure, for a CFRP specimen; (b) fracture plane for a 3D stress state; (c) traction components in the fracture plane; (d) geometrical representation of the Mohr-Coulomb criterion

of the stress tensor and the fracture plane angle ϕ as

$$\begin{aligned}\sigma_n &= \frac{\sigma_b+\sigma_c}{2} + \frac{\sigma_b-\sigma_c}{2}\cos(2\phi) + \tau_{bc}\sin(2\phi)\\ \tau_T &= -\frac{\sigma_b-\sigma_c}{2}\sin(2\phi) + \tau_{bc}\cos(2\phi)\\ \tau_L &= \tau_{ab}\cos(\phi) + \tau_{ca}\sin(\phi)\,.\end{aligned} \tag{3.15}$$

The Mohr-Coulomb failure criterion is expressed in terms of the components of the traction vector in the fracture plane, and can be written in several forms. Considering first the case where $\tau_L = 0$, the Mohr-Coulomb criterion can be expressed as

$$|\tau_T| + \mu_T \sigma_n = S_T \qquad (\sigma_n < 0) \tag{3.16}$$

where μ_T is a friction coefficient and S_T is the fracture plane fracture resistance against its fracture by transverse shear[1]. For simplicity, S_T is not considered to depend on ϕ, and will be designated as transverse shear strength. For a more detailed explanation on the difference between fracture plane fracture resistance and strength, see Ref. [2]. The geometrical representation of this criterion in a (σ,$|\tau|$)

[1]The fracture plane resistance of a potential fracture plane parallel to the fibres is the resistance of this plane against its fracture due to a single stressing acting in this plane [46].

space is a line with negative slope ($-\mu_T$), shown in Fig. 3.1(d). In this figure, the Mohr-Coulomb criterion's line is tangential to the Mohr circle corresponding to the case of failure by pure compression. The slope of the Mohr-Coulomb criterion's line can be related to the angle of the fracture plane in pure compression, ϕ_o, through

$$\tan(2\phi_o) = -\frac{1}{\mu_T}. \tag{3.17}$$

Furthermore, writing Eq. 3.16 for a pure compression case establishes the relation between S_T, Y_c and ϕ_o [61]:

$$S_T = \frac{Y_c}{2\tan(\phi_o)}. \tag{3.18}$$

The angle ϕ_o can be easily determined from simple compression tests, Fig. 3.1(a), and allows the determination of μ_T and S_T by using Eqs. 3.17 and 3.18.

The Mohr-Coulomb criterion (Eq. 3.16) can be expressed in several forms, namely considering that friction affects (increases) the strength, or that it affects (decreases) the applied stress. Probably motivated by those two different forms of expressing the same criterion for $\tau_L = 0$, Puck and Schürmann [2, 46] initially proposed for the general case ($\tau_L \neq 0$)

$$f_{mc} = \left(\frac{\tau_T}{S_T - \mu_T\sigma_n}\right)^2 + \left(\frac{\tau_L}{S_L - \mu_L\sigma_n}\right)^2 = 1, \tag{3.19}$$

whereas Dávila et al. proposed first for the LaRC02 [4] failure criteria and subsequently for the LaRC03 [39] failure criteria

$$f_{mc} = \left(\frac{\langle|\tau_T| + \mu_T\sigma_n\rangle}{S_T}\right)^2 + \left(\frac{\langle|\tau_L| + \mu_L\sigma_n\rangle}{S_L}\right)^2 = 1 \tag{3.20}$$

where S_L is the longitudinal shear strength (for simplicity, S_L is considered not to depend on ϕ) and the operator $\langle\cdot\rangle$ is the Mc-Cauley bracket defined by $\langle x\rangle = \max\{0, x\}$, $x \in \mathbb{R}$. Clearly, Puck and Schürmann (Eq. 3.19) consider that the compression stress (σ_n) increases the effective strength, while Dávila et al. (Eq. 3.20) consider that the compression stress reduces the effective shear stress. Puck and Schürmann [2, 46] finally choose to use the following equation, arguing that it fits the experimental data better:

$$f_{mc} = \frac{(\tau_T)^2}{S_T^2 - 2\mu_T S_T\sigma_n} + \frac{(\tau_L)^2}{S_L^2 - 2\mu_L S_L\sigma_n} = 1. \tag{3.21}$$

Table 3.1: Mechanical properties for an E-glass/DY063 epoxy used in the WWFE [66], given by Soden et al. [43, 92]

G_{ab} (GPa)	S_{ab} (MPa)	X_c (MPa)	Y_c (MPa)	ϕ_o (^{o})
5.83	73	800	145	53

For the friction coefficient μ_L in Eqs. 3.19, 3.20 and 3.21, Puck and Schürmann [2] proposed to use the following equation

$$\frac{\mu_L}{S_L} = \frac{\mu_T}{S_T} \tag{3.22}$$

in the absence of biaxial experimental data. This suggestion has later been considered by Dávila et al. for the LaRC02/03 criteria [4, 39].

3.5.2 Comparison and improvements

The comparison of the criteria expressed in Eqs. 3.19, 3.20 and 3.21 is shown in Fig. 3.2 for a material with the properties presented in Table 3.1. In Fig. 3.2, the fracture angle for each point in each curve was determined by trying several tentative angles, as explained later in this subsection.

While the initial and final Puck criteria (Eqs. 3.19 and 3.21) yield similar results, LaRC02/03 criterion (Eq. 3.20) is less conservative. This is related to the fact that the effect of friction is over-estimated in Eq. 3.20. Indeed, affecting the shear traction components by a friction term as in Eq. 3.20 over-estimates the friction forces whenever both τ_T and τ_L are acting simultaneously. As Fig. 3.3(a) represents, supposing a very simple case with isotropic friction ($\mu_T = \mu_L$), the friction stresses are over-estimated by a factor of $\sqrt{2}$ when using Eq. 3.20.

It is interesting to notice the effect that an orthotropic friction model has on LaRC02/03 criterion (Eq. 3.20). A reasonable model for orthotropic friction is

$$\left\{ \begin{array}{c} \tau_T^{fric.} \\ \tau_L^{fric.} \end{array} \right\} = \sigma_n \left[\begin{array}{cc} \mu_T & 0 \\ 0 & \mu_L \end{array} \right] \left\{ \begin{array}{c} \frac{\tau_T}{\tau} \\ \frac{\tau_L}{\tau} \end{array} \right\} \quad \therefore \quad \left\{ \begin{array}{l} \tau_T^{fric.} = \sigma_n \mu_T \cos(\theta) \\ \tau_L^{fric.} = \sigma_n \mu_L \sin(\theta) \end{array} \right. \tag{3.23}$$

where θ is the angle formed by the shear component of the traction vector, τ, and the transverse direction in the fracture plane, i.e., $\theta = \arctan(\tau_L/\tau_T)$. Curiously,

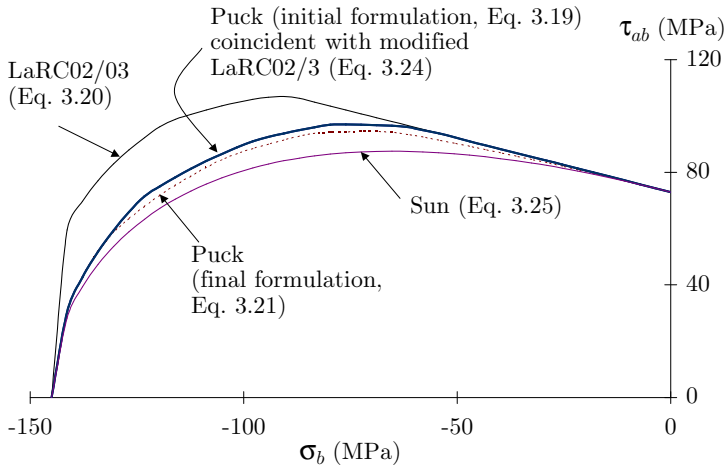

Figure 3.2: Failure envelopes for transverse compression and in-plane shear

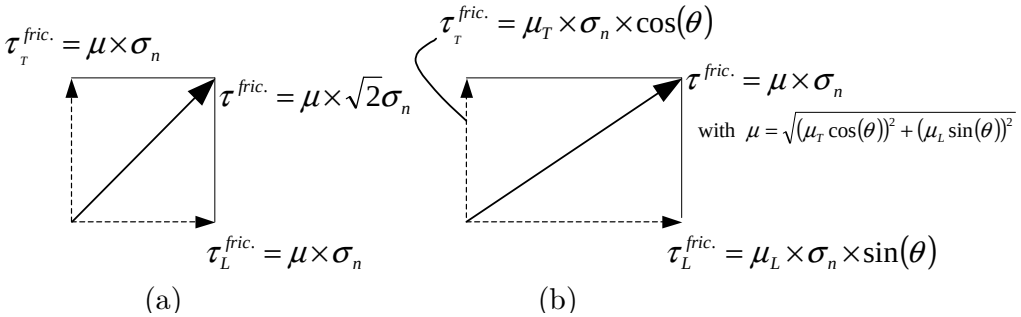

Figure 3.3: (a) Overestimation of the friction stress; (b) model that does not overestimate the friction stresses

modifying LaRC02/03 criterion (Eq. 3.20) to account for this more representative friction stress, i.e., using

$$f_{mc} = \left(\frac{\langle |\tau_T| + \mu_T \sigma_n \cos(\theta) \rangle}{S_T} \right)^2 + \left(\frac{\langle |\tau_L| + \mu_L \sigma_n \sin(\theta) \rangle}{S_L} \right)^2 = 1 \tag{3.24}$$

as a failure criterion yields an envelope that is coincident with Puck's initial criterion (Eq. 3.19), see Fig. 3.2.

Also shown in Fig. 3.2 is the much simpler Sun et al. [78] criterion,

$$f_{mc} = \left(\frac{\sigma_b}{Y_c} \right)^2 + \left(\frac{\tau_{ab}}{S_L - \mu_L \sigma_b} \right)^2 = 1 \tag{3.25}$$

which exhibits the correct trend.

The use of one of Eqs. 3.19, 3.20, 3.21, and 3.24 for the failure criterion implies the use of the set of Eqs. 3.15 for the transformation of stresses. In turn, this means that the fracture angle has to be known. Puck and Schürmann [2] have performed an analytical deduction for Eq. 3.21 in a plane stress state, but it is much more complex to do so for Eqs. 3.19, 3.20 and 3.24 for 3D stress states. However, Dávila et al. [4] have shown that it is possible to draw the envelope with reasonable accuracy by using a very small number of trial angles, as shown in Fig. 3.4, drawn using the data from Table 3.1 and Puck's initial criterion (Eq. 3.19). The latter approach is followed in this work.

3.5.3 Selection of a matrix compressive failure criterion

The criterion expressed by Eq. 3.21 is a modified version of the one expressed by Eq. 3.19 and the failure envelopes for the criteria are almost identical, as shown in Fig. 3.2. An advantage of the former over the latter consists on the possibility of calculating the fracture angle ϕ for each load situation—in plane stress. For a 3D situation, the advantage does not exist, but the modification introduced means Eq. 3.21 does not correctly represent the Mohr-Coulomb criterion. Therefore, for 3D applications, Eq. 3.19 is preferred over Eq. 3.21.

As discussed, Eq. 3.20 over-estimates the friction stresses. Correcting this results in Eq. 3.24, which correctly applies the Mohr-Coulomb criterion, assuming that the

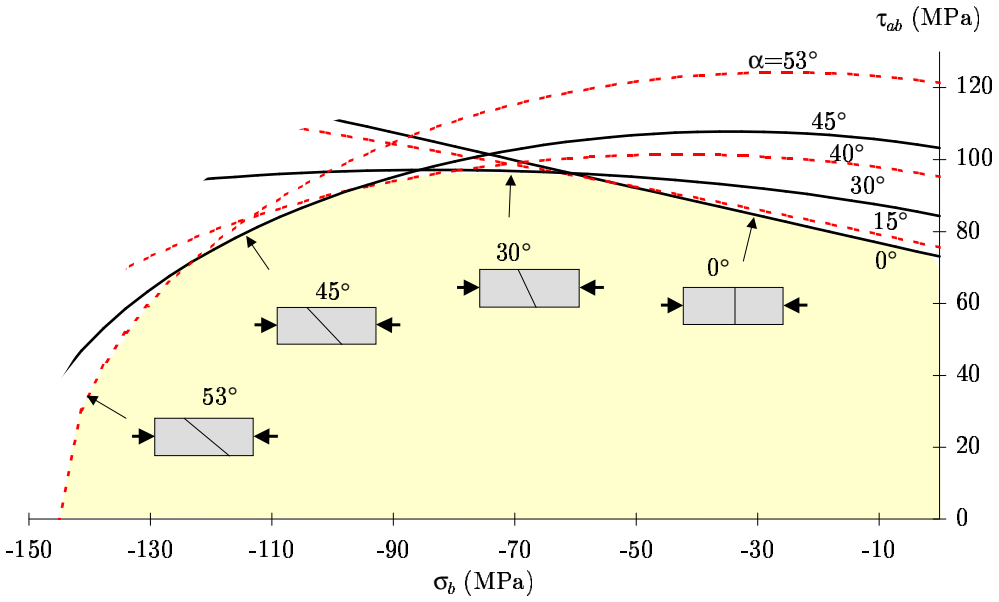

Figure 3.4: Failure envelope for Puck's initial matrix failure criterion (Eq. 3.19), and several values for the angle of the fracture plane, ϕ, based on Ref. [4]

compression reduces the shear stresses. Assuming instead that compression increases the strength results in Eq. 3.19. Both Eqs. 3.19 and 3.24 are physically sound.

Finally, since Eqs. 3.19 and 3.24 yield similar results, but the former is simpler, Eq. 3.19 is selected as the matrix compressive failure criterion (i.e. for $\sigma_n < 0$) in this work. This equation has also been chosen as the LaRC04 matrix compression failure criterion [40].

3.6 Matrix tensile failure

3.6.1 Without in-situ effects

It can be concluded from the WWFE's experimental results [43], that a quadratic interaction between the transverse stress σ_b and the in-plane shear stress τ_{ab} describes appropriately the (σ_b, τ_{ab}) failure envelope, for the matrix tensile failure mode. Dávila et al. [4] used this interaction criterion for the LaRC02 failure criteria. However, for the (σ_b, τ_{ab}) failure envelope, the fracture plane is always parallel to

the (a, c) plane.

For a generic stress state, the matrix tensile fracture plane does not coincide necessarily with the (a, c) plane. Therefore, it seems reasonable to recast the traction components expressed in the potential fracture planes—as expressed in Eq. 3.15—and apply a quadratic interaction as follows:

$$f_{mt} = \left(\frac{\sigma_n}{Y_t}\right)^2 + \left(\frac{\tau_T}{S_T}\right)^2 + \left(\frac{\tau_L}{S_L}\right)^2 = 1. \tag{3.26}$$

The criterion applies for $\sigma_n \geq 0$, and Y_t is the in-plane transverse tensile strength.

3.6.2 With in-situ effects

3.6.2.1 In-situ effect

The in-situ effect, originally detected in Parvizi's tensile tests of cross-ply glass fibre reinforced plastics [93], is characterized by higher transverse tensile and shear strengths of a ply when it is constrained by plies with different fibre orientations in a laminate, when compared to the strength of the same ply in a unidirectional laminate. The in-situ strength also depends on the number of plies clustered together, and on the fibre orientation of the constraining plies.

The orientation of the constraining plies and the number of plies clustered together also affect the crack density and the stiffness reduction of the cracked ply. Wang's [94] tests of $(0/90_n/0)$ $(n = 1, 2, 3, 4)$ carbon/epoxy laminates have shown higher crack densities for thinner 90° layers. The reduction of the elastic properties of a cracked ply is normally predicted using elastic analyses of cracked plies [95, 96] or Continuum Damage Models [97–100].

The in-situ effect is illustrated in Fig. 3.5, where the relation between the in-situ transverse tensile strength and the total thickness of the 90° plies clustered together is represented.

Accurate in-situ strengths are necessary for any stress-based failure criterion for matrix cracking in constrained plies. Both experimental [57, 94, 101] and analytical methods [47, 96, 102] have been proposed to determine the in-situ strengths. In the following, the in-situ strengths are calculated using fracture mechanics solutions for the propagation of cracks in a constrained ply.

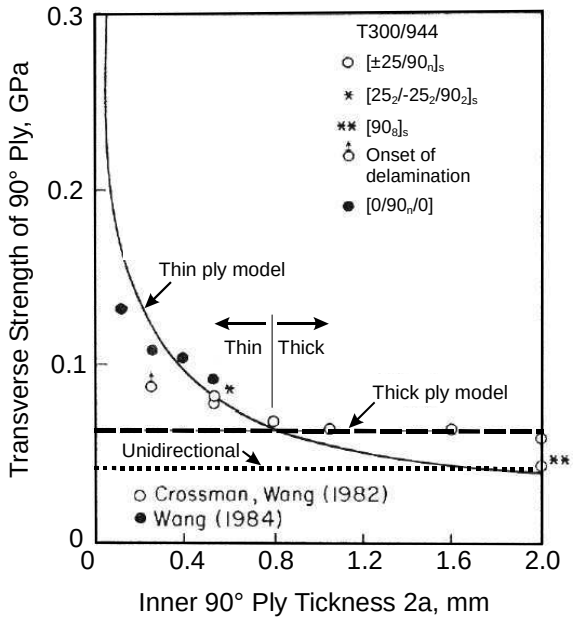

Figure 3.5: Transverse tensile strength as a function of number of plies clustered together, with models from Dvorak [47] based on experimental data from Wang [94]; figure from Ref. [40]

3.6.2.2 Fracture mechanics analysis of a cracked ply

The failure criterion for predicting matrix cracking in a ply subjected to in-plane shear and transverse tension proposed here is based on the fracture mechanics analysis of a slit crack in a ply, as proposed by Dvorak and Laws [47]. The slit crack represents a manufacturing defect that is idealized as lying on the (a, c) plane, as represented in Fig. 3.6 for a thick embedded ply. It has a length $2a_o$ across the thickness of a ply, t. Physically, this crack represents a distribution of matrix-fibre debonds that may be present in a ply as a consequence of manufacturing defects or from residual thermal stresses resulting from the different coefficients of thermal expansion of the fibres and of the matrix. Therefore, the slit crack is an 'effective crack,' representing the macroscopic effect of matrix-fibre debonds that occur at the micromechanical level [94].

The transverse tensile stress σ_b is associated with mode I loading, whereas the in-plane and transverse shear stresses τ_{ab} and τ_{bc} respectively are associated with mode II loading. The crack represented in Fig. 3.6 can grow in the a (longitudinal, L) direction, in the c (transverse, T) direction, or in both directions.

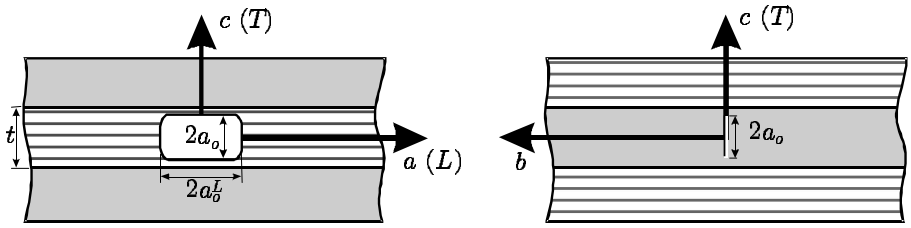

Figure 3.6: Slit crack geometry after Dvorak [47], from Ref. [40]

The components of the energy release rate for the crack geometry represented in Fig. 3.6 were determined by Dvorak and Laws [47] for a linear orthotropic material, and an extension of their analysis for nonlinear shear behaviour is presented in Appendix C. For mixed-mode loading, the energy release rate for crack growth in the T and L directions, G^T and G^L, respectively, are given by

$$\begin{aligned} G^T &= \tfrac{\pi a_o}{2}\left[\eta_I^2 \Lambda_b^o \sigma_b^2 + \eta_{II}^2 \Lambda_{bc}^o \tau_{bc}^2 + \eta_{III}^2 \chi\left(\gamma_{ab}\right)\right] \\ G^L &= \tfrac{\pi a_o}{4}\left[\xi_I^2 \Lambda_b^o \sigma_b^2 + \xi_{II}^2 \Lambda_{bc}^o \tau_{bc}^2 + \xi_{III}^2 \chi\left(\gamma_{ab}\right)\right] \end{aligned} \tag{3.27}$$

where Λ_b^o, Λ_{bc}^o and $\chi\left(\gamma_{ab}\right)$ are given in Appendix C. It can be observed that the energy release rate G^L for longitudinal propagation is a function of the transverse slit size and that it is not a function of the slit length in the longitudinal direction. The parameters η_i, $i = I, II, III$ in Eq. 3.27 are stress intensity reduction coefficients for propagation in the transverse direction, and the parameters ξ_i, $i = I, II, III$ are reduction coefficients for propagation in the longitudinal direction. These coefficients account for the constraining effects of the adjoining layers on crack propagation: the coefficients are nearly equal to 1.0 when $2a_o \ll t$, and are less than 1.0 when $a_o \approx t$. Experimental results [101] have shown an increase in the in-situ transverse tensile strength of $[\pm\theta/90_n]_s, \theta = 0°, 30°, 60°$ laminates for increasing stiffness of adjoining sublaminates $\pm\theta$. This implies that the value of the parameter η_i decreases with increasing stiffness of adjoining sublaminates. Considering that a transverse crack can promote delamination between the plies, Dvorak and Laws [47] suggested that the effective value of η_i can be larger than obtained from the analysis of cracks terminating at the interface, and suggested the use of $\eta_i = \xi_i = 1$.

The mode II and III components of the energy release rate are combined in a shear mode, G_{shear}, as $G_{shear} = G_{II} + G_{III}$. Such an approach was initially proposed

by Li and Sen [103] and Li [104], and used in the simulation of delamination using the Virtual Crack Closure Technique (VCCT) and decohesion finite elements [10]. In fact, no conclusive evidence is available showing that G_{IIc} and G_{IIIc} are different and there is no standard for measuring G_{IIIc} and there is no mixed-mode test method for mixed mode II and mode III loading. In the following, the notation G_{II} and G_{IIc} will be used for simplicity, when referring to G_{shear} and G_{Sc}.

The components of the energy release rate for a thick embedded ply are then obtained for the T-direction using Eq. 3.27 with $\eta_i = 1$:

$$G_I^T = \frac{\pi a_o}{2} \Lambda_b^o \sigma_b^2 \tag{3.28}$$

$$G_{II}^T = \frac{\pi a_o}{2} \left[\Lambda_{bc}^o \tau_{bc}^2 + \chi\left(\gamma_{ab}\right) \right]. \tag{3.29}$$

The corresponding components of the fracture toughness are given as

$$G_{Ic}^T = \frac{\pi a_o}{2} \Lambda_b^o \left(Y_{is}^t\right)^2 \tag{3.30}$$

$$G_{IIc}^T = \frac{\pi a_o}{2} \chi\left(\gamma_{ab\backslash is}^u\right) \tag{3.31}$$

where Y_{is}^t is the in-situ transverse tensile strength, and $\gamma_{ab\backslash is}^u$ is the in-situ in-plane shear ultimate strain.

For propagation in the longitudinal direction, the mode I and mode II components of the energy release rate are

$$G_I^L = \frac{\pi a_o}{4} \Lambda_b^o \sigma_b^2 \tag{3.32}$$

$$G_{II}^L = \frac{\pi a_o}{4} \left[\Lambda_{bc}^o \tau_{bc}^2 + \chi\left(\gamma_{ab}\right) \right] \tag{3.33}$$

and the components of the fracture toughness are

$$G_{Ic}^L = \frac{\pi a_o}{4} \Lambda_b^o \left(Y_{is}^t\right)^2 \tag{3.34}$$

$$G_{IIc}^L = \frac{\pi a_o}{4} \chi\left(\gamma_{ab\backslash is}^u\right). \tag{3.35}$$

Having obtained expressions for the components of the energy release rate and fracture toughness, a failure criterion can be applied to predict the propagation of the slit crack represented in Fig. 3.6. Under the presence of in-plane and transverse shear, as well as transverse tension, the critical energy release rate G_c depends

on the combined effect of all microscopic energy absorbing mechanisms such as the creation of new fracture surfaces. Relying on microscopic examinations of the fracture surface, Hahn [105] observed that the fracture surface topography strongly depends on the type of loading. With increasing proportion of the stress intensity factor K_{II}, more hackles are observed in the matrix, thereby indicating more energy absorption associated with crack extension. Hahn proposed a mixed-mode criterion written as a first-order polynomial in the stress intensity factors K_I and K_{II}. Written in terms of the mode I and mode II energy release rates, the Hahn criterion is

$$(1-g)\sqrt{\frac{G_I^i}{G_{Ic}^i}}+g\frac{G_I^i}{G_{Ic}^i}+\frac{G_{II}^i}{G_{IIc}^i}=1, \qquad i=T,L \tag{3.36}$$

where the material constant g is defined from Eqs. 3.30 and 3.31 or 3.34 and 3.35 as $g=G_{Ic}/G_{IIc}$ which leads to the following expression for g:

$$g=\frac{\Lambda_b^o\left(Y_{is}^t\right)^2}{\chi\left(\gamma_{ab\backslash is}^u\right)}. \tag{3.37}$$

In the following sub-sections, it will be shown that in situations where the slit crack propagates first in the transverse direction (like for UD and thick embedded plies), the in-situ strengths and thus also g can be obtained as a function of known UD strengths. However, for situations where microcracks propagate first in the longitudinal direction (like for thin embedded plies and outer plies), the in-situ strengths and g have to be obtained as a function of G_{Ic}^L and G_{IIc}^L, in which case the interlaminar fracture toughness values are recommended to be used as an approximation.

A failure index for matrix tension can be expressed in terms of the ply stresses and in-situ strengths by substituting either Eqs. 3.28-3.31 or 3.32-3.35 into the criterion in Eq. 3.36 to get

$$f_{mt}=(1-g)\frac{\sigma_b}{Y_{is}^t}+g\left(\frac{\sigma_b}{Y_{is}^t}\right)^2+\frac{\Lambda_{bc}^o\tau_{bc}^2+\chi\left(\gamma_{ab}\right)}{\chi\left(\gamma_{ab\backslash is}^u\right)}=1. \tag{3.38}$$

The criterion presented in Eq. 3.38, with linear and quadratic terms in σ_b, a quadratic term in τ_{bc} and a term on the in-plane shear internal energy, $\chi\left(\gamma_{ab}\right)$, is similar to the criteria proposed by Hahn [105] and Liu [79] (for transverse tension and in-plane shear). It can be observed that using $g=1$ in Eq. 3.36 results in the

linear version of the criterion proposed by Wu and Reuter [106] for the propagation of delamination in laminated composites

$$\frac{G_I}{G_{Ic}} + \frac{G_{II}}{G_{IIc}} = 1. \tag{3.39}$$

Furthermore, using $g = 1$, assuming linear in-plane shear, and neglecting τ_{bc}, Eq. 3.38 reverts to the well-known Hashin-Rotem criterion [54] for transverse matrix cracking under both in-plane shear and transverse tension, where the ply strengths are replaced by the in-situ strengths

$$f_{mt} = \left(\frac{\sigma_b}{Y_{is}^t}\right)^2 + \left(\frac{\tau_{ab}}{S_{is}^L}\right)^2 = 1. \tag{3.40}$$

Finally, the nonlinear term in Eq. 3.38 is also found to be similar to the strain-energy based criterion proposed by Sandhu [107], later used by Chang and Scott [108].

3.6.2.3 Application to unidirectional laminates

The application of the fracture mechanics analysis of a cracked ply to unidirectional laminates yields expressions relating toughness values to crack dimensions which can subsequently be used to relate the strength of thick embedded plies to that of a unidirectional laminate.

Dvorak and Laws [47] regarded the fracture of a unidirectional specimen as the fracture of an unconstrained thick ply, with the critical initial slit crack located at the surface of the laminate. For tensile loading, the crack can be located at the edge of the laminate, which increases the energy release rate when compared with a central crack. In the case of shear loading, there is no free edge effect, so the crack is a central crack, as shown in Fig. 3.7. The defect size is $2a_o$ and is considered to be much smaller than the ply thickness, $2a_o \ll t$.

For unidirectional laminates, the crack will grow unstably in the transverse direction [47], and Eqs. 3.30, 3.31, 3.34 and 3.35 apply with a geometric factor which is obtained from the classic solution of the free edge crack [39, 109], resulting in

$$G_{Ic}^T = 1.12^2 \pi a_o \Lambda_b^o \left(Y^t\right)^2 \tag{3.41}$$

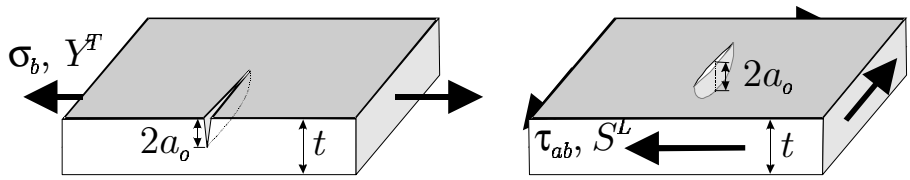

Figure 3.7: Unidirectional specimen with initial crack after Dvorak [47], figure from Ref. [40]

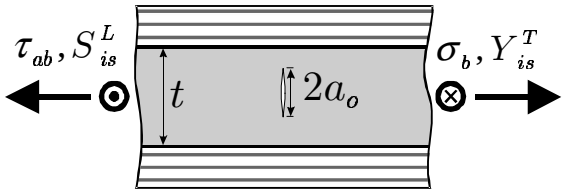

Figure 3.8: Geometry of slit crack in a thick embedded ply subjected to tension and shear loads, from Ref. [40]

$$G_{IIc}^{T} = \pi a_o \chi\left(\gamma_{ab}^{u}\right) \tag{3.42}$$

where Y_t is the transverse tensile strength and γ_{ab}^{u} is the in-plane shear strain at failure, for a unidirectional laminate.

The toughness ratio g can also be calculated in terms of the unidirectional properties by using Eqs. 3.41 and 3.42, resulting in

$$g = \frac{G_{Ic}}{G_{IIc}} = 1.12^2 \frac{\Lambda_b^o \left(Y_t\right)^2}{\chi\left(\gamma_{ab}^{u}\right)}. \tag{3.43}$$

Eq. 3.43 is valid for all situations where the slit crack propagates first in the transverse direction.

3.6.2.4 In-situ strength of thick embedded plies

A thick ply is defined as one in which the length of the slit crack is much smaller than the ply thickness, $2a_o \ll t$, as illustrated in Fig. 3.8. The minimum thickness for a thick ply depends on the material used. For E-glass/epoxy and carbon/epoxy laminates, Dvorak and Laws [47] calculated the transition thickness between a thin and a thick ply to be approximately 0.7mm , or about 5 to 6 plies.

For the geometry represented in Fig. 3.8, the crack can grow in the transverse or in the longitudinal direction. Comparing Eqs. 3.28 and 3.29 to Eqs. 3.32 and 3.33,

however, indicates that the energy release rate for the crack slit is twice as large in the transverse direction as it is in the longitudinal direction. Since Eqs. 3.28 and 3.29 also indicate that the energy release rate is proportional to the crack length, the crack will grow unstably in the transverse direction. Once the crack reaches the constraining plies, it can propagate in the longitudinal direction, as well as induce a delamination.

Crack propagation is predicted using Eq. 3.38, and the in-situ strengths can be calculated from the corresponding fracture toughness, as expressed in Eqs. 3.30 and 3.31. For mode I, the in-situ transverse tensile strength is defined from Eq. 3.30 as

$$Y_{is}^{t} = \sqrt{\frac{2G_{Ic}^{T}}{\pi a_o \Lambda_b^o}} \tag{3.44}$$

and, taking into account Eq. 3.41,

$$Y_{is}^{t} = 1.12\sqrt{2}Y_t. \tag{3.45}$$

For a thick embedded ply loaded in pure in-plane shear, the expressions get more complex due to shear nonlinearity. The in-situ in-plane ultimate strain is obtained as

$$\gamma_{ab\backslash is}^{u} = \chi^{-1}\left(\frac{2G_{IIc}^{T}}{\pi a_o}\right) \tag{3.46}$$

and, taking into account Eq. 3.42,

$$\gamma_{ab\backslash is}^{u} = \chi^{-1}\left[2\chi\left(\gamma_{ab}^{u}\right)\right]. \tag{3.47}$$

For the definition of g for thick embedded plies, replacing Eqs. 3.45 and 3.47 in Eq. 3.37 results in Eq. 3.43.

Considering the constitutive law for the shear behaviour to be expressed by the function f_{CL} such that

$$\tau = f_{CL}\left(\gamma\right), \tag{3.48}$$

then the in-situ in-plane shear strength is defined as

$$S_{is}^{L} = f_{CL}\left(\gamma_{ab\backslash is}^{u}\right). \tag{3.49}$$

As a particular case of nonlinear in-plane shear behaviour, consider the polynomial relation between the shear strain and the shear stress proposed by Hahn and Tsai

[110],

$$\gamma_{ab} = \frac{1}{G_{ab}}\sigma_{ab} + \beta\sigma_{ab}^3. \tag{3.50}$$

With the nonlinear shear law expressed in Eq. 3.50, Eq. 3.46 reverts to

$$G_{IIc}^T = \pi a_o \left[\frac{\left(S_{is}^L\right)^2}{2G_{ab}} + \frac{3}{4}\beta \left(S_{is}^L\right)^4 \right] \tag{3.51}$$

and Eq. 3.42 can be written as

$$G_{IIc}^T = 2\pi a_o \left[\frac{\left(S^L\right)^2}{2G_{ab}} + \frac{3}{4}\beta \left(S^L\right)^4 \right]. \tag{3.52}$$

Equating Eqs. 3.51 and 3.52, the in-situ shear strength of a thick embedded ply, S_{is}^L, can be related to the shear strength of a unidirectional laminate:

$$\frac{\left(S^L\right)^2}{G_{ab}} + \frac{3}{2}\beta \left(S^L\right)^4 = \frac{\left(S_{is}^L\right)^2}{2G_{ab}} + \frac{3}{4}\beta \left(S_{is}^L\right)^4. \tag{3.53}$$

The in-situ shear strength of a thick embedded ply, S_{is}^L, is the positive, real root of Eq. 3.53:

$$S_{is}^L = \sqrt{\frac{\sqrt{1 + \beta\left(\frac{12\left(S^L\right)^2}{G_{ab}} + 18\beta\left(S^L\right)^4\right)\left(G_{ab}\right)^2} - 1}{3\beta G_{ab}}}. \tag{3.54}$$

It can be observed from Eqs. 3.45 and 3.54 that the in-situ strengths of thick embedded plies—Y_{is}^t, and S_{is}^L—are independent of the ply thickness, as has been observed by Dvorak and Laws [47] and Leguillon [111], and as was shown in Fig. 3.5. The general expression for S_{is}^L in Eq. 3.54 can be written for a linear material by letting β tend to zero, in which case the in-situ in-plane shear strength comes as

$$S_{is}^L = \sqrt{2}S^L \qquad \text{for a linear shear law.} \tag{3.55}$$

Eq. 3.55 is equal to the one obtained by Dvorak and Laws [47] and Dávila et al. [39] for a linear shear behaviour.

3.6.2.5 In-situ strengths of thin embedded plies

Thin plies are defined as having a thickness smaller than the typical defect, $t < 2a_o$, so the slit crack represented in Fig. 3.6 extends across the entire thickness t of the ply, as represented in Fig. 3.9.

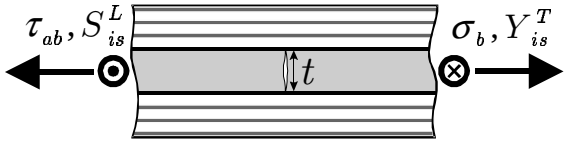

Figure 3.9: Geometry of slit crack in a thin embedded ply, from Ref. [40]

In the case of thin plies, crack defects can only grow in the longitudinal (L) direction, or trigger a delamination between the plies. The in-situ strengths can be calculated from the components of the fracture toughness, as expressed in Eqs. 3.34 and 3.35. For transverse tensile loading, the corresponding strength is expressed as

$$Y^t_{is} = \sqrt{\frac{8G^L_{Ic}}{\pi t \Lambda^o_b}}. \tag{3.56}$$

For a thin embedded ply loaded in pure in-plane shear, the ultimate in-plane shear strain is defined as

$$\gamma^u_{ab\backslash is} = \chi^{-1}\left(\frac{8G^L_{IIc}}{\pi t}\right) \tag{3.57}$$

and the in-situ in-plane shear strength is defined as

$$S^L_{is} = f_{CL}\left(\gamma^u_{ab\backslash is}\right). \tag{3.58}$$

Considering again Eq. 3.50 as a particular case of nonlinear in-plane shear behaviour, Eq. 3.57 can be written as

$$\frac{\left(S^L_{is}\right)^2}{8G_{ab}} + \frac{3}{16}\beta\left(S^L_{is}\right)^4 = \frac{G^L_{IIc}}{\pi t}. \tag{3.59}$$

The in-situ shear strength of a thin ply, S^L_{is}, is the positive real root of Eq. 3.59:

$$S^L_{is} = \sqrt{\frac{\sqrt{1+\beta\frac{48G^L_{IIc}}{\pi t}\left(G_{ab}\right)^2}-1}{3\beta G_{ab}}} \tag{3.60}$$

It can be observed from Eqs. 3.56 and 3.60 that the in-situ strengths are dependent on the thickness t.

Eq. 3.60 can be written for a linear material by letting β tend to zero, in which case the shear strength come as

$$S^L_{is} = \sqrt{\frac{8G_{ab}G^L_{IIc}}{\pi t}} \qquad \text{for a linear shear law.} \tag{3.61}$$

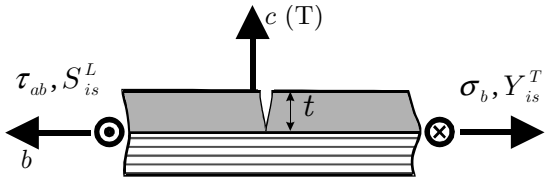

Figure 3.10: Geometry of slit crack in a thin outer ply, from Ref. [40]

Eq. 3.61 is equal to the one obtained by Dvorak and Laws [47] and Dávila et al. [39] for a linear shear behaviour.

If in the absence of specific data, the toughness values G^L_{Ic} and G^L_{IIc} can be assumed to have the values measured by standard Fracture Mechanics tests, such as the DCB for mode I and the ENF test for mode II. For the definition of g for thin embedded plies, the same values can be used to define g as G_{Ic}/G_{IIc}. Using Eq. 3.56, Dvorak and Laws [47] obtained a good correlation between the predicted and experimentally obtained in-situ tensile strengths of both thick and thin 90° plies in $[0/90_n/0]$ laminates, as was shown in Fig. 3.5.

3.6.2.6 In-situ strengths of thin outer plies

Outer plies are taken as a special case of thin plies, as represented in Fig. 3.10. Following the procedure presented for a UD laminate, it is considered that the stress intensity factor of an outer ply is larger than the stress intensity factor of a thin embedded ply. The relation between the stress intensity factors are given by classical fracture mechanics solutions for free-edge cracks. In the case of thin outer plies, crack defects can only grow in the longitudinal (L) direction, or trigger a delamination between the plies. The in-situ strengths of thin outer plies were calculated from the components of the fracture toughness for a linear shear behaviour [41]. For a nonlinear shear response,

$$Y^t_{is} = 1.79\sqrt{\frac{G^L_{Ic}}{\pi t \Lambda^o_b}} \tag{3.62}$$

and

$$\gamma^u_{ab|is} = \chi^{-1}\left(\frac{4G^L_{IIc}}{\pi t}\right). \tag{3.63}$$

As for thin embedded plies, if in the absence of specific data, the toughness

values G_{Ic}^{L} and G_{IIc}^{L} can be assumed to be similar to the corresponding interlaminar fracture toughness and used to define g as G_{Ic}/G_{IIc}.

3.7 Fibre-kinking failure

3.7.1 Literature review

Fibre compressive failure is a field where significant research is still being performed. For matrix compressive failure, a relatively simple mechanical model as the one proposed by Puck and Schürmann [2, 44–46] seems to correctly represent failure, and can be easily expressed as a failure criterion that can be incorporated in numerical codes. However, the mechanics of the failure mode involving fibre compression is more complex. Depending on the material, different fibre compressive failure modes are possible [112]:

Microbuckling. This failure mode consists of the microbuckling of the fibres in the elastic matrix. The first mechanical model for this failure mode can be tracked back to Rosen's work [113] where the fibres are represented by infinite beams[2] in an elastic matrix and failure is attained when the compressive load equals the buckling load. This model provides an upper bound for the failure stress, as it generally predicts a failure stress typically two to three times larger than the experimental one (for carbon reinforced composites [112]). Models based on microbuckling have been widely studied over the last decades. For these models, the matrix shear properties as well as material imperfections play an important role.

Kinking. Kinking can be defined as the localized shear deformation of the matrix, along a band. Typically, the fibres break at the edges of the band, and sometimes also in the interior. It should be noted that some authors consider kinking as a consequence of microbuckling, while others consider it as a separate failure mode [112]. Argon [3] was the first researcher to develop a mechanical model for fibre kinking as a separate failure mode. For Argon, failure is the result of matrix

[2]In fact, Rosen's approach is 2D, and the fibres are thus represented by layers (plates), and not beams.

shear failure, prompted by an initial fibre misalignment. For this model, and those that follow it, matrix elastic behaviour and initial material imperfections play an important role.

Fibre failure. Fibre failure can be expected to occur for fibres with low compressive strength, such as Aramid, but is not expected to happen for carbon, glass or boron fibres [112].

Rosen [113] was the first researcher to propose a mechanical model to describe fibre microbuckling. By minimizing the internal energy, Rosen obtained the fibre's buckling stresses. The analysis was performed for two instability modes: (i) an extension mode, where the deformed shapes of adjacent fibres are in opposition of phase; and (ii) a shear mode, where the deformed shapes of adjacent fibres are in phase. Rosen found that for composites with a high fibre volume fraction, the shear mode is critical, and the associated failure stress is

$$X_c = \frac{G_{matrix}}{1 - V_f} \tag{3.64}$$

where G_{matrix} is the shear modulus of the matrix and V_f is the fibre volume fraction. Considering the rule of mixtures, Eq. 3.64 reduces to $X_c = G_{ab}$, i.e., the shear modulus of the composite. This relation, Eq. 3.64, was later modified to account for an elastic-perfectly plastic resin [114]. In fact, several modifications were attempted, in order to incorporate less restrictive hypotheses (see Ref. [112] for a state of the art review). However, Rosen's approach yields smaller failure stresses than similar models assuming linear elasticity and straight fibres [112] and is simpler. Still, there is little success in predicting the failure stress of advanced composites using Rosen's result. The problem is that, when compared to experimental data, Eq. 3.64 gives results typically 1.5 times higher for Boron composites, 2 to 3 times higher for carbon composites and 4 times higher for glass composites [112]. It was with the introduction of geometric nonlinearity and initial fibre misalignment that the prediction got closer to the experimental results.

Schultheisz and Waas [112] pointed out that most buckling models tend to replicate the model-composite that was studied by Greszczuk [115–118]. Greszczuk performed a series of experiments on model-composites whose reinforcements consisted

of either (i) rods (of steel or aluminum) having diameters in the range 0.5 to 3.2mm ; or (ii) aluminum plates with thickness in the range of 0.3 to 1mm . The basic idea was to duplicate the 2D geometries used in the analytical models. Greszczuk found that the compressive strength of his model-composites exceeded Rosen's prediction. However, when including the energy associated with bending of the fibres, Greszczuk found good agreement. He also concluded that while his model-composites with low-modulus matrix failed by microbuckling, those with intermediate-modulus matrix failed by longitudinal cracking (matrix cracking), and composites with high-modulus matrix failed through compression of the fibres.

Most buckling models follow the 2D approach of Rosen [113]. However, real technical composites are 3D structures. It has been suggested [119, 120] that 3D effects may be a cause of the reduction in the failure stress from Rosen model. Indeed, evidence of the 3D aspect of fibre microbuckling has been reported in the literature [121, 122]. One important 3D consideration, discussed by Schultheisz and Waas [112], is the arrangement of fibres and matrix, which induce different types of interaction (among the fibres and matrix) during the buckling for different packing densities. Furthermore, the laminated construction may lead to different fibre arrangements within the plane of a lamina and in the through-the-thickness direction. Fibre misalignment angles have first been reported to be smaller in the through-the-thickness direction [123], but more recent results suggest they are similar in magnitude [124]. Models incorporating 3D aspects were attempted [118, 125–129], and Schultheisz and Waas [112] concluded that FE analysis would be an excellent candidate to handle the 3D aspect of microbuckling.

In most high fibre-volume-fraction advanced composite materials, compressive failure is seen as a failure mode which is localized in a band across the specimen in which the fibres have rotated by a large amount, and the matrix has undergone large shearing deformation—kinking. A schematic representation of a kink band is shown in Fig. 3.11(a). In the literature, kinking is often seen as a consequence of microbuckling, and not a failure mode itself. However, kinking is other times identified as an independent failure mode. On the discussion on whether or not kinking is a consequence of microbuckling, the main argument has to do with the orientation

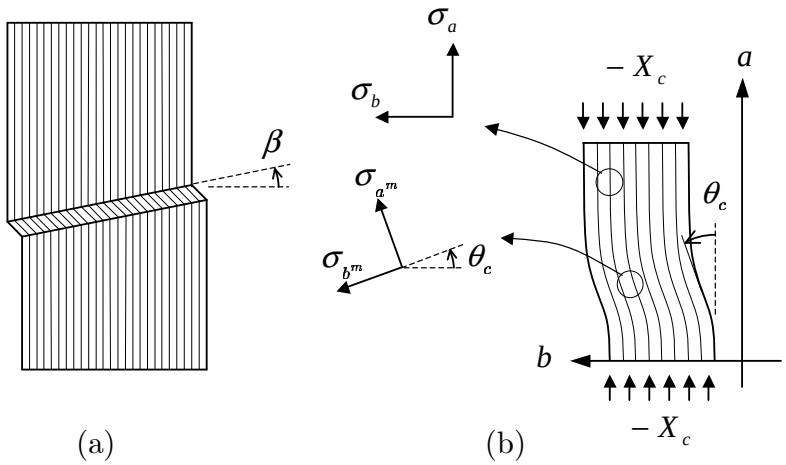

Figure 3.11: (a) Kink band; (b) fibre misalignment frame

of the kink-band boundary. Indeed, if kinking is a consequence of microbuckling, then one would expect the kink-band boundary to lie normal to the loading axis (original fibre direction), i.e., to lie in the plane of highest bending stresses. In Fig. 3.11(a), this would mean an angle β equal to zero. However, it is found that in most cases β lies in the range of 30°. On the other hand, the similarity between the kink bands and shear bands may suggest that shear is the main factor at the onset of kink-band formation. In this case, it would be expected that kink bands would occur in the planes of maximum shear stress, i.e., for $\beta = 45°$. Some thick kink bands have been found near 45° [112], but this is generally not the case.

Another argument supporting kinking as a separate failure mode was introduced by Chaplin [130], who noted that microbuckling should occur everywhere in the composite at about the same time, whereas kinking in his experiments was clearly initiated from some kind of defect.

Effendi et al. [131] carried a set of experimental tests on different carbon-fibre composites and also carried an analytical buckling analysis, which included initial fibre waviness, and computed the stresses in the fibre and matrix constituents. They found that before the buckling load was attained, the stress levels in the constituents exceeded the respective failure stress. To refine the modelling, they conducted a numerical FE analysis, where a nonlinear matrix behaviour was incorporated. The results confirmed that constituent failure happened first. Composites with small

initial imperfections or weaker fibre would fail by fibre failure, while in composites with large initial imperfections or stronger fibres, the matrix would fail first.

On their review of the state of the art on compressive failure of composites, Schultheisz and Waas [112] concluded that the experimental observations on the kinking phenomenon support the contention that kink bands seen in high fibre-volume-fraction advanced composite materials occur via a mechanism that is different from the global microbuckling mode suggested by Rosen [113]. Furthermore, in advanced composites, kinking seems to be initiated by local microstructural defects, such as fibre misalignments and longitudinal (matrix or interfacial) cracking. Therefore, kinking is better understood by treating the problem of stress redistribution, including dynamics, and including both nonlinear geometry and material response.

Whether kinking is a result of fibre microbuckling or a separate failure mode, it is the most common failure feature observed after testing. The kink-band angle and kink width were studied by Hahn [132] for carbon fibre composites (CFC), glass fibre composites (GFC) and Aramid fibre composites (AFC). The kink-band angle β, and the band width w, were found to be the smaller for CFC at room temperature ($\beta \approx 20^\circ$ and $w \approx 0.07$ to 0.2mm). For GFC, no clear kink bands were observed at room temperature. However, at 100°C , a kink angle $\beta \approx 30^\circ$ and a width $w \approx 1.2$mm were observed. For AFC tested at room temperature, the kink angle was found as $\beta \approx 40^\circ$ and width $w \approx 0.45$mm . Chaplin [130] noted the angle of rotation of the fibres in the kink band was twice the angle β, so that no volumetric changes happened in the kinked region.

Argon [3] assumed that an initial fibre misalignment exists in the composite, which leads to shearing stresses between the fibres. The shearing stresses would act as to further rotate the fibres, which would in turn lead to further increase in the shear stresses. This 'closed loop' effect could then lead to failure. The main result from his analysis is the relation between the compressive failure stress, X_c, the longitudinal shear failure stress, S_L, and the initial fibre misalignment angle θ_i (in radians):

$$X_c = \frac{S_L}{\theta_i}. \tag{3.65}$$

From Argon's analysis, a kink-band angle $\beta = 45^\circ$ should also result. Several

authors since reported the sensitivity of the compressive failure stress to the shear failure stress [133–136]. Budiansky [135] later extended Argon's analysis to

$$X_c = \frac{S_L}{\theta_i + \gamma^o} \tag{3.66}$$

where γ^o is the shear strain at failure. Failure occurs when the shear failure stress is reached in the material coordinate system. In a later analytical work, Budiansky and Fleck [136] included the effect of strain-hardening, shear loads, kink-band inclination and finite fibre stiffness, obtaining a non closed-form solution. Another similar solution was obtained assuming kinking in the transverse direction [137] (but not for any generic direction). Analytical models for kink-band broadening were also developed [137]. Kyriakides et al. [138] carried micro-mechanical 2D FE models of the kinking process (modelling fibre and matrix individually), including matrix nonlinearity and initial imperfections. The micro-mechanical 2D FE models were successfully used to predict the propagation stress during kink band broadening [139, 140].

More recently, Dávila et al. [4, 39] used a very interesting combination of Argon's approach [3] and the LaRC02/03 matrix failure criterion. Essentially, Dávila et al. suppose that the fibres might be misaligned, and that further rotation will occur during compressive loading. They then compute the stresses in the updated misalignment frame and check for matrix failure using LaRC02/03 matrix failure criterion.

3.7.2 2D kinking model

A 2D kinking model is now proposed. It is based on Argon's [3] approach and the latter developments by Dávila et al. [4, 39]. In the following, the subscript m applied to the shear stress and shear strain designates the misalignment frame at failure, and the subscript mc (also applied to the shear stress and shear strain) designates the misalignment frame at failure for pure axial compression.

Consider a unidirectional composite with a misaligned region being compressed, as depicted in Fig. 3.11(b). The stresses in the misalignment frame are, for a generic

plane stress loading

$$\begin{aligned}\sigma_{a^m} &= \frac{\sigma_a + \sigma_b}{2} + \frac{\sigma_a - \sigma_b}{2}\cos(2\theta) + \tau_{ab}\sin(2\theta)\\ \sigma_{b^m} &= \frac{\sigma_a + \sigma_b}{2} - \frac{\sigma_a - \sigma_b}{2}\cos(2\theta) - \tau_{ab}\sin(2\theta)\\ \tau_{a^m b^m} &= -\frac{\sigma_a - \sigma_b}{2}\sin(2\theta) + \tau_{ab}\cos(2\theta).\end{aligned} \tag{3.67}$$

3.7.2.1 Determination of the model's parameters using pure axial compression data

For failure under pure compression ($\sigma_a = -X_c$, $\sigma_b \equiv \tau_{ab} = 0$), Eqs. 3.67 lead to

$$\begin{aligned}\sigma_{a^m} &= -X_c\cos^2(\theta),\\ \sigma_{b^m} &= -X_c\sin^2(\theta) \quad \text{and}\\ \tau_{a^m b^m} &= \tau_{mc} = X_c\sin(\theta)\cos(\theta).\end{aligned} \tag{3.68}$$

This stress state can now be placed in an appropriate matrix failure criterion. For a material with linear shear behaviour, placing it in an appropriate matrix failure criterion leads directly to the expression for the specific value of the misalignment angle θ at failure for a pure compression case—θ_c. For a material with nonlinear shear behaviour, it will become clear at the end of this section that kinking can result either from (i) matrix failure (i.e. the verification of a matrix failure criterion), or (ii) instability, due to the loss of (shear) stiffness for larger shear strain values.

Without loss of generality, suppose first the case of failure by the verification of an appropriate matrix failure criterion.

Case 1: Kinking for pure compression as the result of matrix failure

Using Puck's initial criterion [2] or LaRC02/3 [4, 39], Eqs. 3.19 and 3.20 respectively (they yield the same result in this case), gives the expression for the specific value of the misalignment angle θ at failure for a pure compression case—θ_c :

$$X_c\left(\sin(\theta_c)\cos(\theta_c) - \mu_L\sin^2(\theta_c)\right) = S_L. \tag{3.69}$$

This angle, θ_c, is the sum of the initial misalignment and the rotation due to loading.

Dávila et al. [4] have solved Eq. 3.69 for θ_c resulting in

$$\theta_c = \arctan\left(\frac{1-\sqrt{1-4\left(\frac{S_L}{X_c}+\mu_L\right)\frac{S_L}{X_c}}}{2\left(\frac{S_L}{X_c}+\mu_L\right)}\right). \tag{3.70}$$

Dávila et al. pointed out that neglecting μ_L and the shear strain, and assuming θ_c to be small (in Eq. 3.69) yields Argon's equation (Eq. 3.65). In fact, assuming all the above but now not neglecting the shear strain yields Budiansky's Eq. 3.66.

Using the shear constitutive law, the shear strain γ_{mc} can be obtained from the shear stress τ_{mc} and so the initial misalignment angle, θ_i, can be calculated. In practice, the shear constitutive law is usually nonlinear so that the shear strain can be related to the shear stress by the generic function f_{CL} such that $\tau = f_{CL}(\gamma)$. From the constitutive law, the shear stress at failure (and in the material axes) is a function of the shear strain

$$\tau_{mc} = f_{CL}(\gamma_{mc}) \tag{3.71}$$

and from the transformation equations (Eqs. 3.68), the shear stress at an angle θ_c is

$$\tau_{mc} = \frac{1}{2}\sin(2\theta_c)\, X_c. \tag{3.72}$$

From Eqs. 3.71 and 3.72, the shear strain at failure for a pure axial compression case, γ_{mc}, comes as

$$\gamma_{mc} = f_{CL}^{-1}\left(\frac{1}{2}\sin(2\theta_c)\, X_c\right). \tag{3.73}$$

For instance, for a material which is linear in shear, Eq. 3.73 becomes simply

$$\gamma_{mc} = \frac{\sin(2\theta_c)\, X_c}{2G_{ab}}. \tag{3.74}$$

Dávila et al. [4] assumed small angle approximations and reached a simpler expression for Eq. 3.74:

$$\gamma_{mc} = \frac{\theta_c X_c}{G_{ab}}. \tag{3.75}$$

The initial misalignment angle can then be calculated using

$$\theta_i = \theta_c - \gamma_{mc} \tag{3.76}$$

where γ_{mc} can be defined by Eqs. 3.73, 3.74 or 3.75.

Writing Eq. 3.73 in the form

$$f_{CL}\left(\gamma_{mc}\right) = \frac{1}{2}\sin\left[2\left(\theta_i + \gamma_{mc}\right)\right] X_c \tag{3.77}$$

and plotting the left and right hand side of it in a (γ, τ) space provides insight into the meaning of the solution of Eq. 3.73. Fig. 3.12(a) represents both sides of Eq. 3.77 for a material with linear shear behaviour.

The Left Hand Side (LHS) of Eq. 3.77 is the shear strain vs. shear stress material law. The Right Hand Side (RHS) of Eq. 3.77 represents the shear stress resulting from the compressive longitudinal loading, in a rotated coordinate system. As the compressive stress increases, the 'RHS' curve corresponding to a general stress level shifts up, and the intersection with the 'LHS' curve defines the strain in the misalignment frame γ_m. At failure (when the compressive stress equals X_c), the strain in the misalignment frame is defined as γ_{mc} and is shown in Fig. 3.12(a).

For a material with nonlinear shear behaviour, there could be more than one intersection point for each stress level, as represented in Fig. 3.12(b) for the particular case of failure onset. As the compressive loading increases, the 'RHS' curve corresponding to a general stress level shifts up, and the intersection with the 'LHS' curve defines the strain in the misalignment frame γ_m. At failure (when the compressive stress equals X_c), the strain in the misalignment frame is defined as γ_{mc} and is shown in Fig. 3.12(b). Therefore, γ_{mc} has to correspond to the first intersection of the two curves (lower energy). However, this is not guaranteed by the solution of Eqs. 3.70, 3.73 and 3.76. If the mentioned solution corresponds to the second intersection, then the solution is not valid and failure is due to a different mechanism, which is now discussed.

Case 2: Kinking for pure compression as the result of instability

A second mechanism that can promote fibre kinking is elastic instability of the matrix, due to the softening character of the constitutive law. As a composite is progressively loaded in compression, the curve 'RHS' in Fig. 3.12(b) shifts up, also progressively. Suppose that at the moment the two curves 'LHS' and 'RHS' are tangent to each other, Fig. 3.12(c), the matrix compressive failure criterion is not yet verified. Then, a small increase in the compressive load results in the two curves

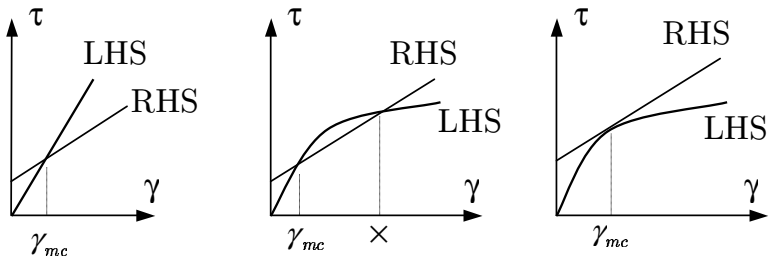

(a) (b) (c)

Figure 3.12: Left and Right hand side of Eq. (3.77), for a material with a (a) linear shear behaviour, (b) nonlinear shear behaviour, and failure by matrix cracking, and (c) nonlinear shear behaviour, and failure by instability

not touching each other. Physically, this means that there is no equilibrium position and catastrophic failure results, due to unstable rotation of the fibres. It is concluded that the compressive strength measured for pure axial compression is in this case actually a failure due to instability, rather than matrix failure.

The values of θ_i and γ_{mc} corresponding to this type of failure can be obtained from the system that results from Eq. 3.77 and the condition that expresses that the left and right hand side of Eq. 3.77 have the same slope at γ_{mc} :

$$\begin{cases} f_{CL}(\gamma_{mc}) = \dfrac{X_c}{2}\sin\left[2\left(\theta_i+\gamma_{mc}\right)\right] \\ \left.\dfrac{\partial f_{CL}(\gamma)}{\partial\gamma}\right|_{\gamma_{mc}} = X_c\cos\left[2\left(\theta_i+\gamma_{mc}\right)\right]. \end{cases} \tag{3.78}$$

To summarize, the three variables θ_i, γ_{mc} and θ_c can be determined by Eqs. 3.70, 3.73 and 3.76 (matrix compressive failure) or by Eqs. 3.76 and 3.78 (elastic instability).

If the instability solution occurs for $f_{mc} < 1$ (Eq. 3.19), then the instability solution must be considered; otherwise the matrix compressive failure solution is considered. Either way, θ_i, γ_{mc} and θ_c are always defined. The initial misalignment angle θ_i is a material property, and could be regarded as an equivalent angle that embodies microstructural defects (that can trigger kink-band formation) as well as the actual initial misalignment, like oscillations in the fibre volume fraction or in the bonding to the resin, or microcracks in the resin.

3.7.2.2 Generic plane-stress loading

Knowing θ_i allows the establishment of an equation defining the shear strain in the material axes for a generic plane stress situation, γ_m, by using the transformation Eqs. 3.67 and the shear law:

$$f_{CL}(\gamma_m) = -\frac{\sigma_a - \sigma_b}{2} \sin\left(2\left(\theta_i + \gamma_m\right)\right) + |\tau_{ab}| \cos\left(2\left(\theta_i + \gamma_m\right)\right). \tag{3.79}$$

Having solved the previous equation for γ_m, the misalignment angle θ comes then as

$$\theta = \frac{\tau_{ab}}{|\tau_{ab}|}\left(\theta_i + \gamma_m\right). \tag{3.80}$$

Note that, in Eq. 3.79, a modulus was applied to τ_{ab} because it is the easiest way of considering simultaneously the possibility of an initial misalignment $\pm\theta_i$.

For a nonlinear shear response, Eq. 3.79 can be solved by an iterative process to yield γ_m. For most practical cases, Eq. 3.79 can be simplified without significant error by assuming small angle approximations:

$$f_{CL}(\gamma_m) \approx \left(\theta_i + \gamma_m\right)\left(-\sigma_a + \sigma_b\right) + |\tau_{ab}|. \tag{3.81}$$

For a linear shear behaviour, Eq. 3.81 can be solved [4], resulting in

$$\gamma_m = \frac{\theta_i G_{ab} + |\tau_{ab}|}{G_{ab} + \sigma_a - \sigma_b} - \theta_i. \tag{3.82}$$

However, for a nonlinear shear behaviour, there might be no easy way of solving Eq. 3.81 or 3.79 without iterating. Having determined the misalignment frame, the stresses can be rotated to that frame, and a matrix failure criterion can be used to check for possible kink-band formation. Therefore matrix failure can be checked using Eq. 3.19 for compression ($\sigma_n \leq 0$) and either Eq. 3.26 (neglecting in-situ effects) or Eq. 3.38 (including in-situ effects) for tension ($\sigma_n > 0$).

For nonlinear shear behaviour, there might be no easy way of solving Eq. 3.79 or 3.81 without iterating. Furthermore, Eq. 3.79 does not always have a solution, since failure by instability is also possible. If, for a specific load state, Eq. 3.79 does not have a solution (this can be easily checked by plotting the left and right hand side of the equation in a (τ, γ) space), then failure has taken place by instability.

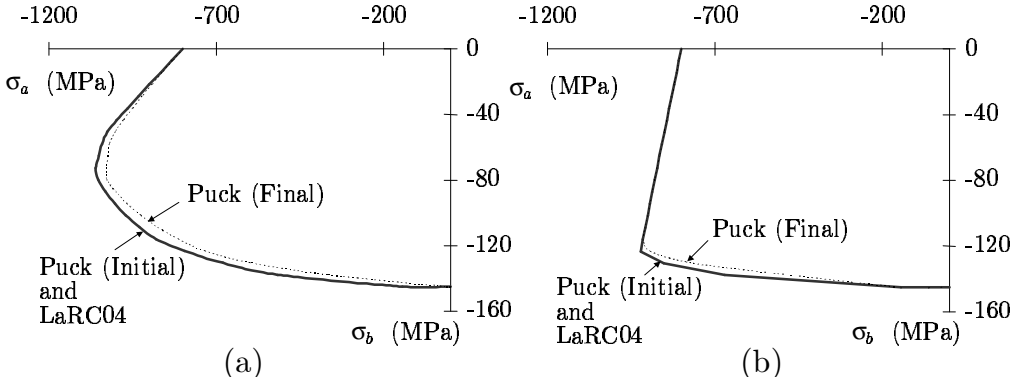

Figure 3.13: Failure envelopes for longitudinal compression acting with in-plane shear for (a) linear shear behaviour and (b) nonlinear shear behaviour

The envelope for failure by instability is defined by the system that results from the following two conditions: (i) Eq. 3.79 is verified; and (ii) the slope (in a (τ, γ) space) of the left hand side of Eq. 3.79 is the same as the slope of the right hand side. Mathematically, the following system results:

$$\begin{cases} f_{CL}(\gamma_m) = -\dfrac{\sigma_a - \sigma_b}{2} \sin\left(2\left(\theta_i + \gamma_m\right)\right) + \left|\tau_{ab}\right| \cos\left(2\left(\theta_i + \gamma_m\right)\right) \\ \dfrac{\partial f_{CL}(\gamma_m)}{\partial \gamma_m} = -\left(\sigma_a - \sigma_b\right) \cos\left(2\left(\theta_i + \gamma_m\right)\right) - 2\left|\tau_{ab}\right| \sin\left(2\left(\theta_i + \gamma_m\right)\right). \end{cases} \tag{3.83}$$

This system (Eq. 3.83) defines an envelope for failure by instability. Fibre kinking is thus predicted not only if the matrix failure criterion (in the misalignment frame) is verified, but also if the system (Eq. 3.83) is verified.

Fig. 3.13 shows the application of this analysis to a biaxial compression in the fibre and matrix direction for a E-glass/DY063 epoxy used in the WWFE [66]. The material properties used are given by Soden et al. [92] and presented in Table 3.1. For the nonlinear behaviour, the experimental data stress vs. strain points given by Soden et al. [92] are used directly by the model (Fig. 3.14).

Fig. 3.13(a) shows the different envelopes obtained while using the LaRC04 matrix compressive failure criterion (Eq. 3.19) and the Puck matrix failure criterion (Eq. 3.21), considering a linear shear behaviour.

Fig. 3.13(b) presents the application of this failure model for a nonlinear shear behaviour (see Eqs. 3.73 and 3.79). Shear nonlinearity was not considered explicitly; instead, interpolation and extrapolation was used to get the required information

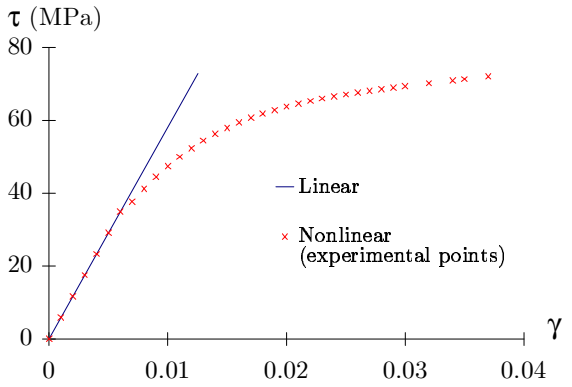

Figure 3.14: Linear and nonlinear shear curves for an E-glass/DY063 epoxy used in the WWFE, experimental points from Soden et al. [92]

from the experimental data points. The linear and nonlinear shear strain vs. shear stress curves are represented in Fig. 3.14. The effect of the nonlinearity on the envelope—Fig. 3.13(b)—is seen to be considerable, which reinforces the importance of a more comprehensive characterization of composite materials under shear loading.

Note the interesting implications of this model: the failure envelope is dependent on the elastic properties of the material. This is common in fibre compressive failure models and in this case reflects the fact that failure takes place in a rotating misalignment frame. Indeed, the magnitude of the rotation of the fibres, γ_{mc}, depends on the shear response.

3.7.3 Proposed 3D kinking model

Most fibre-kinking models assume that kinking happens in the plane of the lamina. On the other hand, most experimental studies mimic this in-plane approach and constrain the specimens so that out of plane movements are not allowed. However, many researchers agree on the 3D nature of fibre-kinking failure. A 3D kinking model based on the previous 2D model is now proposed. This model assumes initial fibre misalignment and nonlinear shear behaviour. Furthermore, its formulation is such that an efficient numerical FE implementation is possible.

Consider a unidirectional lamina under a general compressive stress state as

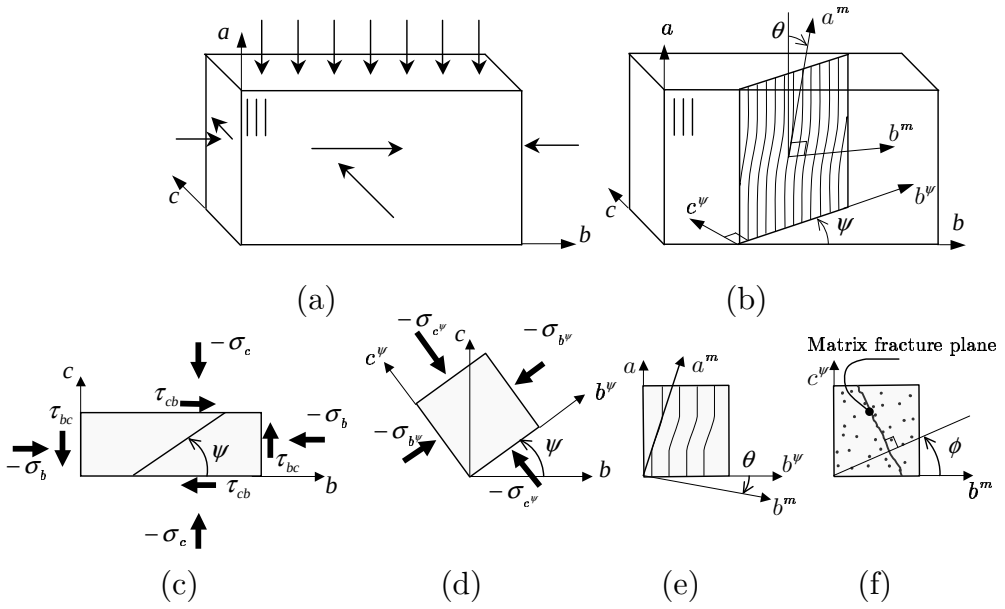

Figure 3.15: 3D kinking model; (a) solid under generic loading, (b) fibre kinking plane, (c) stresses on the (a, b, c) coordinate system, (d) stresses on the (a, b^ψ, c^ψ) coordinate system, (e) stresses on the misalignment frame and (f) matrix fracture plane

shown in Fig. 3.15(a). The fibre-kinking plane is assumed to be at an angle with the b axis, as shown in Fig. 3.15(b). Fig. 3.15(c) shows the stresses acting on the (b, c) plane, while Fig. 3.15(d) shows the stresses acting along the b^ψ and c^ψ directions (Fig. 3.15(d) assumes that b^ψ and c^ψ are the principal directions in the plane (b, c)). The rotation to the misalignment plane is shown in Fig. 3.15(e). The matrix fracture plane is represented in Fig. 3.15(f). The value of the angle ψ depends on the particular stress state[3]. A 2D fibre-kinking model—in which through-the-thickness movements are constrained—assumes that the angle ψ in Figs. 3.15(b), (c) and (d) is equal to zero. If the composite is constrained so that it cannot move in the b direction, then the fibre-kinking plane would have an angle $\psi = 90°$. For a general load situation, ψ will have a value between 0 and 180°.

The set of transformation Eqs. 3.84 can be used to rotate the stresses to a

[3]In reality, defects such as fibre initial misalignment may not be homogeneously distributed and the kinking plane could in fact also be influenced by that.

potential fibre-kinking plane:

$$\begin{aligned}
\sigma_{b^\psi} &= \frac{\sigma_b + \sigma_c}{2} + \frac{\sigma_b - \sigma_c}{2}\cos(2\psi) + \tau_{bc}\sin(2\psi) \\
\sigma_{c^\psi} &= \sigma_b + \sigma_c - \sigma_{b^\psi} \\
\tau_{ab^\psi} &= \tau_{ab}\cos(\psi) + \tau_{ca}\sin(\psi) \\
\tau_{b^\psi c^\psi} &= -\frac{\sigma_b - \sigma_c}{2}\sin(2\psi) + \tau_{bc}\cos(2\psi) \\
\tau_{c^\psi a} &= \tau_{ca}\cos(\psi) - \tau_{ab}\sin(\psi)\,.
\end{aligned} \tag{3.84}$$

After defining the fibre-kinking plane, the stresses are then rotated to the misalignment frame. The strain γ_m is obtained by solving the iterative equation

$$f_{CL}(\gamma_m) = -\frac{\sigma_a - \sigma_{b^\psi}}{2}\sin(2(\theta_i + \gamma_m)) + |\tau_{ab^\psi}|\cos(2(\theta_i + \gamma_m)) \tag{3.85}$$

and the angle θ comes as

$$\theta = \frac{\tau_{ab^\psi}}{|\tau_{ab^\psi}|}(\theta_i + \gamma_m)\,. \tag{3.86}$$

If Eq. 3.85 does not have a solution, then failure has taken place by instability. The envelope for failure by instability is defined by

$$\begin{cases}
f_{CL}(\gamma_m) = -\dfrac{\sigma_a - \sigma_{b^\psi}}{2}\sin(2(\theta_i + \gamma_m)) + |\tau_{ab^\psi}|\cos(2(\theta_i + \gamma_m)) \\
\dfrac{\partial f_{CL}(\gamma_m)}{\partial \gamma_m} = -(\sigma_a - \sigma_{b^\psi})\cos(2(\theta_i + \gamma_m)) - 2|\tau_{ab^\psi}|\sin(2(\theta_i + \gamma_m))\,.
\end{cases} \tag{3.87}$$

Having established the orientation of the misalignment frame, the stresses can be rotated to it using

$$\begin{aligned}
\sigma_{a^m} &= \frac{\sigma_a + \sigma_{b^\psi}}{2} + \frac{\sigma_a - \sigma_{b^\psi}}{2}\cos(2\theta) + \tau_{ab^\psi}\sin(2\theta) \\
\sigma_{b^m} &= \sigma_a + \sigma_{b^\psi} - \sigma_{a^m} \\
\tau_{a^m b^m} &= -\frac{\sigma_a - \sigma_{b^\psi}}{2}\sin(2\theta) + \tau_{ab^\psi}\cos(2\theta) \\
\tau_{b^m c^\psi} &= \tau_{b^\psi c^\psi}\cos(\theta) - \tau_{c^\psi a}\sin(\theta) \\
\tau_{c^\psi a^m} &= \tau_{c^\psi a^\psi}\cos(\theta)\,.
\end{aligned} \tag{3.88}$$

At this point, a check can be performed for matrix failure. For compression ($\sigma_{b^m} \leq 0$), one can apply the already presented matrix compressive failure criterion (Eq. 3.19), while for tensile ($\sigma_{b^m} > 0$) the matrix tensile failure criterion (Eq. 3.26) is applied (in-situ effects are neglected). The criterion for kinking comes then as:

- for $\sigma_{b^m} \leq 0$

$$f_{kink} = \left(\frac{\tau_T}{S_T - \mu_T\sigma_n}\right)^2 + \left(\frac{\tau_L}{S_L - \mu_L\sigma_n}\right)^2 = 1 \tag{3.89}$$

- for $\sigma_{b^m} > 0$

$$f_{kink} = \left(\frac{\sigma_n}{Y_t}\right)^2 + \left(\frac{\tau_T}{S_T}\right)^2 + \left(\frac{\tau_L}{S_L}\right)^2 = 1. \tag{3.90}$$

In Eqs. 3.89 and 3.90, the traction components in the fracture plane are given by

$$\begin{aligned}
\sigma_n &= \frac{\sigma_{b^m} + \sigma_{c^\psi}}{2} + \frac{\sigma_{b^m} - \sigma_{c^\psi}}{2}\cos(2\phi) + \tau_{b^m c^\psi}\sin(2\phi) \\
\tau_T &= -\frac{\sigma_{b^m} - \sigma_{c^\psi}}{2}\sin(2\phi) + \tau_{b^m c^\psi}\cos(2\phi) \\
\tau_L &= \tau_{a^m b^m}\cos(\phi) + \tau_{c^\psi a^m}\sin(\phi)
\end{aligned} \tag{3.91}$$

where the angle ϕ is obtained by trying a small number of tentative angles in the interval $0 \leq \phi < \pi$, and the angle ψ has yet to be determined. A possible solution to determine ψ is to apply the criterion expressed in Eqs. 3.89, 3.87 and 3.90 to a range of tentative angles ψ in the interval $0 \leq \psi < \pi$. For a numerical implementation of the criterion however, the numerical effort dispensed could be cumbersome. It is now shown that it is possible to define a pragmatic expression for ψ.

The analysis of specimens failed by kink-band formation shows that, in the kink band, the fibres rotate consistently in the same direction forming planes of kinked fibres. Consider now an element of volume of a composite, under a generic loading as in Fig. 3.15(a). The stresses acting on a section in the (b, c) plane are shown in Fig. 3.15(c). Suppose that the element of volume fails by the formation of a kink band in its interior; a plane of kinked fibres is shown in Fig. 3.15(b). During (and after) the failure process, the shear stiffness in the failed band is lower than outside it. As a result, if the shear stress $\tau_{b^\psi c^\psi}$ is nonzero, the lower shear stiffness in the kink band would result in an out-of-plane movement of the kinked fibres, which contradicts the assumption that (b^ψ, c^ψ) is the plane where fibre kinking takes place. Therefore, $\tau_{b^\psi c^\psi}$ has to be zero, and b^ψ and c^ψ are thus the principal directions in the plane (b, c), Fig. 3.15(d).

Another argument leading to the same conclusion is that a negative stress σ_{b^ψ} will tend to close any micro-cracks in the matrix (normal to the b^ψ direction) disfavouring fibre kinking in that direction, while a positive stress σ_{b^ψ} will tend to open those same micro-cracks, now favouring fibre kinking. Hence, it is reasonable to expect that the b^ψ is the direction corresponding to maximum principal stress in the plane

Table 3.2: Mechanical properties of a unidirectional E-glass/LY556, from Soden et al. [43, 92]

E_a (GPa)	E_b (GPa)	G_{ab} (GPa)	S_{ab} (GPa)	Y_t (GPa)	Y_c (GPa)	ϕ_o (°)
53.48	17.7	5.83	66.5	37.5	130.3	53

(b, c). Finally, the angle ψ is thus given by

$$\tan(2\psi) = \frac{2\tau_{bc}}{\sigma_b - \sigma_c}. \tag{3.92}$$

To conclude, note that the laminated construction may lead to different fibre arrangements within the plane of a lamina and in the through-the-thickness direction. It is not clear whether initial fibre misalignment angles are smaller in the through-the-thickness direction or similar in magnitude [123, 124]. The present model assumes that the initial fibre misalignment is equal in magnitude in the transverse direction, through-the-thickness direction, or in any direction between the two. In order to apply this model, the only material properties that need to be known, in addition to the in-plane shear response, are Y_c, S_L, ϕ_o, Y_t and X_c. All the remaining parameters follow from these.

3.8 Applications

3.8.1 Failure envelope (σ_b, τ_{ab})

The matrix failure model (compression and tension) is here used to predict the (σ_b, τ_{ab}) failure envelope for a unidirectional composite E-glass/LY556. Material properties, Table 3.2, and experimental data, Fig. 3.16, are given by Soden et al. [43, 92]. Since more than one value is reported for the transverse (compressive and tensile) and shear strengths, the corresponding average values are used in all models.

The envelope predicted by the model is given in Fig. 3.16, where a good correlation with the experimental results can be observed.

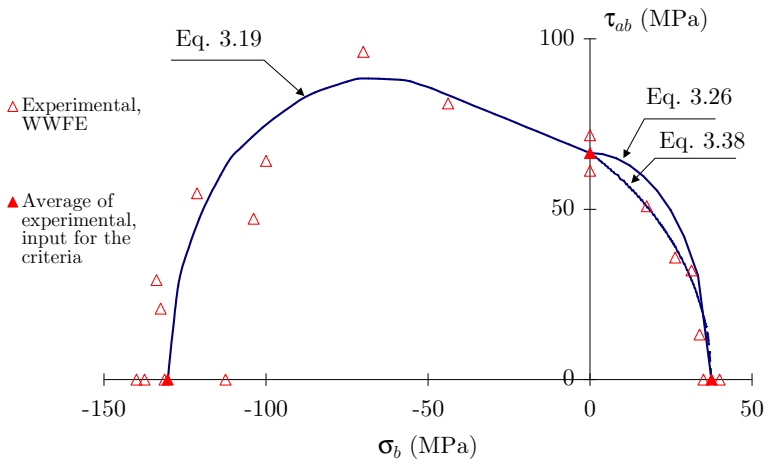

Figure 3.16: Failure envelopes and WWFE test data for unidirectional composite E-Glass/LY556

3.8.2 Failure envelope (σ_a, σ_b)

Testing for biaxial loads presents a number of complexities, and experimental results are rare. A test case from the WWFE [42] is studied here: the biaxial compression of a 0° E-glass/MY750 epoxy lamina, with material properties given in Table 3.3. In addition to those properties, the in-plane Poisson's ratio is $\nu_{ab} = 0.278$, and the fracture angle for pure in-plane transverse compression is $\phi_o = 53°$. For the application of the model with nonlinear shear behaviour, the experimental curve given by Soden et al. [92] is used directly. The linear and nonlinear shear laws are plotted in Fig. 3.17(a).

For the current kinking model, the kink-band angle is predicted using Eq. 3.92. The magnitude of σ_c is unknown, and depends on the existence of constrains on the c direction. Therefore, the two roots of Eq. 3.92 to be considered are $\psi_1 = 0°$ and $\psi_2 = 90°$, meaning that the kink plane can either be in the plane of the lamina, or in the through-the-thickness direction.

Assuming first that the kink band develops in the plane of the lamina ($\psi = 0°$), either due to the micromechanics of the material or imposed by the testing, the failure envelope comes as in Fig. 3.17(b).

If it is assumed that the kink band is formed in the through-the-thickness direction (second root of Eq. 3.92), $\psi = 90°$), the envelope shown in Fig. 3.18(a) is

Table 3.3: Mechanical properties of E-glass/MY750 used in the WWFE [66], given by Soden et al. [43, 92]

	Longitudinal		Transverse		Shear
	Tensile	Compression	Tensile	Compression	
Strength (MPa)	1280	800	40	145	73
Modulus (GPa)	45.6		16.2		5.83

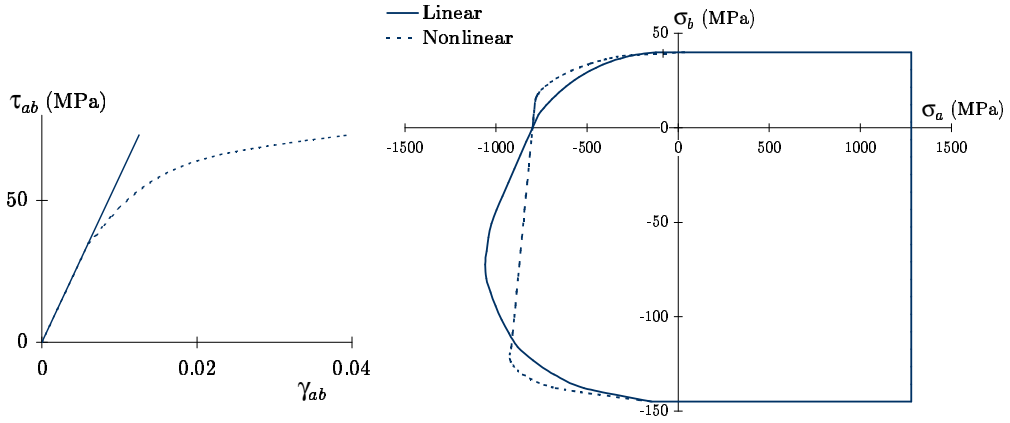

(a) (b)

Figure 3.17: (a) Linear and nonlinear shear law; (b) biaxial (σ_a, σ_b) failure envelope of 0° E-glass/MY750 epoxy lamina, assuming a kink band in the plane of the lamina

predicted. If the orientation of the kink plane is unrestricted, the envelope in Fig. 3.18(b) is obtained.

For biaxial compression, the criteria predicts an increase of the axial compressive strength with increasing transverse compression only for a kink band developing in the plane of the lamina.

3.8.3 Axial compression with superposed hydrostatic pressure

Unfortunately, there is not much experimental data on fibre kinking under a multi-axial stress state. One exception is the compressive behaviour of composite rods, with superposed hydrostatic pressure. Wronsky and Parry [141] measured the effect

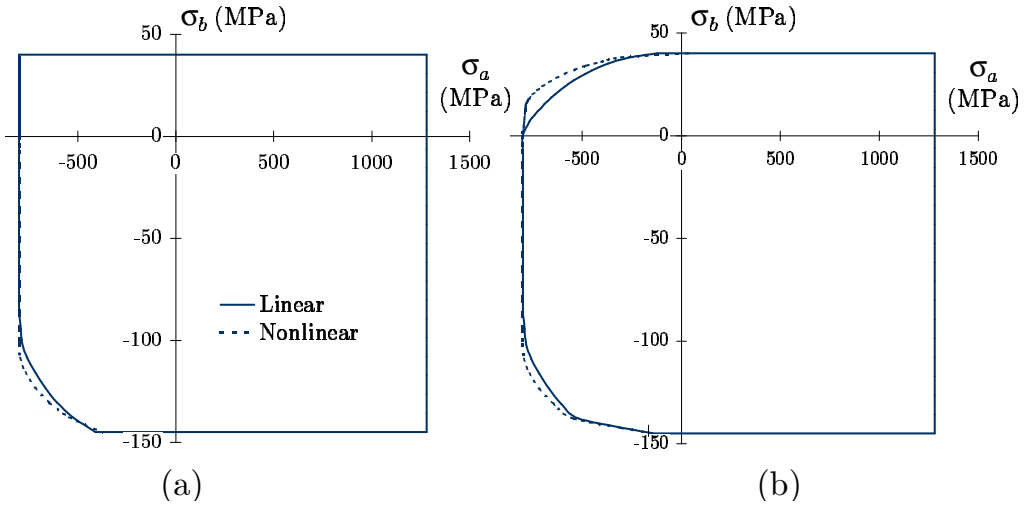

Figure 3.18: Biaxial (σ_a, σ_b) failure envelope of 0° E-glass/MY750 epoxy lamina (a) assuming through-the-thickness kinking; (b) assuming that there are no restrictions to the kinking plane

of hydrostatic pressure on the compressive strength for a glass-reinforced composite. The compressive strength without superposed hydrostatic pressure was measured as 1150 MPa. Three values of shear strength are reported, depending on the test method and specimen dimensions, 42, 48 and 59 MPa. The biggest value of the three is used herein, for being (arguably) more representative.

These material properties are not enough to completely define the material for the purposes of the failure model. Therefore, some material properties have been assumed from typical values as follows: (i) the shear modulus is taken as 6600 MPa, (ii) the fracture angle in matrix compression is $\phi_o = 53°$, (iii) the transverse compressive strength is taken as 140 MPa. To analyse the effect of shear nonlinearity, a logarithmic law is considered, $\tau = k_1 \ln(k_2\gamma + 1)$, with $k_1 = 200$ MPa and $k_2 = 33$, which yields the same initial shear modulus. The linear and nonlinear curves are compared in Fig. 3.19(a).

The effect of the hydrostatic pressure on the compressive strength, as predicted from the model, is compared with the experimental data from Wronsky and Parry [141] in Fig. 3.19(b). The comparison suggests that the physics of the compressive behaviour may have been correctly represented in the model, but clearly, experimental measurements of the assumed material properties are required for a rigorous

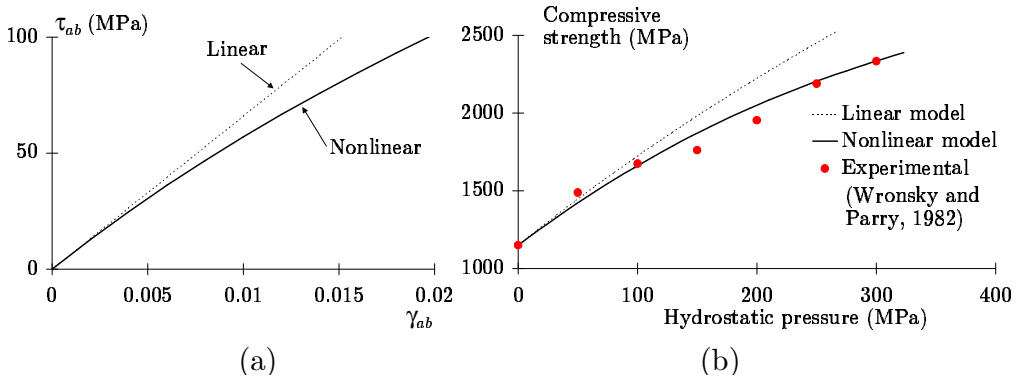

Figure 3.19: (a) Linear and nonlinear shear curves considered; (b) compressive strength as a function of the hydrostatic pressure

validation of the model.

3.8.4 Angle-ply laminate

A last application example is presented, which consists of the compression of carbon-epoxy AS4/3502 laminates with lay-up $(\pm\theta)_{ns}$. For these laminates, the failure can be matrix-dominated or fibre-dominated depending on the angle θ. The material properties used by the model are from Shuart [124]: $E_a = 127.6\,\text{GPa}$, $E_b = 11.3\,\text{GPa}$, $G_{ab} = 6.0\,\text{GPa}$, $\nu_{ab} = 0.3$, $X_c = 1045\,\text{MPa}$, $S_L = 95\,\text{MPa}$ and the shear strain at failure is 4%. In addition to these properties, the model also requires the fracture angle in pure transverse compression, which is considered to be $\phi_o = 53°$. For the nonlinear shear behaviour, the logarithmic law is considered, $\tau = k_1 \ln(k_2\gamma + 1)$, with the constants k_1 and k_2 computed such that the nonlinear curve has the same initial slope as the linear one, and that it passes through the point $(\gamma = 0.04, \tau = 95)$, which yields $k_1 = 58.2\,\text{MPa}$ and $k_2 = 103.1$. The linear and nonlinear shear curves are shown in Fig. 3.20(a) and the predictions from the model are shown to be in good agreement with the experimental data, Fig. 3.20(b). For this application, the influence of the nonlinear shear behaviour does not appear to be particularly important.

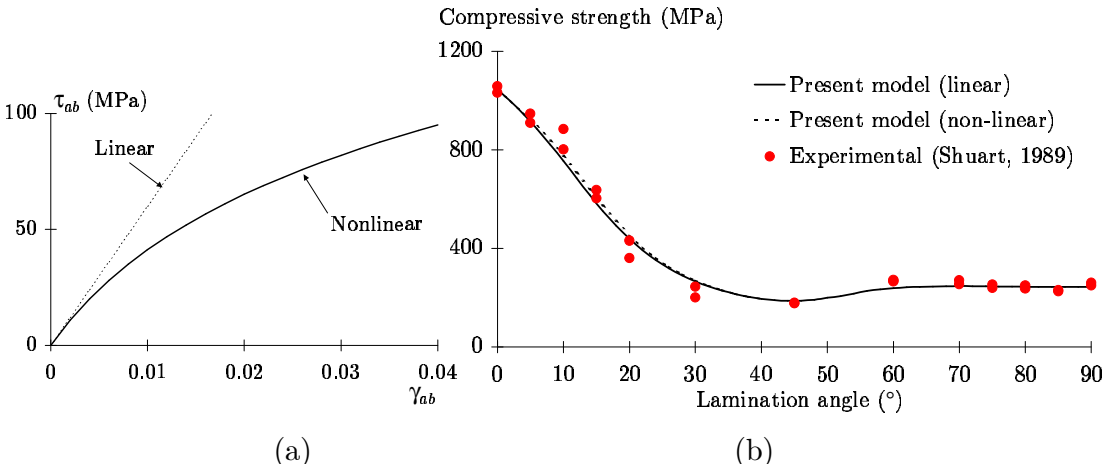

Figure 3.20: (a) Linear and nonlinear shear curves; (b) comparison of the results from the present model to the experimental results from Shuart [124]

3.9 Conclusions

The criteria proposed, and the physically-based models developed, are shown to accurately predict failure envelopes and trends. The fibre compression failure criterion proposed emphasizes the need for accurate characterization of the shear behaviour. The fibre-kinking model can be readily used in a stochastic formulation, since manufacturing defects can be easily accounted for within the model.

The application of these criteria to more complex structures requires the use of numerical methods. An implementation of these criteria in FE is described in the next chapter.

3.10 Publications

The work presented in this chapter resulted in the following publications[4]:

1. S. T. Pinho, L. Iannucci, P. Robinson. Crashworthiness of Composite Structures. Poster presented at GSEPS Research Student Research Symposium, Poster Competition, Imperial College London, 16^{th} July 2003 (won the 2^{nd}

[4]Some of these publications include work from other chapters of this thesis and therefore feature again in the list of publications at the end of the corresponding chapters

prize); *and* at Industrial Affiliates Annual Review Meeting, The Composites Centre, Imperial College London, 25^{th} September 2003

2. S. T. Pinho, L. Iannucci, P. Robinson. Physically-based Failure Models and Criteria for Laminated Fibre-Reinforced Composites: Development, Implementation and Validation. Aero Internal report 02/04, Imperial College London, 2004

3. S. T. Pinho, L. Iannucci, P. Robinson. Recent developments in modelling failure of laminated composite materials. The Composites Centre annual affiliates meeting, Imperial College London, 30^{th} September 2004 (power point presentation)

4. S. T. Pinho, L. Iannucci, P. Robinson. Physically-based Failure Models and Criteria for Laminated Fibre-Reinforced Composites: Development, Implementation and Validation. The Composites Centre annual affiliates meeting, Imperial College London, 30^{th} September 2004 (poster presentation)

5. S. T. Pinho, L. Iannucci, P. Robinson. Physically-based Failure Models and Criteria for Laminated Fibre-Reinforced Composites with emphasis on fibre kinking. Part I Development. In press, Composites Part A, 2005

6. S. T. Pinho, C. G. Dávila, P.P. Camanho, L. Iannucci, P. Robinson. Failure models and criteria for FRP under in-plane or three-dimensional stress states including shear nonlinearity. NASA TM 213530-2005, Langley Research Center, 2005

7. P. P. Camanho, C. G. Dávila, S. T. Pinho, L. Iannucci, P. Robinson. Prediction of In-situ Strengths and Matrix Cracking in Composites under Transverse Tension and in-plane Shear. In press, Composites Part A, 2005

8. S. T. Pinho, L. Iannucci, P. Robinson. Modelling failure using physically-based 3D models and a smeared formulation. 15^{th} International Conference on Composite Materials (ICCM-15). Durban, South Africa, 27^{th} June - 01^{st} July 2005

Chapter 4

Implementation of a smeared failure model

4.1 Introduction

Successfully modelling failure initiation and propagation in composite components is often only possible through the use of numerical methods, such as Finite Elements (FE). One of the most widely used FE codes, LS-Dyna [1], has composite material models with failure already available and applies the Chang and Chang [58, 59] or Tsai and Wu [51] failure criteria. Once failure is detected, the relevant elastic properties are reduced to zero over a fixed number of time steps. This approach is unrealistic, as the post-failure behaviour is completely disregarded.

In order to model damage propagation, continuum constitutive models can feature internal variables representing, directly or indirectly, the density and/or distribution of the microscopic defects that characterize damage. These are called Continuum Damage Mechanics (CDM) models. Ladeveze's CDM model [142], in which the behaviour of fibres (unidimensional phase) and matrix (orthotropic phase) are considered separately, is the basis for a large number of CDM models for composites in the literature, such as that of Coutelier and Rozycki [143] for multi-layered combinations of metallic and composite plies and Johnson's [144] damage model for fabric reinforced composites. Another model, by Matzenmiller et al. [145], is notable for

using a damage growth law which is based on a Weibull distribution of strengths. Williams and Vaziri [146] implemented Matzenmiller et al.'s model in LS-Dyna. In their model, the volumetric energy associated with a failure mode (area under the stress-strain curve) is function of a parameter (m). For a constant value of m, they found that their results were mesh sensitive; however, they argued that, in contrast to the models implemented in LS-Dyna, their model could make use of the parameter m to account for different mesh sizes (m becoming a material property for a specific mesh density). A detailed review of implementation of CDM models is also given by Williams and Vaziri [146]. More recently, Williams et al. [147] developed their model further, addressing in particular the physical significance of the choice of damage parameter, the ease of material characterization and the effect of stacking sequence, and identified rate dependence and mesh size dependence as key areas needing development in the future.

To model failure, the approaches outlined above suffer from a severe mesh dependency problem related to *strain localization* during the fracture process. Strain localization occurs whenever failure is preceded by the emergence of narrow and highly-strained zones. Typical examples of strain localization include shear bands in metals, the formation of kink bands and the accumulation of damage that results in fracture in composites. Local damage formulations are not able to describe the localization phenomena either in a physically or mathematically appropriate way [148]. In this chapter, an FE implementation in LS-Dyna [1] of the failure criteria developed in the previous chapter is presented. The implementation avoids the strain localization problem by using a smeared formulation. Due to the importance of correctly modelling in-plane shear nonlinearity, the implementation accepts any generic curve for the shear law. The FE model only requires parameters with physical meaning. Most of them are typically available from standard tests, and the remaining are shown to either be related to known parameters, or obtainable from simple tests. Even though the model and approach themselves are more general, the implementation is made for LS-Dyna's [1] 8-noded solid brick element with one-point integration. The resulting FE model is easy to use and is shown to have captured some key features of the failure process.

4.2 Failure criteria

The equations relevant to apply the failure criteria developed in the previous chapter are now summarized. As before, the subscript a refers to the fibre direction, the subscript b refers to the in-plane transverse direction and the subscript c refers to the through-the-thickness direction. The values of parameters associated with the onset of failure are denoted with the superscript 'o' while the values of parameters associated with failure propagation are denoted with the superscript 'f'. For instance, σ_a^o is the stress in the a direction at onset of failure.

4.2.1 Fibre tensile failure

For fibre tensile failure, the simple maximum-stress criterion

$$f_{ft} = \frac{\sigma_a}{X_t} = 1 \tag{4.1}$$

is used, where X_t is the axial tensile strength.

4.2.2 Matrix failure

The traction components σ_n, τ_T and τ_L on potential fracture planes are obtained by rotating the stresses in the plane (b, c), with tentative rotation angles ϕ such that $0 \leq \phi < \pi$, see Fig. 4.1(a). Following the exposition in the previous chapter, the FE implementation determines the angle ϕ by computing the failure criterion for a few trial angles from that interval.

4.2.2.1 Compression

For matrix compression ($\sigma_n < 0$), the following criterion is used:

$$f_{mat} = \left(\frac{\tau_T}{S_T - \mu_T \sigma_n}\right)^2 + \left(\frac{\tau_L}{S_L - \mu_L \sigma_n}\right)^2 = 1 \qquad \Leftarrow \sigma_n < 0, \tag{4.2}$$

where S_L and S_T are the longitudinal and transverse (to the fibres) shear strengths; and μ_T and μ_L are transverse and longitudinal friction-like parameters.

To apply this criterion, only the compressive strength Y_c, the longitudinal shear strength, S_L, and the angle, ϕ_o, of the fracture plane for pure compression in the

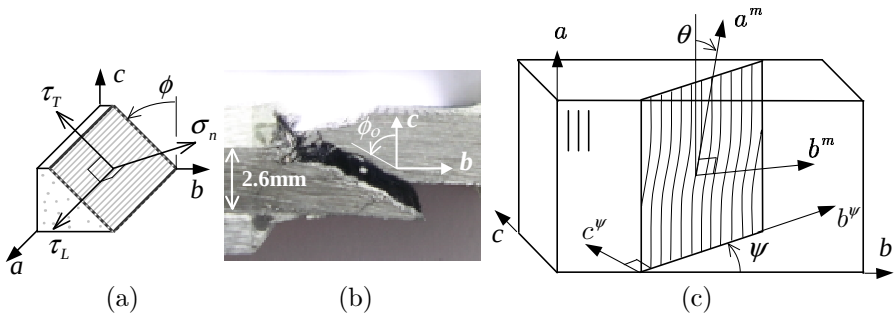

Figure 4.1: (a) Traction components in the fracture plane; (b) failure angle, ϕ_o, for pure transverse compression failure; (c) orientation of a kink band in a 3D space

b direction (typically, $\phi_o \approx 53\,^\circ$) need to be known. This angle is shown in Fig. 4.1(b). All the remaining parameters follow from these:

$$\mu_T = -\frac{1}{\tan(2\phi_o)}, \quad S_T = \frac{Y_c}{2\tan(\phi_o)}, \quad \mu_L = S_L\frac{\mu_T}{S_T}. \tag{4.3}$$

4.2.2.2 Tension

Matrix tensile failure is assumed to occur when the following quadratic interaction between the normal traction component σ_n, and the shear traction components τ_T and τ_L is satisfied:

$$f_{mat} = \left(\frac{\sigma_n}{Y_t}\right)^2 + \left(\frac{\tau_T}{S_T}\right)^2 + \left(\frac{\tau_L}{S_L}\right)^2 = 1 \qquad \Leftarrow \sigma_n \geq 0 \tag{4.4}$$

where Y_t is the transverse tensile strength.

4.2.3 Fibre-kinking failure

To predict fibre-kinking failure, the mechanical model presented in the previous chapter is used, with only one modification that enhances the numerical efficiency. This simple modification, which avoids iterating in each time step, consists of defining the misalignment frame orientation θ as the sum of an initial misalignment angle θ_i with the shear strain in the initial misalignment frame, γ_{mi}. The angles needed

for the definition of the orientation of a kink band are shown in Fig. 4.1(c). The criterion for fibre-kinking is

$$f_{kink} = \begin{cases} \left(\dfrac{\tau_T}{S_T - \mu_T \sigma_n}\right)^2 + \left(\dfrac{\tau_L}{S_L - \mu_L \sigma_n}\right)^2 = 1 \Leftarrow \sigma_n \leq 0 \\ \left(\dfrac{\sigma_n}{Y_t}\right)^2 + \left(\dfrac{\tau_T}{S_T}\right)^2 + \left(\dfrac{\tau_L}{S_L}\right)^2 = 1 \Leftarrow \sigma_n > 0 \end{cases} \tag{4.5}$$

where τ_T, τ_L and σ_n are the traction components on potential fracture planes.

To apply this criterion, the only material property that needs to be known, further to Y_c, S_L, ϕ_o and Y_t is the compressive strength in the fibre direction X_c. All the remaining parameters follow from these.

The stresses in the fibre-kinking plane coordinate system (a, b^ψ, c^ψ) are obtained by rotation in the (b, c) plane by an angle ψ. The angle ψ is obtained either by trying a small number of tentative angles or using the following approximate expression:

$$\tan(2\psi) = \frac{2\tau_{bc}}{\sigma_b - \sigma_c}. \tag{4.6}$$

The stresses are then rotated to the misalignment frame (a^m, b^m, c^ψ) by rotation in the (a, b^ψ) plane by an angle θ defined as

$$\theta = \frac{\tau_{ab^\psi}}{|\tau_{ab^\psi}|}(\theta_i + \gamma_{mi}). \tag{4.7}$$

The initial misalignment angle θ_i is deduced from experimental data by solving the following iterative equation[1]

$$\theta_i = \theta_c - f_{CL}^{-1}\left(\frac{1}{2}\sin(2\theta_i) X_c\right) \tag{4.8}$$

where

$$\theta_c = \arctan\left(\frac{1 - \sqrt{1 - 4\left(\frac{S_L}{X_c} + \mu_L\right)\frac{S_L}{X_c}}}{2\left(\frac{S_L}{X_c} + \mu_L\right)}\right). \tag{4.9}$$

The strain in the initial misalignment frame is defined as

$$\gamma_{mi} = f_{CL}^{-1}\left(\left|-\frac{\sigma_a - \sigma_{b^\psi}}{2}\sin(2\theta_i) + |\tau_{ab^\psi}|\cos(2\theta_i)\right|\right) \tag{4.10}$$

[1]In this model, θ_i is a material property and is therefore computed only once; hence, it is not important that iteration is needed to obtain it.

where f_{CL} is the shear law ($\tau = f_{CL}(\gamma)$).

The traction components in the potential fracture planes are obtained by stress rotation in the plane (b^m, c^ψ) by an angle ϕ comprised in the interval $0 \leq \phi < \pi$, which is obtained by trying a small number of tentative angles.

4.3 Finite element implementation of the smeared failure model

This section describes in detail the 3D FE implementation of the smeared failure model in LS-Dyna [1], for brick elements with one point integration.

4.3.1 Elastic behaviour

The compliance matrix $[S]$, which relates the strain vector $\{\varepsilon\}^T = \{\varepsilon_a\ \varepsilon_b\ \varepsilon_c\ \gamma_{bc}\ \gamma_{ca}\}$ to the elastic or effective stress vector $\{\sigma\}^T = \{\sigma_a\ \sigma_b\ \sigma_c\ \tau_{bc}\ \tau_{ca}\}$, is defined as for any 3D orthotropic material:

$$[S] = \begin{bmatrix} 1/E_a & -\nu_{ba}/E_b & -\nu_{ca}/E_c & 0 & 0 \\ & 1/E_b & -\nu_{cb}/E_c & 0 & 0 \\ & & 1/E_c & 0 & 0 \\ SYM. & & & 1/G_{bc} & 0 \\ & & & & 1/G_{ca} \end{bmatrix}. \tag{4.11}$$

The in-plane shear (ab) is not included in the compliance matrix because the model for this shear mode has been designed to use a full nonlinear shear stress vs. shear strain response, obtained experimentally.

4.3.2 In-plane shear behaviour

According to experimental evidence, the in-plane shear (ab) behaviour is nonlinear and irreversible, even before the localization process. Due to the importance of the nonlinear shear behaviour, this model assumes that the full nonlinear shear stress vs. shear strain curve is available. The curve is entered in the FE model through the

coefficients of a set of polynomials, Fig. 4.2(a). The function $f_{CL}(\gamma_{ab})$ represents the value of shear stress obtained from those polynomials, with $\gamma_{ab} \geq 0$. The effect of σ_b on the in-plane shear curve is not considered. The effect of strain rate is not directly considered but it can be accounted for by using the shear law corresponding to the desired strain rate for the function $f_{CL}(\gamma_{ab})$.

There is no trivial answer to what is the behaviour in shear over very complex loading-unloading-reloading paths. A simple model for unloading, considers a constant unloading modulus (equal to the initial one, G_{ab}) and so needs only the experimental shear stress vs. shear strain curve. A more general approach consists of defining the slope of the unloading law as a function of the inelastic strain. However, this approach would require experimental data for its application that is seldom available. Furthermore, some experimental results suggest that when unloading and reloading, the shear modulus is fairly similar to the initial one, though with some hysteresis [2]. Neglecting the hysteresis, one of the simplest models that accounts for irreversibility is the one presented in Fig. 4.2(b). To define this shear response, one has first to define the maximum (over time) shear strain as

$$\gamma_{ab}^{\max}(t) = \max_{t' \leq t} \{|\gamma_{ab}(t')|\} \tag{4.12}$$

and the inelastic shear strain as

$$\gamma_{ab}^{in} = \gamma_{ab}^{\max} - f_{CL}(\gamma_{ab}^{\max}) / G_{ab}. \tag{4.13}$$

The material law for shear that reproduces the behaviour shown in Fig. 4.2(b) then becomes

$$\tau_{ab} = \begin{cases} \frac{\gamma_{ab}}{|\gamma_{ab}|} f_{CL}(|\gamma_{ab}|) \Longleftarrow |\gamma_{ab}| = \gamma_{ab}^{\max} \\ \frac{\gamma_{ab}}{|\gamma_{ab}|} G_{ab} \langle |\gamma_{ab}| - \gamma_{ab}^{in} \rangle \Longleftarrow |\gamma_{ab}| < \gamma_{ab}^{\max} \end{cases} \tag{4.14}$$

where the operator $\langle \cdot \rangle$ is the Mc-Cauley bracket defined as $\langle x \rangle = \max\{0, x\}$, $x \in \mathbb{R}$.

Even though in-plane shear nonlinearity and irreversibility are modelled, the shear unloading model outlined above may need further development in the future, for situations where the shear stress reverses direction.

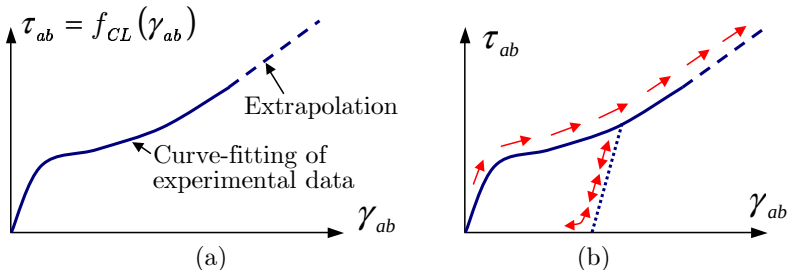

Figure 4.2: (a) Curve fitting of the experimental nonlinear shear behaviour; (b) irreversibility: loading, unloading and reloading paths

4.3.3 Smeared formulation

To avoid strain localization, a smeared formulation [149, 150] is used. In smeared formulations, the fracture energy is distributed (smeared) over the full volume of the element. As a consequence of this approach, a parameter with the dimension of length, relative to the element dimensions, is introduced into the constitutive law. The treatment of localization problems with smeared formulations has been widely used in concrete and in metals [151].

One of the major difficulties related with the smeared-formulation approach is that the material damage laws have to include a length parameter, in order to achieve a constant energy released per unit area of crack generated regardless of the element dimensions. Using the example in Fig. 4.3, matrix tensile fracture, one can easily understand how the length parameter enters the material law. Suppose that the whole plate represented in Fig. 4.3 is modelled as one element. Then, the energy absorbed by the element after complete failure (complete separation), U, is

$$U = V \times \frac{\sigma^o \varepsilon^f}{2} = L_1 L_2 L_3 \times \frac{\sigma^o \varepsilon^f}{2} \tag{4.15}$$

where V is the volume of the element. The basic idea is that this energy is equal to an energy per unit area, Γ, which is a material property, multiplied by the corresponding area, $A = L_1 L_3$, i.e.

$$U = \Gamma \times A = \Gamma \times L_1 L_3. \tag{4.16}$$

Equating Eqs. 4.15 and 4.16, one can retrieve the maximum strain, ε^f, as a function of the energy per units of area of the surface created, Γ, the material strength σ^o

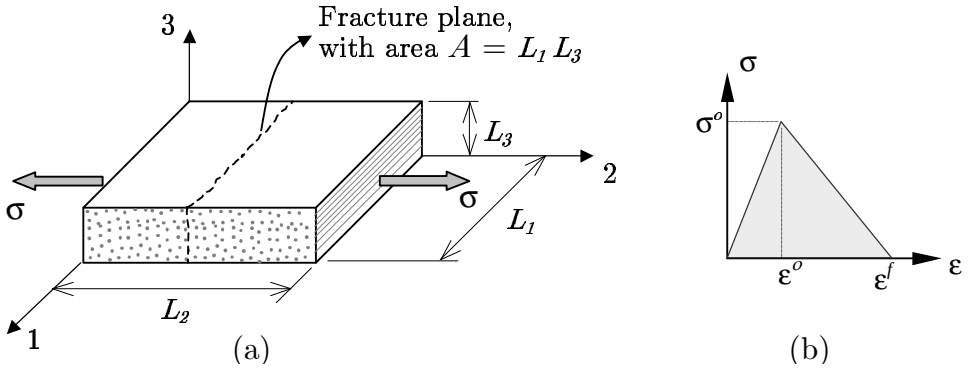

Figure 4.3: (a) Example of a unidirectional composite loaded in transverse (matrix) tension up to complete failure; (b) material law with failure

and one element dimension, L_2:

$$\varepsilon^f = \frac{2\Gamma}{\sigma^o L_2}. \tag{4.17}$$

With ε^f defined by Eq. 4.17, the energy absorbed by the plate (per units of cracked area) in Fig. 4.3 is independent of the mesh refinement $U/A = \Gamma =$ material property. The same does not happen with any of the composite material models currently implemented in LS-Dyna [1].

Another particularly interesting interpretation for this approach is the concept of *width of the damaged zone*. In fact, if one considers that the work done per unit volume of fully damaged material, Γ_v, is a material property, and that the width, w, of the band of failed material is also a material property, then Eq. 4.17 also holds, with $\Gamma = \Gamma_v \times w$.

4.3.4 Damage variables

In CDM models, the stress applied at each point of a structure, which is based on the applied load and the macroscopic cross-sectional area (as if the material was undamaged) is usually referred to in the literature as 'true stress', 'real stress' or 'applied stress.' This stress measure is relevant on a macroscopic point of view, since it represents an average over damaged and undamaged material. In addition, the stress that is based on the cross-sectional area effectively resisting the loading is

frequently referred to as 'effective stress.' From these definitions, the effective stress, σ^{ef}, can be related to the applied stress, σ^{ap}, by

$$\sigma^{ap} = (1 - d)\,\sigma^{ef} \tag{4.18}$$

where d is a damage variable.

In order to avoid superscripts (which could be confused with other indexes used in this work), the operation in Eq. 4.18 will be in the remaining of this chapter represented as

$$\sigma \leftarrow (1 - d)\,\sigma \tag{4.19}$$

meaning that the effective stress (in the right) is replaced by a damaged one (in the left).

Damage variables, d, are defined in this model to degrade linearly the relevant stress components to zero, as defined by Eqs. 4.18 or 4.19 and as shown in Fig. 4.3(b). For each failure mode, the damage variables are defined such that they have the value 0 at onset of failure ($\varepsilon = \varepsilon^o$) and value 1 at final failure ($\varepsilon = \varepsilon^f$). In each time step after failure onset, the relevant effective stress components are multiplied by $(1 - d)$. This way, the applied (or damaged) stress components are progressive and linearly reduced to zero, as in Fig. 4.3(b), without creating a discontinuity. The instantaneous value of the damage variable, d^{inst}, is defined as

$$d^{inst} = \max\left\{0, \min\left\{1, \varepsilon^f \frac{\varepsilon - \varepsilon^o}{\varepsilon\left(\varepsilon^f - \varepsilon^o\right)}\right\}\right\}. \tag{4.20}$$

In order to account for irreversibility, the damage variable is defined as

$$d\left(t\right) = \max_{t' \leq t}\left\{d^{inst}\left(t'\right)\right\}. \tag{4.21}$$

The onset stresses and strains are defined by appropriate failure criteria. The final strain, ε^f, is defined such that the energy absorbed by the crack formed is correctly accounted for, and thus depends on the failure mode predicted.

4.3.5 Modelling the matrix failure mode

After failure is detected (Eqs. 4.2 and 4.4), the traction components in the fracture plane are degraded:

$$\tau_T \leftarrow (1 - d_{mat})\,\tau_T, \quad \tau_L \leftarrow (1 - d_{mat})\,\tau_L \tag{4.22}$$

$$\sigma_n \leftarrow \left(1 - d_{mat}\frac{\langle\sigma_n\rangle}{\sigma_n}\right)\sigma_n. \tag{4.23}$$

Note from Eq. 4.23 that the normal traction component σ_n is only degraded if it is positive, in order to correctly account for the contact between the fracture surfaces. The damage variable for the matrix failure mode, d_{mat}, is obtained from Eqs. 4.20 and 4.21 with the driving strain ε_{mat} defined later in this subsection (in Eqs. 4.20 and 4.21, the variables ε, ε^o and ε^f are replaced by ε_{mat}, ε^o_{mat} and ε^f_{mat} respectively). It is noted once again that the variable d_{mat} has the value 0 at failure onset, and then grows continuously to 1, as a function of the driving strain, during the numerical analysis. In each time step, the operations in Eqs. 4.22 and 4.23 are performed and thus the traction components in the fracture plane are degraded smoothly to zero.

4.3.5.1 Driving strain for the matrix failure mode

From Eqs. 4.20 and 4.21, it follows that a strain variable ε_{mat} 'drives' the damage variable. The history of this strain variable during failure, together with its associated stress σ_{mat}, defines the energy absorbed by the failure process. Therefore, σ_{mat} is the magnitude of the traction in the fracture plane

$$\sigma_{mat} = \sqrt{\langle\sigma_n\rangle^2 + (\tau_{mat})^2} \tag{4.24}$$

with the shear component of the traction τ_{mat} defined as

$$\tau_{mat} = \sqrt{(\tau_T)^2 + (\tau_L)^2}. \tag{4.25}$$

Note in Eq. 4.24 that the normal component of the traction (σ_n) is only considered to contribute to σ_{mat} if σ_n is positive. It results that during a compression situation, the energy will only be absorbed by the shear traction components, which is intended.

The angle of the resultant shear component of the traction, τ_{mat}, with the component τ_T (see Fig. 4.4(a)) is $\lambda = \arctan \tau_L/\tau_T$ and the angle of the magnitude of the traction σ_{mat} with the shear component τ_{mat} (see Fig. 4.4(b)) is $\omega = \arctan \langle \sigma_n \rangle / \tau_{mat}$. Defining the angles λ and ω allows the definition of the strain driving the damage variable. Before proceeding to the definition of the strain variable which drives damage, care has to be taken on the effect of the nonlinearity in the in-plane shear strain. Consider a specimen loaded in uniform pure in-plane shear. For this case, some energy is absorbed uniformly over all the specimen, due to the shear nonlinear (irreversible) behaviour, Fig. 4.4(c). However, at the onset of failure, a localized fracture surface starts forming, resulting in further energy being absorbed. While the energy absorbed due to the nonlinear shear behaviour is proportional to the volume of the specimen, the energy absorbed by the fracture process is proportional to the area created. Only the elastic internal energy in the element at onset of failure contributes to the fracture process. Therefore, a definition of the driving strain considering only the elastic part of γ_{ab} results.

The elastic strain components acting on the fracture plane are

$$\begin{aligned} \varepsilon_n &= \tfrac{1}{2}\left[(\varepsilon_b + \varepsilon_c) + (\varepsilon_b - \varepsilon_c)\cos(2\phi) + \gamma_{bc}\sin(2\phi)\right] \\ \gamma_T &= -(\varepsilon_b - \varepsilon_c)\sin(2\phi) + \gamma_{bc}\cos(2\phi) \\ \gamma_L^{el} &= \gamma_{ab}^{el}\cos(\phi) + \gamma_{ca}\sin(\phi), \end{aligned} \tag{4.26}$$

where the elastic component of the in-plane shear strain is defined as

$$\gamma_{ab}^{el} = \frac{\tau_{ab}}{G_{ab}}. \tag{4.27}$$

From the definition of the angle λ, it follows that the elastic component of the shear strain acting on the fracture plane, in the direction of τ_{mat}, is expressed as

$$\gamma_{mat} = \left|\gamma_T \cos\lambda + \gamma_L^{el}\sin\lambda\right|. \tag{4.28}$$

From the definition of angle ω, the driving strain, acting on the direction of σ_{mat} is defined as follows:

$$\varepsilon_{mat} = \frac{\langle \sigma_n \rangle}{\sigma_n}\varepsilon_n \sin\omega + \gamma_{mat}\cos\omega. \tag{4.29}$$

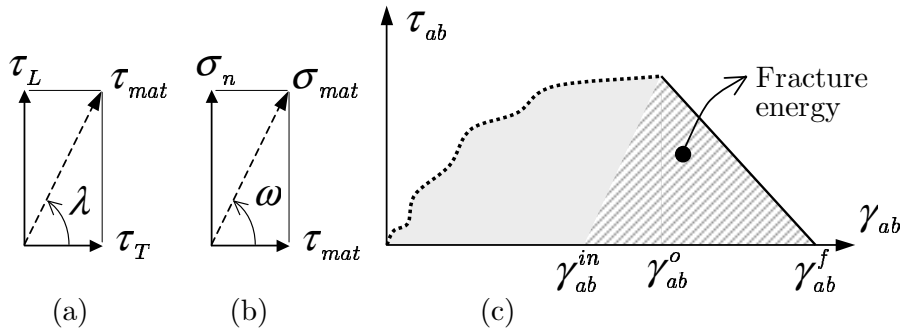

Figure 4.4: (a) Definition of λ; (b) definition of ω and (c) fracture energy for in-plane shear

4.3.5.2 Onset strain and final strain for the matrix failure mode

The onset stress and strain are determined from the value of σ_{mat} and ε_{mat} at the onset of failure:

$$\sigma_{mat}^{o} = \sigma_{mat|f_{mat}=1}\,, \quad \varepsilon_{mat}^{o} = \varepsilon_{mat|f_{mat}=1}\,. \tag{4.30}$$

Following Eq. 4.17 and Fig. 4.3(b), the expression for ε_{mat}^{f} is

$$\varepsilon_{mat}^{f} = \frac{2\Gamma}{\sigma_{mat}^{o} L_{mat}}. \tag{4.31}$$

The characteristic length L_{mat} in Eq. 4.31 (necessary to define ε_{mat}^{f}) has to be determined. For the case when the fibres are aligned with the element direction, it is clear (see Fig. 4.3(a)) that the characteristic length is $L_{mat} = L_2$. For a generic case, the characteristic length should be such that $L_{mat} = V/A$, where V is the element volume and A is the fractured area, and is given in Appendix D.

The fracture toughness Γ in Eq. 4.31 is the last term which needs to be determined. For pure tensile failure (positive σ_n acting alone), Γ is the mode I intralaminar fracture toughness. For a carbon-epoxy T300/913, the authors have determined this property using four-point bending tests with pre-cracked specimens, and obtained $\Gamma_b = 0.22\,\mathrm{kJ/m^2}$, see Chapter 5. This value is similar to the mode I interlaminar fracture toughness for the same material, which can be attributed to the similarity in the fracture mode. The situations when either τ_T or τ_L act alone result in a pure mode II intralaminar fracture. It thus seem reasonable to extrapolate the previous result obtained for mode I to mode II, in the absence of

experimental data, i.e. to use $\Gamma_T = \Gamma_L = G_{IIc}$ (where the fracture toughness values Γ_T and Γ_L correspond to τ_T and τ_L acting alone, respectively; and G_{IIc} is the mode II interlaminar fracture toughness).

For a mixed-mode situation (σ_n, τ_T and τ_L acting all at the same time), mixed-mode criteria developed for interlaminar fracture such as the power-law [11]

$$\left(\frac{G_I}{G_{Ic}}\right)^{\alpha} + \left(\frac{G_{II}}{G_{IIc}}\right)^{\alpha} = 1 \tag{4.32}$$

can be used here resulting in the following expression for Γ

$$\Gamma = \left[\left(\frac{1}{\Gamma_b}\left\langle\frac{\varepsilon_n^o \sigma_n^o}{\varepsilon_{mat}^o \sigma_{mat}^o}\right\rangle^2\right)^{\alpha} + \left(\frac{1}{\Gamma_T}\left(\frac{\gamma_T^o \tau_T^o}{\varepsilon_{mat}^o \sigma_{mat}^o}\right)^2\right)^{\alpha} + \left(\frac{1}{\Gamma_L}\left(\frac{\gamma_L^{el,o} \tau_L^o}{\varepsilon_{mat}^o \sigma_{mat}^o}\right)^2\right)^{\alpha}\right]^{-1/\alpha}. \tag{4.33}$$

For a carbon-epoxy T300/913, the authors obtained α by the best fit of mixed-mode interlaminar experimental results as $\alpha = 1.21$. For materials where other propagation criteria are thought to be more appropriate than the power law, these criteria can be easily implemented in the model, provided they can be expressed as $\Gamma = f(\Gamma_b, \Gamma_T, \Gamma_L, \cdots)$. In particular, if no mixed-mode data is known at all, a simple weighted average of Γ_b, Γ_T and Γ_L might be appropriate:

$$\Gamma = \Gamma_b \left\langle\frac{\sigma_n^o}{\sigma_{mat}^o}\right\rangle^2 + \Gamma_T \left(\frac{\tau_T^o}{\sigma_{mat}^o}\right)^2 + \Gamma_L \left(\frac{\tau_L^o}{\sigma_{mat}^o}\right)^2. \tag{4.34}$$

4.3.5.3 Discussion

From Eq. 4.31, it results that for very coarse meshes ($L_{mat} \to \infty$), ε_{mat}^f tends to zero. Therefore, there is a critical element size at which ε_{mat}^f equals ε_{mat}^o, and the actual elements should be smaller than that. The physical interpretation for this phenomenon is that for a very coarse mesh, it is possible for an element to have more elastic energy at failure onset, than the energy necessary for the formation of a crack across it. In these situations, the only possibility for the element to absorb the correct amount of energy is the strains decreasing as the stresses are degraded. However, this is not possible to control via a user-element in an explicit FE code like LS-Dyna. In the actual implementation of this failure model, a warning is issued if $\varepsilon_{mat}^f < \varepsilon_{mat}^o$ and the analysis continues with $\varepsilon_{mat}^f = \varepsilon_{mat}^o$ for the element affected.

The consequence is that the elements falling in this category will absorb more energy than they should during failure. It is then up to the user to conclude whether the results are reasonable (based on the number of warnings), or to re-run the analysis with a more refined mesh in the region of the elements affected.

Finally, for a simple one dimensional problem, or for a situation where Poisson's effects are not considered (this is the case for interface or decohesion elements) the definition of the damage variable in Eqs. 4.20 and 4.21, with the final strain computed from Eq. 4.31 yields the exact energy absorption specified. However, for any 3D material model, the stress vs. strain curves do not have to pass exactly through the origin due to the Poisson's effect (for instance, for a zero stress in the b direction, the corresponding strain ε_b will be in general nonzero if stresses are already acting in the a and c directions). A small error results from this fact. In order to avoid this error in a numerical implementation, the full stress vs. strain paths would need to be kept in memory, which seems cumbersome. The error can however be quantified and proven to be small, using a particular example. With this purpose, consider a carbon-epoxy T300/913 with properties given in Table 4.1, which fails due to the stress in the b direction, but which has a constant superposed stress σ_a in the a direction, existing since before any loading in the b direction was applied. The error in the energy absorbed can be computed for this simple case, by considering the area under the ε_b vs. σ_b curve. Even for a particularly high superimposed stress $\sigma_a = 1000\,\mathrm{MPa}$, the error (which is proportional to σ_a), is only about 4%, considering a characteristic length $L = 0.5\,\mathrm{mm}$. This aspect warrants further investigation in the future.

4.3.6 Modelling the fibre-kinking failure mode

Fibre-kinking failure is detected using Eq. 4.5. After failure is detected, the shear stresses in the kink-band, $\tau_{a^m b^m}$ and $\tau_{c^\psi a^m}$, are degraded, as well as (depending on the sign of σ_{a^m}) the stress normal to the kink band. This is done using a damage

variable, d_{kink}:

$$\tau_{a^m b^m} \leftarrow (1 - d_{kink})\, \tau_{a^m b^m}, \quad \tau_{c^\psi a^m} \leftarrow (1 - d_{kink})\, \tau_{c^\psi a^m}, \tag{4.35}$$

$$\sigma_{a^m} \leftarrow \left(1 - d_{kink} \frac{\langle \sigma_{a^m} \rangle}{\sigma_{a^m}}\right) \sigma_{a^m}. \tag{4.36}$$

The damage variable for the fibre-kinking failure mode, d_{kink}, is obtained from Eqs. 4.20 and 4.21 with the driving strain ε_{kink} defined later in this subsection (in Eqs. 4.20 and 4.21, the variables ε, ε^o and ε^f are replaced by ε_{kink}, ε^o_{kink} and ε^f_{kink} respectively).

4.3.6.1 Driving strain for the fibre-kinking failure mode

During fibre-kinking failure, energy is dissipated by the bending and eventual breaking of each individual fibre, as well as by matrix cracking in the kink band. These failure processes are associated with the rotation of fibres in the kink band, which is due to the shear stress $\tau_{a^m b^m}$. Therefore, at the scale of the kink-band, failure propagation is controlled by the driving stress $\sigma_{kink} = \tau_{a^m b^m}$. Proceeding like before, the inelastic component of γ_{ab} is not considered for the driving strain, which is thus defined as $\varepsilon_{kink} = \gamma^{el}_{a^m b^m}$, where $\gamma^{el}_{a^m b^m}$ is obtained by rotation of the elastic strains (γ_{ab} replaced by γ^{el}_{ab} as defined by Eq. 4.27).

4.3.6.2 Onset strain and final strain for the fibre-kinking failure mode

The onset stress and strain are defined as

$$\sigma^o_{kink} = |\sigma_{kink}|_{|f_{kink}=1}\,, \quad \varepsilon^o_{kink} = |\varepsilon_{kink}|_{|f_{kink}=1} \tag{4.37}$$

and the expression for the final strain ε^f_{kink} is

$$\varepsilon^f_{kink} = \frac{2\Gamma_{kink}}{\sigma^o_{kink} L_{kink}}. \tag{4.38}$$

The characteristic length L_{kink} in Eq. 4.38 is determined in Appendix D for a generic orientation of the kink band within a brick finite element.

Finally, the energy Γ_{kink} can be obtained by experiments. Soutis and Curtis [152] loaded a plate of carbon-epoxy T800H/924C with layup $(0, 90_2, 0)_{3S}$ containing a

central crack in compression. From their work, it can be concluded (see Chapter 6) that the critical energy release rate for kinking, for T800H/924C, is about $76\,\mathrm{kJ/m^2}$. For another material, T300/913, the author of this thesis carried out tests using Compact Compression Specimens (CCS are like Compact Tension Specimens (CTS), but loaded in compression), having obtained $\Gamma_{kink} = 79.9\,\mathrm{kJ/m^2}$, see Chapter 6.

4.3.7 Modelling the tensile fibre failure mode

Fibre tensile failure is predicted using the criterion expressed through Eq. 4.1. When this criterion is fulfilled, the material response is changed to account for the changes in the structure, i.e., the catastrophic behaviour observed in experimental tests:

$$\{\tau_{ab}, \tau_{bc}, \tau_{ca}\} \leftarrow (1 - d_{ft})\,\{\tau_{ab}, \tau_{bc}, \tau_{ca}\} \quad \text{and} \tag{4.39}$$

$$\sigma_i \leftarrow \left(1 - d_{ft}\frac{\langle\sigma_i\rangle}{\sigma_i}\right)\sigma_i \quad \text{with} \quad i = a, b, c. \tag{4.40}$$

The damage variable for the fibre tensile failure mode, d_{ft}, is directly driven by the strain ε_a, since the fibre tensile failure criterion is a function of only σ_a. It is obtained from Eqs. 4.20 and 4.21 (with the variables ε, ε^o and ε^f replaced by ε_a, ε_a^o and ε_a^f respectively).

The onset stress and strain are defined as

$$\sigma_a^o = \sigma_a\big|_{f_{ft}=1}, \quad \varepsilon_a^o = \varepsilon_a\big|_{f_{ft}=1}. \tag{4.41}$$

The final strain ε_a^f is defined as

$$\varepsilon_a^f = \frac{2\Gamma_a}{\sigma_a^o L_a} \tag{4.42}$$

where Γ_a and L_a still have to be determined. The determination of L_a is presented in Appendix D. The fracture toughness associated with the fibre tensile failure mode (Γ_a) was obtained by the authors using CTS for a carbon-epoxy T300/913 as $\Gamma_a = 91.6\,\mathrm{kJ/m^2}$, see Chapter 6.

4.4 Mesh dependency

The formulation presented should avoid the mesh dependency characteristic of most failure models. Fig. 4.5 shows four different meshes for a square specimen, loaded by an uniform tensile stress in the b direction (by imposing a uniform displacement). Mesh (a) consists of a single element, while meshes (b), (c) and (d) have 3^2, 9^2 and 27^2 elements respectively. No artifice is used to trigger failure at any specific location, or along any particular direction.

It can be seen from Figs. 4.5(b)-(d) that fracture is always predicted in a band normal to the loading direction, as expected, and is always smeared over the width of one element. Moreover, the load-displacement curve (and thus the energy absorbed) is independent of mesh refinement and of the width of the failed region, as shown in Fig. 4.5(e). This is an important feature, given that complete failure takes place.

A final aspect is worth mentioning. This FE formulation avoids pathological mesh dependency in the energy absorbed. However, with this FE formulation, as with any other standard FE formulation, the volume of damaged material is still mesh dependent. This aspect is a shortcoming of the FE method in representing reality, and is a consequence of the spacial discretization of the continuum. For complex structures, the effect of the mesh is expected to be particularly noticeable when the dimension over which failure is smeared (dependent on mesh size) is not negligible in comparison to other dimensions of the structure. The need for refined meshes to capture the correct damage zone/ path is similar to the need for refined meshes to capture the correct stress gradient.

4.5 Applications

4.5.1 Standard tests

The ability of the material model implemented in LS-Dyna [1] to reproduce the physics of shear and compression failure is here assessed. Standard experimental tests were carried with carbon-epoxy T300/913 (see Appendix A). The numerical models presented in this sub-section reproduce the geometry of specimens that were

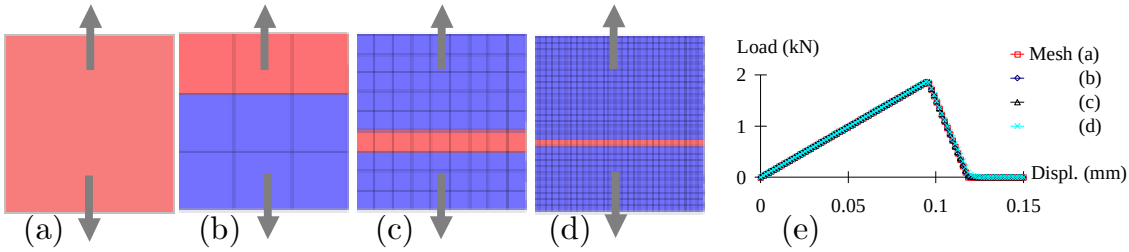

Figure 4.5: Models with different mesh densities; the failed elements are identified by a lighter colour; (a) shows the material axes; (b), (c) and (d) show the fracture planes; (e) load vs. displacement curves for different mesh refinement levels

actually tested, and use the material properties obtained. The objective is to assess the model's capability to predict the main failure features observed experimentally, such as the inclined fracture for the transverse compression test, the $\pm 45\,^{\circ}$ failure for the shear specimen and the kink-band formation for the longitudinal compression specimen. Note that none of these features is directly included in the model.

The elastic properties and strengths, obtained experimentally, are presented in Table 4.1. The experimental in-plane shear stress vs. strain curve was used as input for the numerical model, the Poisson's ratio ν_{ba} was obtained as 0.021 and the fracture angle for pure transverse compression was measured as $\phi_o = 53\,^{\circ}$. Regarding the through-the-thickness (c) direction, the composite was assumed transversely isotropic, with $\nu_{bc} = 0.4$. The shear modulus G_{ca} was taken as being equal to the (initial) in-plane shear modulus (G_{ab}), and the Poisson's ratio ν_{ca} as ν_{ba}. The intralaminar toughness was measured experimentally using 4-point bending tests as $\Gamma_b = 0.22\,\mathrm{kJ/m^2}$, and Γ_{kink} and Γ_a were obtained using CTS and CCS as $\Gamma_{kink} = 79.9\,\mathrm{kJ/m^2}$ and $\Gamma_a = 91.6\,\mathrm{kJ/m^2}$ respectively, see Chapters 5 and 6. The toughness values Γ_T and Γ_L were taken as the mode II interlaminar fracture toughness for the same material, $\Gamma_T = \Gamma_L = 1.1\,\mathrm{kJ/m^2}$, see Appendix B.

In all the examples that follow, an element with slightly lower strength was used to trigger failure close to the middle of the specimen.

Table 4.1: Mechanical properties of T300/913 and HSC/913

Material	E_a (GPa)	E_b (GPa)	G_{ab} (GPa)	X_t (MPa)	X_c (MPa)	Y_t (MPa)	Y_c (MPa)	S_{ab} (MPa)
T300/913	132	8.8	4.6	2005	1355	68	198	150
HSC/913	130	9.2	4.6	1650	1100	60	200	100

4.5.1.1 Modelling shear failure of a $(\pm 45)_{8S}$ test specimen

Shear tests were carried with $(\pm 45)_{8S}$ specimens (angles relative to the loading direction), tested in tension, according to the appropriate ASTM standard [153], see Fig. 4.6(a). The shear stress vs. strain curve was nonlinear almost from the beginning of the test, but no strain localization was present until immediately before final failure, which happened at a shear strain of about 25%. The data reduction was done according to the ASTM standard [153], but, in order to obtain the full strain vs. stress curve, fibre scissoring and width reduction were taken into account. (Fibre scissoring was taken into account by considering the current orientation of the fibres in the data reduction (affected by the shear strain), rather than assuming that they remain at $45\,^\circ$. The applied stress was calculated by dividing the load by the current cross-sectional area, where the reduction in width was computed using the strains from the transverse strain gauge.)

An FE model of part of the specimen, containing the failed region, is presented in Fig. 4.6(b). The model has the same dimensions as the actual specimen—except for the length, which is smaller. The model has 16 solid elements across the thickness, in order to simulate each layer individually. The $\pm 45\,^\circ$ failure can be observed in Fig. 4.6(b), and results from the damage variable affecting the *local* shear traction components in the predicted fracture plane, within each element. (In fact, when the shear stress is reduced at some angle β, it is also reduced at an angle $\beta + 90\,^\circ$. This may give rise to unrealistic failure patterns, and is a feature typical to CDM-based models.) The numerical load vs. displacement curve is compared to the experimental in Fig. 4.6(c). The experimental displacement was computed by multiplying the strain in the longitudinal strain gauge by the length of the numerical specimen.

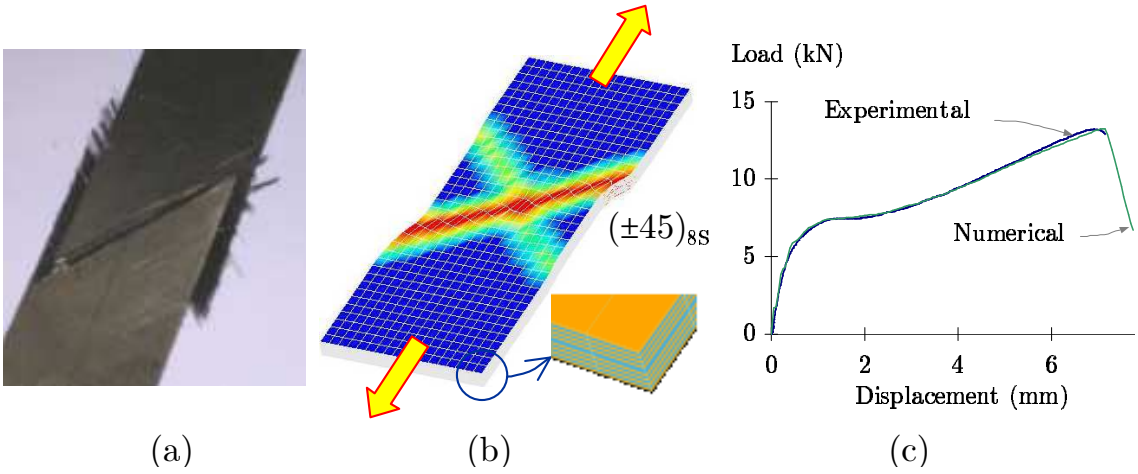

Figure 4.6: (a) Shear specimen; (b) model of the shear specimen; (c) experimental and numerical load vs. displacement curves

For the good agreement obtained, the consideration of fibre scissoring and width reduction in the data-reduction were key factors, as well as the FE code's capability to handle large rotations appropriately.

4.5.1.2 Modelling matrix compression failure

Pure transverse compression tests were carried out, and a typical fracture surface is shown in Fig. 4.1(b). Fracture occurred at an angle of 53 ° with the thickness direction. A numerical model of this specimen was created, and is shown in Fig. 4.7. The fracture angle predicted by each failed element, available as a history variable, is 53 °. This correct prediction is a consequence of the matrix compression failure criterion, expressed in Eq. 3.19, being maximized for this angle, when the material is subjected to pure transverse compression. The angle of the band of failed material (smeared fracture surface), which can be observed in Fig. 4.7, is about 50 °. In this case, the correct prediction results from the shear traction components being degraded in a coordinate system aligned with the predicted fracture plane. If the failed elements in this example had been deleted immediately after they failed, the contact between the fracture surfaces would have not been properly modelled during the propagation of the fracture surface (failed band) across the specimen. The author has observed this to affect the angle of the failed band observed in the numerical

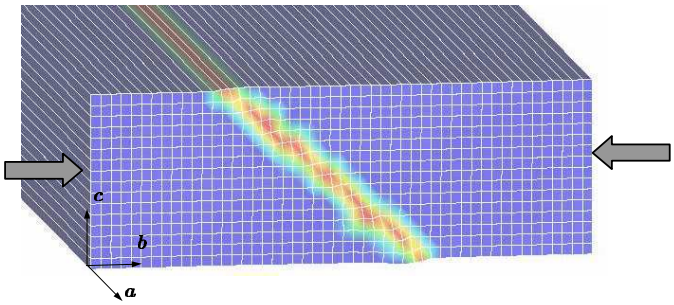

Figure 4.7: Model of the transverse compression test specimen

specimen.

4.5.1.3 Modelling fibre compression failure

The formation of kink bands at a small angle β with the normal to the loading direction is predicted by the model, as a result of the damage variable acting on the shear stress in the misalignment frame. For T300/913, the author has observed it to be about $25 \pm 5\,^{\circ}$ for out-of-plane kinking in CCS (see Chapter 6), and $20 \pm 5\,^{\circ}$ for standard axial compression specimens with in-plane kinking, Fig. 4.8(a). Fig. 4.8(b) shows the FE mesh of an axial compression specimen, with the corresponding loading. The formation of the kink band can be observed in Figs. 4.8(c) to (e). The predicted kink band angle is about $15\,^{\circ}$. After the kink band is formed, further loading leads to kink-band broadening, as observed in Fig. 4.8(e).

Kink fronts have been reported to reorient themselves naturally, as they propagate, before stabilizing in a β direction [154] and the tip of kink bands to lie at different angles than the rest of the kink band [155]. These observations emphasize the role of damage propagation within the kink band, for the definition of its final orientation. Turning to the numerical model, the kink band orientation observed in Figs. 4.8(c) to (e) is never predicted explicitly, and is the result of the shear traction component being degraded in the misalignment coordinate system, whose orientation is updated during damage propagation. The author has observed that not updating the misalignment frame (where the traction components are degraded) results in a smaller angle predicted.

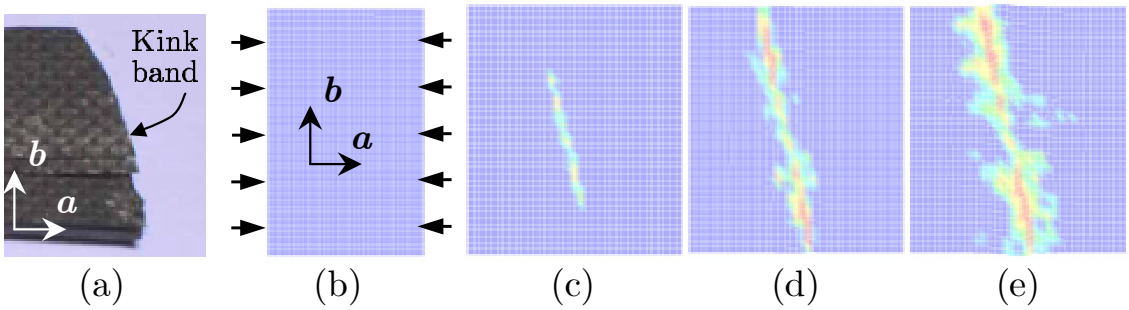

Figure 4.8: (a) Left half of a failed longitudinal compression test specimen; (b) model of the same specimen; (c) to (e) formation of a kink band and kink-band broadening

4.5.2 Crush of cantilever column specimens

In this sub-section, the numerical model is applied to simulate the crushing of composite columns. Cantilever columns were manufactured to a nominal thickness of 1mm , free length of 5mm and width 10mm , and were quasi-statically crushed by a metallic surface (coated with a PTFE spray) with an inclination of $2\,^{\circ}$, as shown in Fig. 4.9. Two different situations are studied. The first uses the T300/913 material system with a $(-45_2, 45_2)_S$ layup. The second uses previous experimental results from Davies [156], corresponding to a HSC/913 material system with a $(-45, 0, 90, 45)_S$ layup.

The complexity of this type of problem is considerably greater than in the previous examples, particularly after the peak load is attained. Furthermore, the problem is markedly chaotic, in the sense that small variations from one specimen to the other or in the loading and boundary conditions result in damage localizing in different parts of the specimen, and in different load vs. displacement curves, most notably after the peak load. However, there should be a common pattern to the form in which all specimens fail, as well as in the load vs. displacement curves.

4.5.2.1 T300/913 with $(-45_2, 45_2)_S$ layup

The failure mode of the T300/913 specimens with $(-45_2, 45_2)_S$ layup observed experimentally was similar for all specimens, even though damage could localize in different regions for different specimens. It consisted of a small crushed region formed

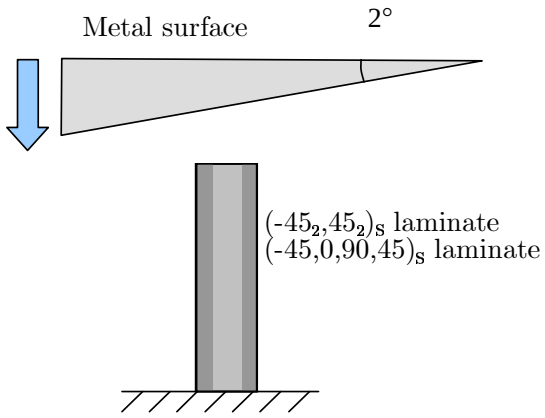

Figure 4.9: Representation of the column being crushed by a rigid surface

next to the loading surface; crushing at 45 ° to the loading axis on the surfaces of the specimens; and delaminations at the interfaces between the ±45 ° plies. These features can be observed in Fig. 4.10(a) and (b).

The numerical analysis of this problem also proves to be chaotic—small variations in certain input parameters to the numerical model result in a completely different output, at the end of the analysis. For this reason, instead of comparing an experimental load vs. displacement curve with a numerical one, a cloud of experimental points corresponding to the 23 columns tested is compared to a cloud of numerical points, corresponding to several numerical analyses, in which two different values were assigned to a number of parameters. More specifically, two different levels of mesh refinement were tried (1 and 2 elements per ply thickness), two different velocities of the impacting surface (500mm/s and 5000mm/s , the kinetic energy in the model was negligible compared to the internal energy for both situations), two different impact angles (2 and 2.5 °), two different metallic surface/ composite column friction coefficients (0 and 0.05), and two different approaches to deal with failed elements. Concerning this last point, failed elements (particularly those in contact with the impacting surface) have to be deleted at some point in the analysis, because they typically develop excessive deformations which lead the numerical analysis to break down. However, there is no clear solution as to when to remove these elements from the analysis. Here, two possibilities were tried: deleting them immediately after they have failed completely ($\varepsilon = \varepsilon^f$) and keeping the failed

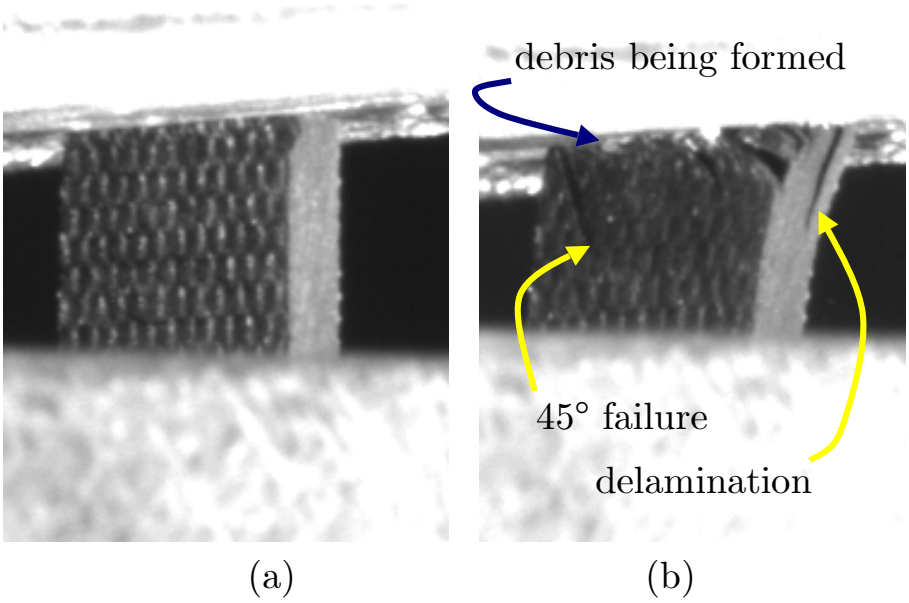

Figure 4.10: T300/913 composite column with $(-45_2, 45_2)_S$ layup (a) before crushing and (b) being crushed

elements in the analysis until $\varepsilon = 2\varepsilon^f$. Many other parameters could have also been subjected to variation, but the ones studied already result in a considerable number of combinations.

Two different pictures of deformed numerical models are shown in Fig. 4.11. It can be observed that the formation of debris is successfully simulated. The 45 ° failure patterns on the surfaces do appear in the numerical model, even though the clear formation of a distinct fracture line as observed in the experiments is not totally reproduced. However, probably the biggest achievement of the model is the prediction of delamination in the ±45 ° interfaces, which is a direct result of the ability of the matrix failure criterion to search for potential fracture planes.

The two clouds of points corresponding to the experimental and numerical load vs. displacement curves are presented in Fig. 4.12. It can be observed that the numerical results have higher initial stiffness than the experimental ones. This is believed to be essentially due to the compliance of the experimental fixture. The maximum load is particularly well predicted. The over-prediction of the load after the peak is essentially due to the growing complexity of the interaction between the

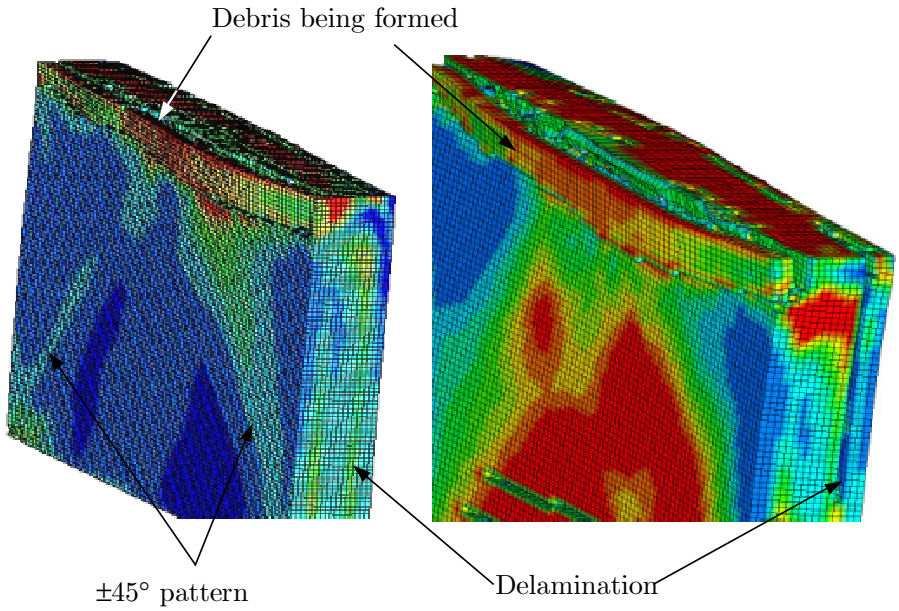

Figure 4.11: Numerical model of the T300/913 composite column with $(-45_2, 45_2)_S$ layup being crushed

rigid surface and the failing/failed elements, and suggests that further developments of the post-failure behaviour are needed.

4.5.2.2 HSC/913 with $(-45, 0, 90, 45)_S$ layup

For the HSC/913 specimens with $(-45, 0, 90, 45)_S$ layup, the failure mode was reported as consisting of two main delaminations in the $0/90^\circ$ interfaces, as well as matrix fracture in the outer -45° layers along the fibre direction [156]. The in-plane mechanical properties of HSC/913 are given in Table 4.1. For the in-plane shear response, the full stress vs. strain curve was not available, and so the curve for T300/913 was used, since the matrix system is the same. As before, in order to define the through-the-thickness properties, the material was assumed transversely isotropic. The fracture toughness values for the different failure modes for this material are not known, and thus the values for T300/913 presented earlier were used, and a sensitivity study running models with Γ_b, Γ_T, Γ_L, and Γ_{kink} at $\pm 10\%$ of their respective nominal values (Γ_a was not considered because fibre tensile failure did not occur; this leads to $1 + 2 \times 4 = 9$ numerical models in total) was performed.

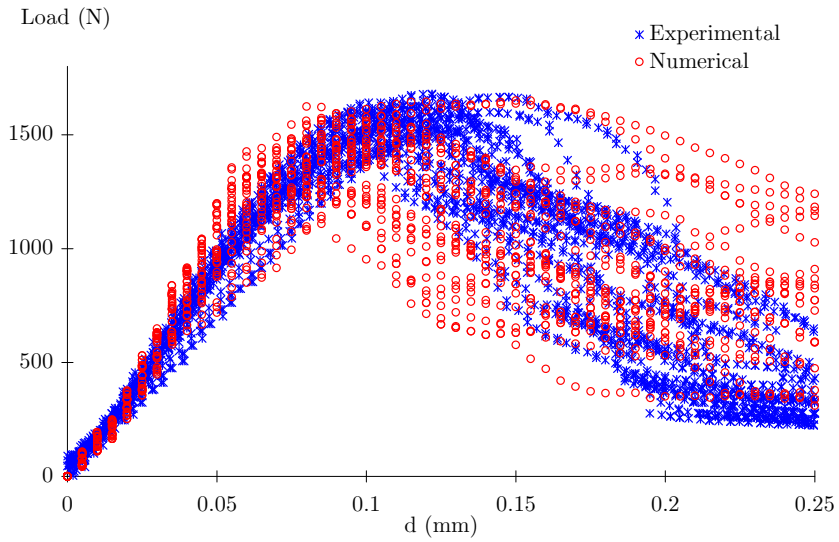

Figure 4.12: Experimental and numerical load vs. displacement curves corresponding to the T300/913 columns with $(-45_2, 45_2)_S$ layup being crushed

To capture the stress field accurately, two solid elements across the thickness of each composite ply were used in the numerical model, presented in Fig. 4.13 (the colour map shows matrix failure). The matrix fracture in the outer plies is correctly predicted. The delamination in the 0/90° interfaces is approximately simulated by the matrix failure in the 90° plies (the matrix fracture plane predicted by these failed elements is parallel to the 0/90° interfaces). Fig. 4.14 shows the experimental peak load and mean post-crushing load for different specimens tested (as well as average and standard deviation), and the numerical results corresponding to the 9 numerical models mentioned. While the mean post-crushing load is reasonably predicted, the predictions for the peak load are particularly good. It can be further noticed that small variations in the fracture toughness did not affect visibly the peak load, but did affect the mean post-crushing load. The numerical model also seems to slightly over-predict the mean post-crushing load, which might be due to the delaminations in the 0/90° interfaces not being properly modelled. Since these can be modelled using decohesion elements, this suggests that some improvement might be achieved.

A layer of decohesion elements is used in the 0/90° interfaces to investigate

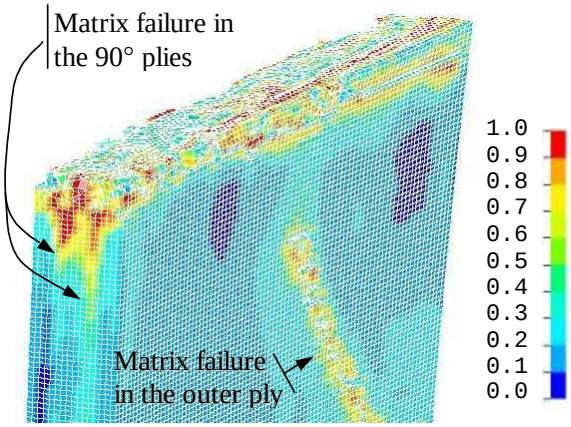

Figure 4.13: Numerical model of the HSC/913 column with $(-45, 0, 90, 45)_S$ layup being crushed

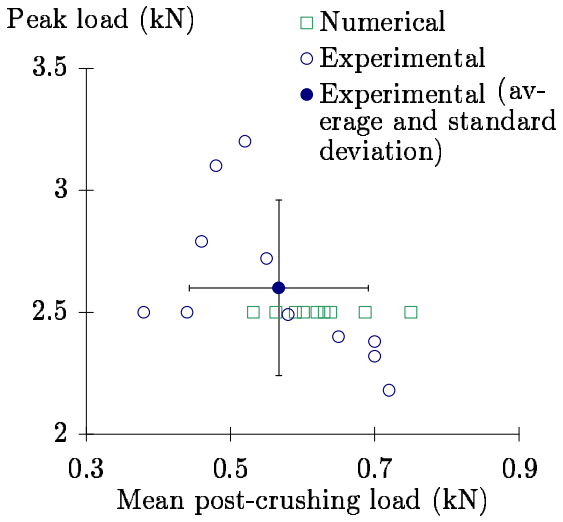

Figure 4.14: Experimental (from [156]) and numerical load vs. displacement curves corresponding to the HSC/913 columns with $(-45, 0, 90, 45)_S$ layup being crushed (without using decohesion elements)

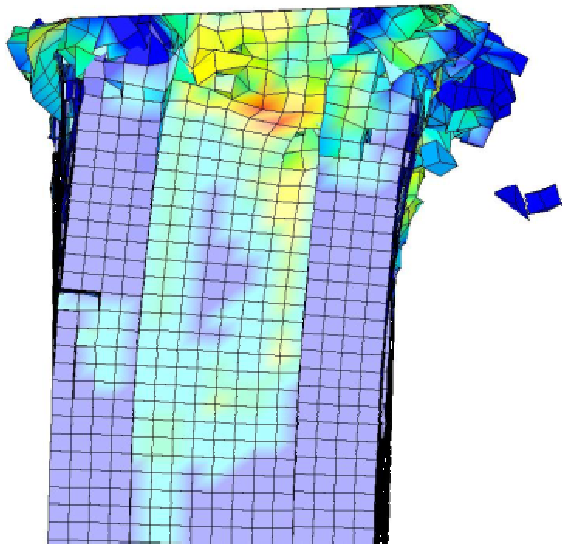

Figure 4.15: Numerical model of the HSC/913 column with $(-45, 0, 90, 45)_S$ layup being crushed, using decohesion elements

whether this brings an improvement on the predicted failure mode (Fig. 4.15) and post-crushing load (Fig. 4.16). It can be observed from Fig. 4.15 that the delamination is now predicted, which results in a reduction of the post-crushing load. Using decohesion elements, the post-crushing load is now slightly under-predicted, Fig. 4.16.

4.6 Conclusions

This work demonstrates that the current FE model can reproduce the key physical aspects observed in the failure of laminated composites, provided that sound, physically-based failure criteria are implemented, and that failure propagation is handled appropriately. The failure-models implementation is 3D, and allows the user to incorporate any in-plane shear curve directly. In addition, the pathological mesh dependency characteristic of CDM models is avoided using a smeared formulation. Finally, all parameters used in the model have clear physical meaning, and this chapter briefly identifies how they can be obtained from simple tests (a complete description of the fracture toughness tests for intralaminar matrix fracture is given in Chapter 5 and for the fibre-dominated failure modes in Chapter 6). The examples

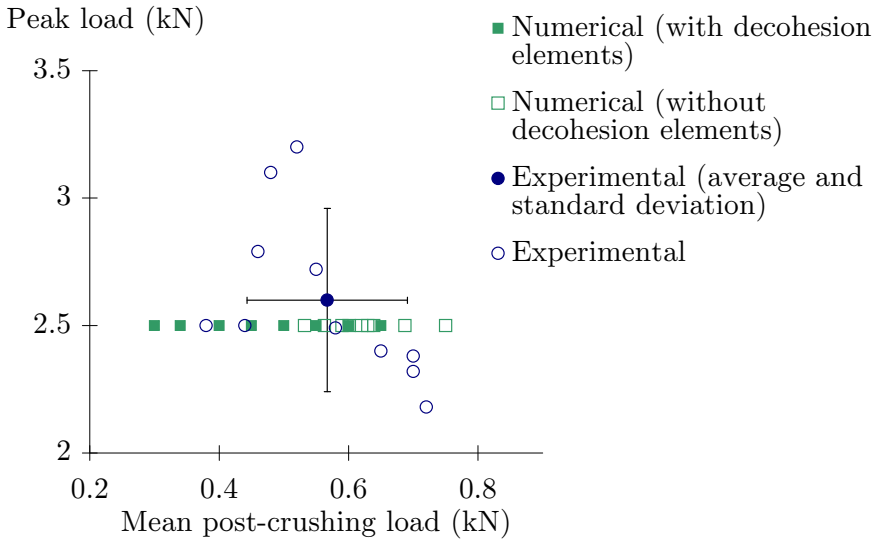

Figure 4.16: Experimental and numerical load vs. displacement curves corresponding to the HSC/913 columns with $(-45, 0, 90, 45)_S$ layup being crushed (including models with decohesion elements)

presented suggest that it might be beneficial to use this failure model together with decohesion elements in order to model delamination more accurately.

4.7 Publications

The work presented in this chapter resulted in the following publications[2]:

1. S. T. Pinho, L. Iannucci, P. Robinson. Crashworthiness of Composite Structures. Poster presented at GSEPS Research Student Research Symposium, Poster Competition, Imperial College London, 16^{th} July 2003 (won the 2^{nd} prize); *and* at Industrial Affiliates Annual Review Meeting, The Composites Centre, Imperial College London, 25^{th} September 2003

2. S. T. Pinho, L. Iannucci, P. Robinson. Physically-based Failure Models and Criteria for Laminated Fibre-Reinforced Composites: Development, Imple-

[2]Some of these publications include work from other chapters of this thesis and therefore feature again in the list of publications at the end of the corresponding chapters.

mentation and Validation. Aero Internal report 02/04, Imperial College London, 2004

3. S. T. Pinho, L. Iannucci, P. Robinson. Recent developments in modelling failure of laminated composite materials. The Composites Centre annual affiliates meeting, Imperial College London, 30^{th} September 2004 (power point presentation)

4. S. T. Pinho, L. Iannucci, P. Robinson. Physically-based Failure Models and Criteria for Laminated Fibre-Reinforced Composites: Development, Implementation and Validation. The Composites Centre annual affiliates meeting, Imperial College London, 30^{th} September 2004 (poster presentation)

5. S. T. Pinho, L. Iannucci, P. Robinson. Physically-based Failure Models and Criteria for Laminated Fibre-Reinforced Composites with emphasis on fibre kinking. Part II: FE implementation. In press, Composites Part A, 2005

6. S. T. Pinho, L. Iannucci, P. Robinson. Modelling failure using physically-based 3D models and a smeared formulation. 15^{th} International Conference on Composite Materials (ICCM-15). Durban, South Africa, 27^{th} June - 01^{st} July 2005

Chapter 5

Developing a four point bend specimen to measure the mode I intralaminar fracture toughness

5.1 Introduction

This chapter is concerned with the measurement of a particular intralaminar fracture toughness of unidirectional laminated composites. This toughness is the resistance to a crack growing in the thickness direction of the laminate, labelled 'transverse intralaminar crack growth' in Fig. 5.1. It is important for material characterization and for numerical modelling. Currently, there is no standard test to determine this property.

Different testing methods have been used to measure the intralaminar fracture toughness of laminated composites. The test methods most commonly used are the centre-notched tension [157], surface-notched tension [157], Compact Tension (CT) [157–161], Three Point Bending (TPB) [157, 158, 162, 163], Four Point Bending (FPB) [164, 165], double edge notch [163], double cantilever beam [166] and the wedge insert fracture [167]. Investigations into size effects for the CT specimen [157] and for the FPB [165] concluded in both cases that the effect of specimen dimensions did not affect the fracture toughness appreciably. Furthermore, Garg

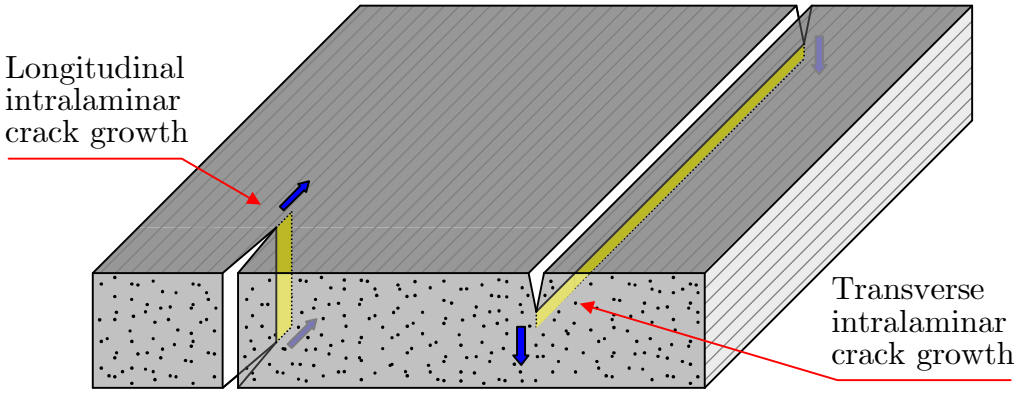

Figure 5.1: Transverse and longitudinal intralaminar crack growth

[157] compared the fracture toughness obtained using TPB and CT specimens, and observed good consistency.

An important characteristic exhibited by some unidirectional composites is an increasing R-curve in the intralaminar toughness which has been attributed to fibre bridging [163, 166]. In such cases, it is usual to take the initiation toughness value for use in design as this is conservative. The accurate measurement of the initiation toughness is therefore a key requirement of an intralaminar toughness test and it has been shown that a poor initial pre-crack can lead to an artificially high initiation toughness [159]. However, it is more difficult to introduce a sound and sharp intralaminar pre-crack than to introduce an interlaminar one, due to the layered structure of the material; the manufacture of specimens with pre-cracks formed during the layup and the cure process presents some technical difficulties, while the introduction of a pre-crack after manufacture of the laminate can cause damage around the intended crack tip.

In order to introduce an intralaminar pre-crack into a cured composite, breaching tools [160], wire-blade saws (0.1 mm thick) [163], jeweler saws (0.35 mm thick) [157] and razor blades ($0.06 - 0.1$ mm thick) [159, 161, 165, 168] have all been used. However, it has been found that introducing the crack mechanically after the composite has been cured provokes damage ahead of the crack tip, which can compromise the toughness values obtained [165, 168].

To produce a pre-crack during layup, previous work [164] has investigated ap-

plying a PTFE spray onto a cut made along the fibre direction in the pre-preg assembly (not to the full thickness of the pre-preg assembly), prior to cure. However, the PTFE spray failed to prevent the sides of the pre-crack from sticking together in the cured laminate, because of small movements of the plies during the cure process. A plastic release film placed into a cut in the prepreg assembly was later tried [165, 168, 169] instead of the PTFE spray, but the resulting pre-cracks were not straight and resin pockets often occurred at the crack tips. Finally, the use of a razor blade coated with a release agent, which was inserted into the pre-preg assembly and held in that position during cure, was investigated [165]. The pre-crack obtained was straight and sharp, but considerable distortions in the layered structure of the composite were present, as a result of the introduction of the blade and the mechanical constraint imposed by the blade during the cure.

In this work, the FPB test is used to measure the intralaminar fracture toughness, because of its simplicity and accuracy. The test method is briefly described and the investigations conducted into the manufacture of a sound, embedded pre-crack are presented. The tests carried out are then described and the results are presented and discussed.

5.2 Test method

The FPB test, adopted in previous work [164, 165, 168, 169] to determine the intralaminar fracture toughness of laminated composites, is used here. The test specimen, together with the loading conditions, is presented in Fig. 5.2. The test specimen is composed of a unidirectional laminate, with fibres aligned in the width direction of the specimen. The nominal dimensions of the specimen are 140mm in length, width $w = 10\text{mm}$, and thickness $h = 3\text{mm}$. The distances L and c in Fig. 5.2 are $L = 60\text{mm}$ and $c = 30\text{mm}$.

The critical stress intensity factor is defined as [170]

$$K_{Ic} = \frac{3Pc\sqrt{\pi a}}{wh^2} f\left(a/h\right) \tag{5.1}$$

where P is the total applied load at failure (the crack growth is unstable in this

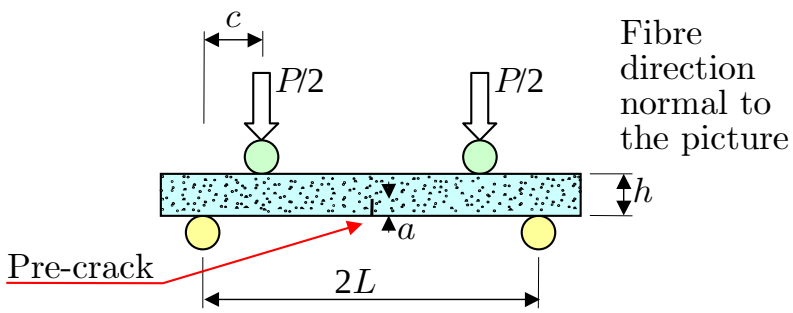

Figure 5.2: Four point bending test specimen and loading

test), a is the length of the initial pre-crack, and $f(a/h)$ is defined by

$$f(a/h) = 1.12 - 1.39\left(\frac{a}{h}\right) + 7.32\left(\frac{a}{h}\right)^2 - 13.1\left(\frac{a}{h}\right)^3 + 14.0\left(\frac{a}{h}\right)^4. \tag{5.2}$$

Assuming plane stress, the critical energy release rate is obtained from the critical stress intensity factor at the onset of crack propagation as

$$G_{Ic} = \frac{K_{Ic}^2}{E_b} \tag{5.3}$$

where E_b is the transverse modulus of the unidirectional laminate.

5.3 Manufacture

5.3.1 Material systems used

Two different carbon-epoxy unidirectional pre-preg systems were used. The system HSC/ SE84LV (produced by SP systems) was used for most of the tests and T300/ 913 (produced by Hexcel), was also used to confirm that the process to insert the crack into the laminate could be replicated with other materials. Both materials were cured according to the instructions from the respective suppliers. For the first material system, a consolidation cycle was also performed in some instances (as detailed later), and this also followed the instructions from the supplier.

The single material property needed for the data reduction is the in-plane transverse Young's modulus, which was determined using standard tests: $E_b = 8200$MPa for the SE84LV/ HSC, and $E_b = 8800$MPa for the T300/ 913.

5.3.2 Manufacture of the test specimens

Laminates with dimensions 200mm $\times$ 200mm were manufactured by laying up 24 layers of prepreg. The thickness of each panel was nominally 3mm. Depending on the method to introduce the pre-crack into the pre-preg assembly, some panels were manufactured by first stacking up together two or three sub-assemblies. All laminates were unidirectional, with the pre-crack running at the mid-length position, parallel to the fibres.

From the panels, specimens for FPB tests were cut using a wet saw. As noted earlier, the nominal dimensions of the specimens were 140mm in length, 10mm in width, and 3mm in thickness, with the fibres and the pre-crack oriented along the width. The actual width and thickness of each specimen, necessary for the data reduction, were obtained by averaging three individual measurements.

5.3.3 Introduction of the crack tips

Two different approaches to introduce the pre-crack into the laminates were investigated. In the first one, a plastic non-stick film was used to separate the two sides of the crack (Fig. 5.3(a)) and in the second one, a metal blade coated with release agent was used (Fig. 5.3(b)). The plastic film was a fluoroethylene polymer film, with a thickness of 0.0125mm, and the metal blade was composed of a row of steel razor blades, with nominal thickness 0.08mm. (The thickness of the blade at the sharp tip was considerably smaller than 0.08mm). For the metal-blade approach, two aluminium plates were used, which held the razor blades so that the depth of the protruding blade was 0.625mm in one case and 1.00mm in the other, see Fig. 5.3(b).

In previous work [164, 165], the film and metal-blade approaches have not consistently produced good quality cracks. In the current study, several variations of both approaches were investigated in a systematic way to identify the best method to produce pre-cracks of good quality. A description of all methods investigated to introduce the intralaminar pre-crack is now presented.

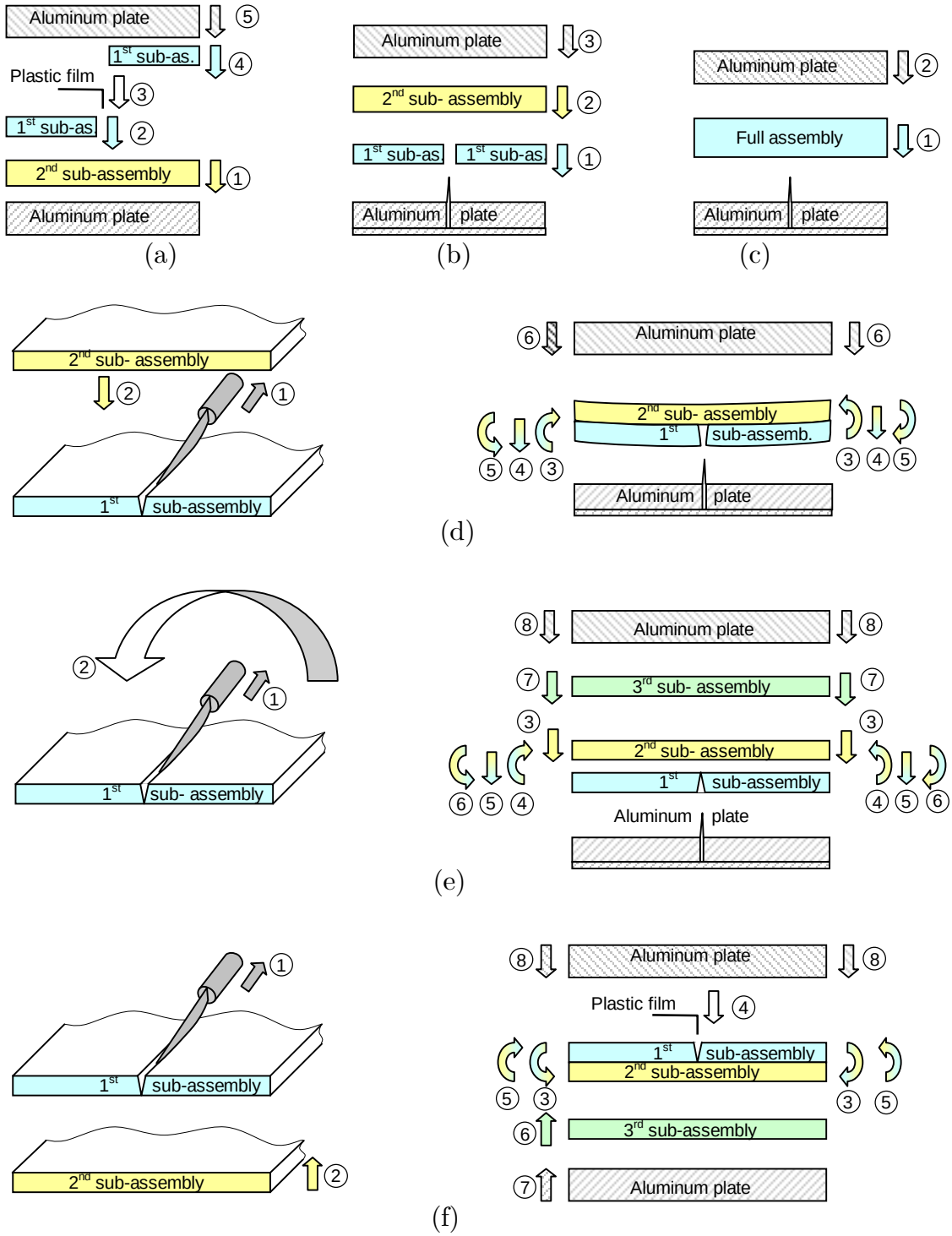

Notes: 1. the aluminium plates were all coated with release agent
2. the numbers ①, ②,... indicate the sequence of operations

Figure 5.3: Methods to introduce a pre-crack to a laminate: (a) method A, (b) method B, (c) method C, (d) method D, (e) method E and (f) method F

Method A This method uses the plastic-film approach. From the 24 layers that constitute the final laminate, part of them are stacked together in one sub-assembly, and the remaining are stacked together in another sub-assembly. (The number of plies in each sub-assembly depends on the required depth of the pre-crack.) The first sub-assembly is cut at the mid-width position, along the fibres, using a scalpel. One half of it is then positioned carefully on top of the second (uncut) sub-assembly, allowing the non-stick film to be positioned as shown in Fig. 5.3(a). The positioning of the film requires great care to avoid wrinkles of the film at the crack tip, and to obtain a crack of uniform depth. The second half of the first sub-assembly is then very carefully positioned next to the film. Care in positioning the second half of the first sub-assembly is essential to avoid gaps adjacent to the film.

Method B This method uses the metal-blade approach. From the 24 layers that constitute the final laminate, part are stacked together in one sub-assembly, and the remaining are stacked together in another sub-assembly. The first sub-assembly is cut in the middle, along the fibres, using a sharp scalpel. Both halves are then carefully positioned on each side of the metal blade on the aluminium plate, as shown in Fig. 5.3(b). Attention must be paid to avoid, as much as possible, any gap between the laminates and the blade. The second sub-assembly is then positioned on top, taking care not to move the two halves of the first sub-assembly.

Method C This method also uses the metal-blade approach. The 24 layers are stacked together to form a single pre-preg assembly. The pre-preg assembly is then positioned on top of the aluminium plate holding the metal blade as shown in Fig. 5.3(c). Very carefully, pressure is manually applied on the pre-preg assembly to force the blade to penetrate it, and the upper part of the rig is finally positioned on top.

Method D This method uses the metal-blade approach. From the 24 layers that constitute the laminate, two sub-assemblies are laid up. In order to create the pre-crack, the first sub-assembly is cut at the mid-width position, parallel to the fibres, using a scalpel as shown in Fig. 5.3(d), but the two halves are not separated. The second sub-assembly, with the remaining layers, is then placed on top of the first

sub-assembly. Since the two halves of the first pre-preg assembly were not separated after they were cut, this process leads to a very small and uniform gap between the two halves, dependent on the thickness of the scalpel only. Fixing the first sub-assembly to the working surface before performing the cut facilitates the operation, as it prevents the relative movement of the two halves of the first sub-assembly. A small pressure can be applied on top of the second sub-assembly to improve the adhesion to the first one, and this also results in a reduction in the width of the gap created by the blade. The pre-preg assembly is then lifted off the lay-up surface and is bent gently so that the gap created by the cut is widened and this is carefully positioned over the razor blade held in the aluminium plate, as shown in Fig. 5.3(d). The upper plate is then positioned on top.

Method E This method uses the metal-blade approach. The 24 layers that constitute the laminate are stacked together in three different sub-assemblies. The first sub-assembly, shown in Fig. 5.3(e) is fixed to the table using tape. On its bottom side, a backing sheet is used (with a few layers of tape to reinforce the backing sheet at the intended cut position) to prevent the two halves from separating after the cut shown in Fig. 5.3(e) is made with the scalpel. As before, the cut is made along the fibres, at the mid-width position. After the cut is made, a backing sheet is positioned on top of the (first) sub-assembly, so that it can be moved more easily without separating the two halves. Very carefully, the two halves of the sub-assembly are detached from the table and turned over. This operation requires particular attention, since the two halves are linked together by the backing sheets (and tape) only. The two halves are again fixed to the table and the backing sheet (with tape) that is now on the top side is removed, so that the second sub-assembly can be stacked on top of the first one. The process just described might seem complex, but it produces a geometry for the cut that more closely matches the shape of the blade in the plate (i.e. the cut is widest at the lower surface and narrower at the crack tip, as indicated in Fig. 5.3(e), and in contrast to Fig. 5.3(d)). The same result can in principle be achieved more easily, by using equipment that controls accurately the depth of the cut instead of performing it manually. Fig. 5.3(e) represents how the

two sub-assemblies are then bent to facilitate placing them over the mounted razor blades, after which they are fixed to the plate (at the edges, using tape), to avoid any motion between them and the blade. The third sub-assembly is carefully positioned on top, followed by the upper part of the aluminum rig. Using this method, the third sub-assembly does not need to be bent, which is intended to reduce any distortion in the pre-preg layers due to bending.

Method F This method uses the plastic-film approach, and follows the same steps from method E until the first and second sub-assemblies are stacked on top of each other (i.e. with the first sub-assembly having been cut along the mid-width, parallel to the fibres). The two sub-assemblies are then turned over again, so that the cut is on top. This process is represented in Fig. 5.3(f), but the 'turning over' operations are omitted in the figure for simplicity. The assembly is then slightly bent, to facilitate the introduction of the plastic film in the gap. The third sub-assembly is then added below the second, and the whole is positioned between two aluminum plates.

5.4 Discussion of the suitability of each method to produce satisfactory crack tips

5.4.1 Comparing the plastic-film and metal-blade approaches (methods A and B)

The first goal of this work is to compare the ability of the plastic-film and the metal-blade approaches to produce satisfactory crack tips. For this purpose, two composite plates were manufactured following methods A and B.

A micrograph representative of the pre-crack obtained by method A (film) is presented in Fig. 5.4(a). It can be observed that the crack obtained is not straight, and the orientation of the crack tip is not in the intended crack direction (i.e. vertical in this figure). The waviness is probably caused by small movements of the plies during the cure process. Resin pockets at the crack tip have been reported in a previous

study using the film approach [165], but none were observed in the specimens micrographed in the current investigation. For the laminate manufactured by method B (metal blade), the aluminium plate with a 1.00mm protruding blade was used. The sub-assembly to be cut along the fibres (first sub-assembly) had 8 layers, and the other (second sub-assembly) comprised the remaining 16 plies. When removing the laminate manufactured by method B from the blade fixture, the laminate broke but this did not prevent the micrographic examination of the crack obtained. From the micrograph shown in Fig. 5.4(b), it is clear that significant movement of the plies has occurred.

For the plastic-film approach, it is not obvious how to overcome the waviness of the crack, or how to modify the method to obtain a sound crack tip. On the other hand, it was thought that for the metal-blade approach, modifications in the manufacturing method could lead to improvements on the crack tip quality and so methods C-E were investigated. The distortion of the plies next to the crack was believed to result from two factors: the reduction in thickness due to consolidation during the curing and any gap between the sub-assemblies and the blade, due to the manual positioning, that may have enabled excessive movement of the plies to occur during cure. It was not clear however how much each factor contributed to the final distorted shape of the layers next to the blade.

5.4.2 Alternative metal-blade approaches

5.4.2.1 Mounting the blade by pressure (method C)

The effect of the reduction in thickness on the distortion of the layers mentioned in the previous sub-section for the metal-blade approach can be reduced by pre-consolidating the sub-assemblies that constitute the pre-preg—so that the blade might be inserted to a depth that is closer to the final one, and less movement occurs during the curing process. The possibility of a gap between the blade and the layers of composite can be avoided by forcing the blade into the pre-preg assembly. For this purpose, method C was used with pre-consolidated sub-assemblies and the aluminium rig with smaller outstanding blades (0.625mm).

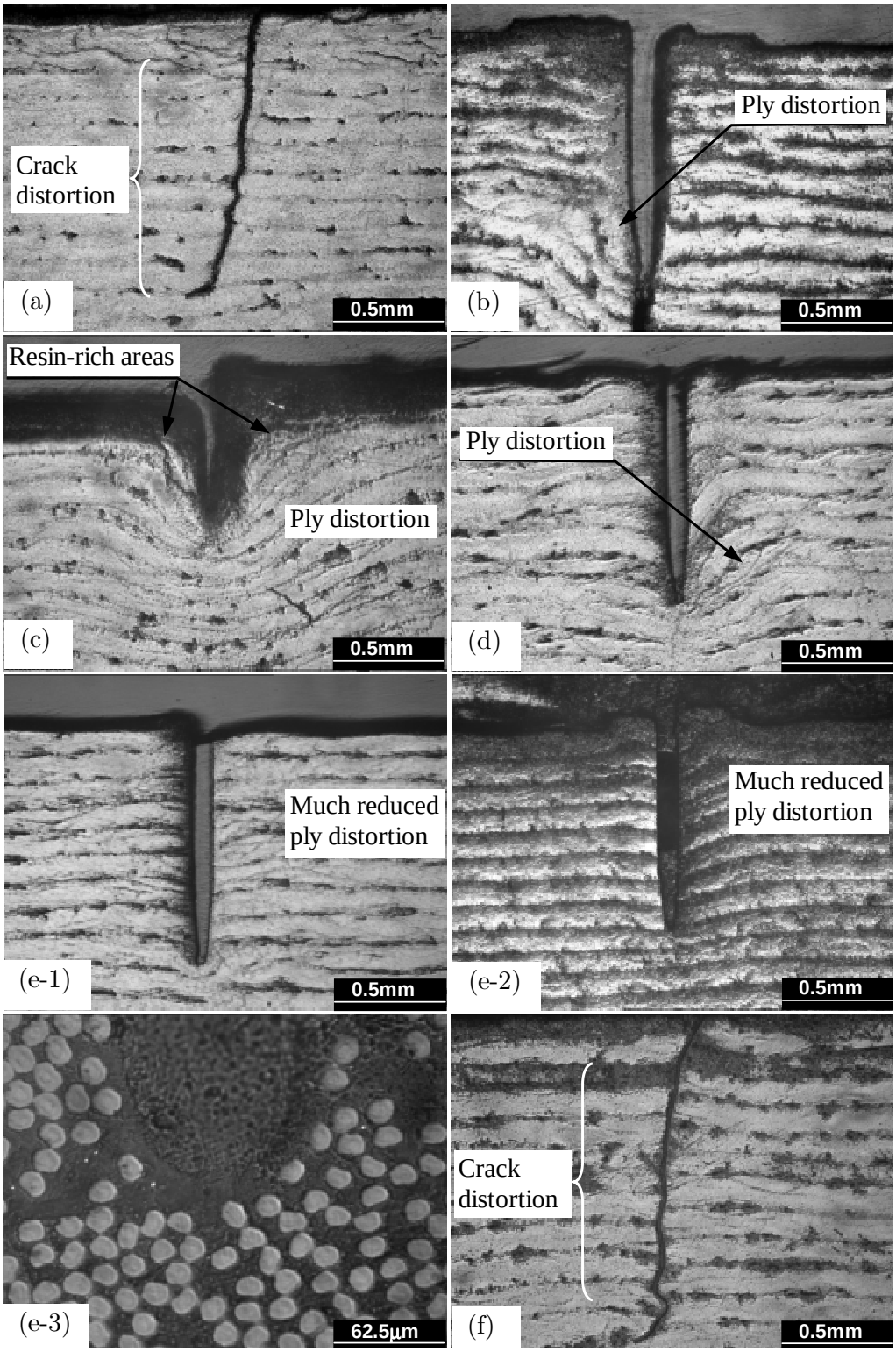

Figure 5.4: Pre-cracks obtained using method (a) A, (b) B, (c) C, (d) D, (e-1) E, (e-2) E, (e-3) E and (f) F

A micrograph representative of the crack tip obtained is shown in Fig. 5.4(c). It is clear that mounting the blade by pressure resulted in empty regions at the root of the blade that were filled by resin during the cure, resulting in considerable distortion of the layers.

5.4.2.2 Mounting the blade by bending the pre-preg assembly (method D)

The distortions obtained when mounting the blade by pressure suggested that it seemed possible to achieve better results if the blade was not forced through the pre-preg assembly. This led to the idea that bending the composite in order to insert the blade could be beneficial, resulting in method D to manufacture the crack. Since the effect of pre-consolidation could not be assessed in the previous trials due to the poor quality of the cracks obtained, two plates were manufactured by this method with pre-consolidation used for one.

The distortion of the plies next to the blade for cracks introduced by method D was found to be reduced but still significant, as shown in the micrograph in Fig. 5.4(d). Also, pre-consolidating the sub-assemblies did not appear to have a noticeable effect on the crack tip quality.

During the manufacture using method D, it became evident that, due to the profile of the scalpel used to cut the sub-assembly, a small gap would result between the pre-preg assembly and the razor blade, close to the crack tip. This feature is exaggerated in Fig. 5.3(d) for better understanding. However, it was not clear how much this aspect contributed to the observed distortion of the layers.

5.4.2.3 Mounting the blade by bending the pre-preg assembly in a modified way (method E)

It was thought that the small gap between the pre-preg assembly and the blade, at the crack tip, that resulted from using method D could be avoided if the cut sub-assembly was reversed before it was mounted on the razor blades. Also, the compression that resulted in the layers away from the crack during the bending process may have contributed to ply distortions. Furthermore, during the bending

process, the considerable stiffness of the uncut layers made the bending process more difficult. As a result of these considerations, a modified bending procedure was developed—method E. In this method, only two uncut layers (second sub-assembly) were holding the (first) cut sub-assembly together before it was mounted on the aluminium plate. The remaining layers (third sub-assembly) were stacked immediately afterwards.

This method resulted in the smallest ply distortions obtained so far, as Fig. 5.4(e-1) shows.

In order to investigate if the same crack tip quality could be achieved with other materials, the same manufacturing procedure (method E) was repeated with another material, T300/ 913. The pre-crack quality resulting for this material, shown in Fig. 5.4(e-2) confirms that method E is appropriate to systematically manufacture a panel with a sound pre-crack without introducing considerable distortions into the layers of the laminate. A bigger magnification of the crack tip in Fig. 5.4(e-2) is shown in Fig. 5.4(e-3). It can be observed that the crack tip is sharp, despite some wearing of the blade in the aluminium plate that occurred during the successive trials.

5.4.3 Improving the plastic-film approach (method F)

Method E, which uses the metal-blade approach, proved to reduce the distortion in the layers of the laminate to a minimum, by successfully reducing the empty space between the pre-preg assembly and the blade. The effect of this procedure on the plastic-film approach seemed worth investigating, even though this manufacturing method could not prevent the small ply movements distorting the plastic film during the cure. As a result, method F was developed, which essentially applies the bending method E to the plastic-film approach. A plate was manufactured, using material HSC/ SE84LV, and the corresponding micrograph of the crack is shown in Fig. 5.4(f). It was confirmed that the plastic film was unable to create a straight crack even with this improved manufacturing process.

5.5 Testing

5.5.1 Experimental procedure

FPB tests were carried in an Instron machine, with a 1kN load cell. The load was applied to the specimens using 6mm diameter rollers. The body containing the upper rollers was free to rotate (about a central horizontal axis parallel to the width direction of the specimen) in order to accommodate eventual minor misalignments and guarantee that both loads applied to the left and right side of the specimen were equal. Rubber fittings were used between the rollers and the specimens, to avoid stress concentrations due to any minor misalignment. The specimens were loaded up to failure at 0.5mm/min . The failure loads were recorded, and Eqs. 5.1 to 5.3 were used to obtain the fracture toughness. The actual pre-crack length was measured individually for each specimen after the tests using an optical microscope.

5.5.2 Results

The average fracture toughness and coefficients of variation obtained for each method, are presented in Table 5.1. The features on the fracture surface of failed specimens show features characteristic of mode I fracture, see Fig. 5.5.

5.5.3 Discussion

The test results show low scatter on the intralaminar fracture toughness measured for all methods used to create the pre-crack. The mode I interlaminar fracture toughness for HSC/ SE84LV and T300/ 913 have been measured using standard tests as $235\,\mathrm{J/m^2}$ and $258\,\mathrm{J/m^2}$ respectively, which is found to be similar to the intralaminar values obtained here. This similarity in the fracture toughness values was expected, since the fracture processes are also similar.

The intralaminar fracture toughness values obtained using the plastic-film approach were found to be similar in magnitude to those obtained using the metal blade, provided the ply distortions are reasonably small. This contrasts with previous results [165], where the intralaminar fracture toughness obtained using the

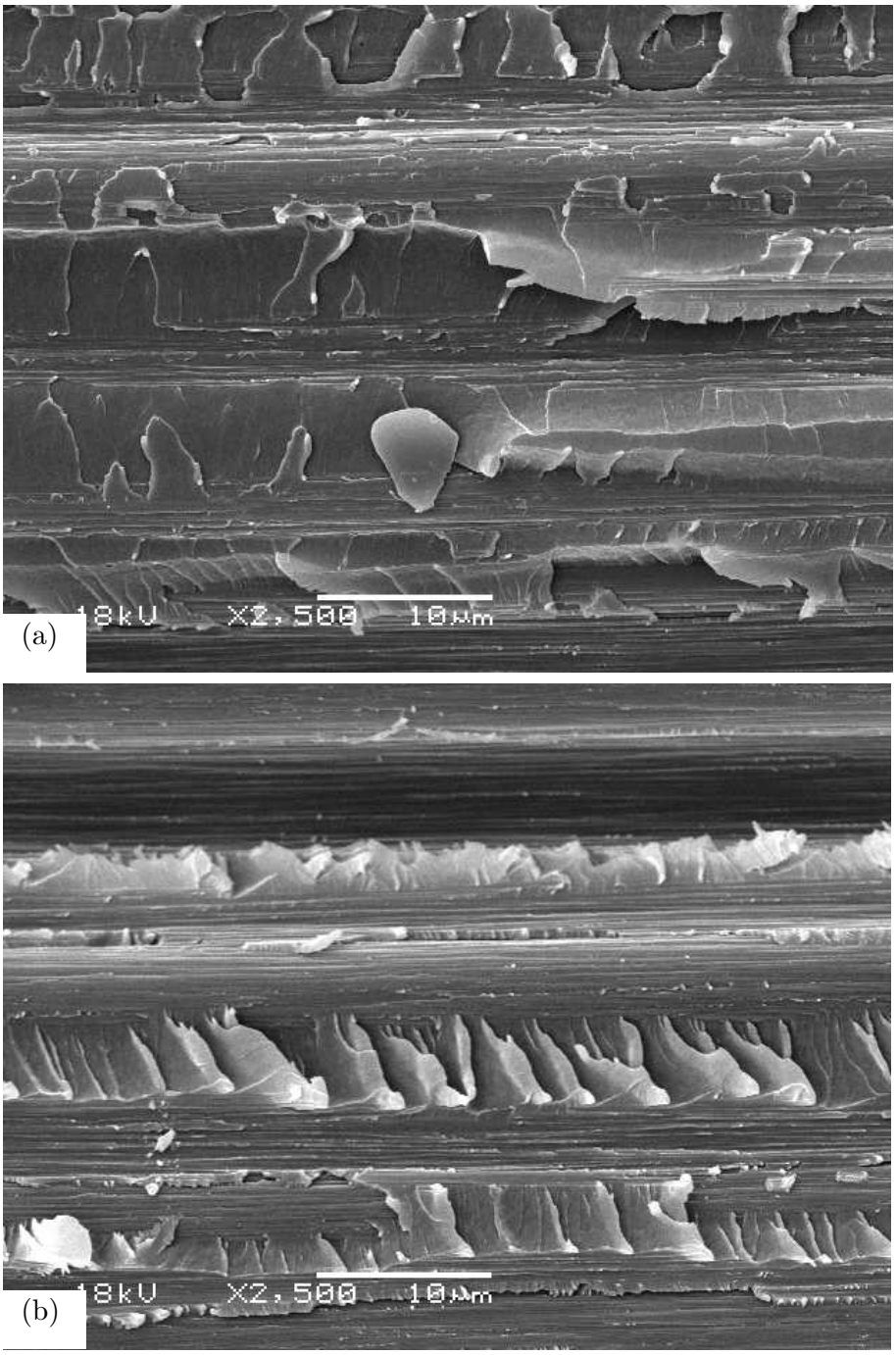

Figure 5.5: SEM images of the fracture surface of a FPB specimen, showing evidence of mode I fracture

Table 5.1: Fracture toughness values obtained from the tests

Material	Method	a nominal (mm)	N° of specimens tested	Average G_{Ic} (J/m^2)	Coefficient of variation (%)
	A	1.25	5	208	7.2
	C (pre-cons.)	0.625	7	257	5.3
	D (pre-cons.)	1	6	232	9.9
HSC/	D	0.625	5	218	5.6
SE84LV	E	0.625	7	228	8.5
	E	1	7	222	6.0
	F	1.25	6	213	7.5
	All	-	43	226	9.3
T300/ 913	E	1	13	211	6.4

plastic-film approach was found to be slightly higher than the one obtained with the metal-blade approach. In that previous study, the higher values were attributed to resin pockets at the crack tips, which were not observed here. Possibly, the resin pockets at the crack tip were avoided in this work because the plastic film was more precisely aligned with the end of the pre-cut.

For the specimens with a pre-crack obtained by the metal-blade approach, those with higher ply distortion appear to produce generally higher toughness values.

5.6 Conclusions

This work shows that it is possible to manufacture unidirectional laminated panels including straight and sharp pre-cracks, without damage ahead of the crack tip and without causing significant distortion to the layers. This can be achieved following the process referred to as method E in this chapter.

FPB tests were shown to yield values for the mode I intralaminar fracture toughness with low scatter, which are close to the mode I interlaminar fracture toughness.

The results obtained seem to indicate that there is a correlation between ply distortion and an increased measured fracture toughness. However, for the specimens

tested (all specimens had sharp crack tips and no damage ahead of the crack tip was present), this correlation is not strong.

Using a plastic film to create a pre-crack does not yield a straight pre-crack, but the fracture toughness values obtained were found to be consistent with those obtained using the metal-blade approach to create the pre-crack.

5.7 Publications

The work presented in this chapter resulted in the following publications[1]:

1. S. T. Pinho, P. Robinson, L. Iannucci, Intralaminar toughness tests of T300/913 carbon-epoxy, Tech. rep., Department of Aeronautics, Imperial College London (2005)

2. S. T. Pinho, L. Iannucci, P. Robinson. Modelling failure using physically-based 3D models and a smeared formulation. 15^{th} International Conference on Composite Materials (ICCM-15). Durban, South Africa, 27^{th} June - 01^{st} July 2005

[1]Some of these publications include work from other chapters of this thesis and therefore feature again in the list of publications at the end of the corresponding chapters.